Montanuniversität Leoben

Dissertation

Processing – Structure – Property Relationships

in Selected Iron-Based Nanostructures

Timo Müller

Leoben, April 2018

Erich Schmid Institute of Materials Science

Austrian Academy of Sciences

Jahnstrasse 12

8700 Leoben

Austria

Affidavit

I declare in lieu of oath, that I wrote this thesis

and performed the associated research myself,

using only literature cited in this volume.

Timo Müller

Leoben, April 2018

Acknowledgments

This work would not have been possible without the support by many people. To begin with, I would like to thank my supervisor Reinhard Pippan for his excellent guidance throughout my studies. He gave me the opportunity to work independently, but guided me with good advice and many great ideas based on his incredible experience and knowledge. Thank you also for the opportunity to attend so many inspiring conferences!

I am very grateful to Andrea Bachmaier, who not only paved my way to Leoben and gave me the possibility to install a new electrodeposition setup, but also spent a lot of time to revise my presentations and manuscripts and contributed several important ideas to my work. Furthermore, her and Georg's help with the tensile sample preparation relieved me from a lot of work.

I would like to thank all colleagues at the Erich Schmid Institute who helped me with my experiments: Jozef and Juraj for help with XRD; Thomas for spending many hours at the nanoindenter; Verena for measurements with the new indenter; Florian for an introduction to DSC; Karo, Julian, Zaoli, Gabi and Wicki for compensating my limited TEM competencies; Ruth and Marlene for performing the micromechanical experiments and, together with Markus, Daniel, Reini and Bernardo, for support at the FIB; Toni, Stefan and Gerald for problem solving at the SEM; Thomas for keeping the vacuum furnace in good condition; Oli for performing rolling experiments; and finally (although I'm sure, I have forgotten someone) Peter for his expertise at the HPT. Furthermore, I would like to thank Franz and Robin for manufacturing various custom-made parts and Silke for polishing many samples, sharing her knowledge about metallography and providing space for my electrochemical experiments in her lab.

Unfortunately (or luckily?), scientific work does not only consist of experiments. I am thankful to Dani, Sabine and Doris for managing all the administrative duties and to all colleagues for the enjoyable working environment and good cooperation. Particularly, I would like to thank Kathi, who helped me a lot getting started with my studies in Leoben, and Pradipta, who invited me to join his synchrotron beamtimes paving the way to my next scientific destination. A big thank you also to my office colleagues Lisa and Sascha for many discussions and a friendly, but productive working atmosphere!

Finally, I would like to thank all people who have enriched my life outside the institute during the last years – in particular, the members of the guitar orchestra Graz, who gave me a guitaristic home in Austria, and my family, who supported me throughout my studies in spite of the geographical distance.

Abstract

Motivated by their extraordinary properties, many interdependencies between processing routes, microstructures and properties of nanostructured materials have been investigated in the past. Both top-down and bottom-up manufacturing techniques have been used to prepare unique nanostructures. In the present work, one aspect, that has only attracted little attention in the research so far, is investigated for one method from each approach.

First, it is shown, that high-strength materials in multi-component systems can be obtained via HPT more efficiently, i.e. after reduced strains, when finer, more homogeneous starting materials are used. The two model systems – martensite and coated powder (compared to ferritic-pearlitic steel and powder mixtures) – demonstrate, that this holds on very different length scales. In the case of single-phase supersaturated solid solutions as starting materials, the process of mechanical mixing during HPT, which requires very high strains, is not necessary. Thus, high-strength materials can be prepared at moderate strains, as is demonstrated for a martensitic 0.1 wt.-% C steel reaching a tensile strength of 2.4 ± 0.1 GPa after a von Mises equivalent strain of only 7.5. For the coated powders, where the chemical distribution is homogenized only on a macroscopic length scale, intermixing still takes place during HPT, but is accelerated due to the shorter distances as compared to coarser and more inhomogeneous starting material. Therefore, high strength materials are obtained after moderate strains, too. On the other hand, oxides introduced by the coating process have significant influence on the results.

Secondly, the mechanical properties and deformation behavior of nanostructured electrodeposited iron-based alloys, which have been mainly studied for their functional properties so far, are investigated. Microstructural anisotropy and alloying with light non-metallic elements have a large impact also in this case and are discussed in detail. In nanostructured Fe-C alloys prepared via electrodeposition, the microstructure with a grain size of about 20 nm might be the basis for a high-strength material, but the embrittlement due to oxygen codeposition results in brittle failure already at small loads. Whereas brittle behavior is present in Fe-P electrodeposits as well, it is shown that amorphous/crystalline multilayer structures can be deposited in this system from a single electrolyte and the hardness of the films can be adjusted via the sublayer thickness of the crystalline layer following a Hall-Petch behavior down to a sublayer thickness of 15 nm.

Kurzzusammenfassung

Aufgrund ihrer außergewöhnlichen Eigenschaften wurden in der Vergangenheit schon zahlreiche Korrelationen zwischen Herstellung, Gefüge und Eigenschaften nanostrukturierter Werkstoffe untersucht. Sowohl Top-Down- als auch Bottom-Up-Methoden eignen sich dabei für die Herstellung einzigartiger Nanostrukturen. In der vorliegenden Arbeit wird für je ein Verfahren der beiden Herstellungsansätze ein Teilaspekt betrachtet, der bisher nur wenig Beachtung erfahren hat.

Zunächst wird gezeigt, dass die Verwendung feinerer, homogenerer Ausgangsmaterialien in Mehrkomponentensystemen die Top-Down-Herstellung hochfester Materialien mittels HPT effizienter macht, d.h. die benötigten plastischen Dehnungen reduziert werden. Die beiden Modellsysteme, Martensit und beschichtete Pulver (verglichen mit ferritisch-perlitischem Stahl und Pulvermischungen), zeigen, dass dies auf unterschiedlichen Größenskalen möglich ist. Im Fall einphasiger übersättigter Mischkristalle ist das mechanische Legieren, für das in der Regel sehr hohe Dehnungen notwendig sind, im HPT-Prozess nicht mehr erforderlich. Daher können hochfeste Materialien schon bei moderaten Dehnungen hergestellt werden, wie ein martensitischer Kohlenstoffstahl mit 0.1 gew.-% C zeigt, der nach einer von-Mises-Vergleichsdehnung von nur 7,5 eine Zugspannung von 2,4 ± 0,1 GPa aufweist. Im Fall der beschichteten Pulver, wo eine Homogenisierung nur auf einer makroskopischen Ebene vorliegt, findet mechanisches Legieren nach wie vor statt, ist aber aufgrund der geringeren Abstände zwischen den Phasenregionen beschleunigt. Daher werden auch hier hochfeste Werkstoffe durch moderate plastische Dehnungen erreicht. Andererseits haben in diesem Fall Oxide, die während des Beschichtungsprozesses gebildet werden, bedeutenden Einfluss auf die Ergebnisse.

Anschließend werden die mechanischen Eigenschaften und das Verformungsverhalten nanostrukturierter, elektrochemisch abgeschiedener, eisenbasierter Legierungen, die in früheren Arbeiten überwiegend bezüglich ihrer funktionalen Eigenschaften charakterisiert wurden, untersucht. Auch hier haben die Gefügeanisotopie und das Legieren mit leichten nichtmetallischen Elementen entscheidenden Einfluss auf die Ergebnisse und werden ausgiebig diskutiert. Im ersten betrachteten System, elektrochemisch hergestellten Fe-C Legierugnen, böte die Mikrostruktur mit einer Korngröße von etwa 20 nm eine geeignete Grundlage für ein hochfestes Material, jedoch führt die Sauerstoffversprödung schon bei geringen mechanischen Lasten zu sprödem Versagen. Obwohl sprödes Verhalten auch bei elektrochemisch abgeschiedenen Fe-P Schichten vorliegt, wird gezeigt, dass in diesem System amorph/kristallin-Multilayer aus einem einzigen Elektrolyten abgeschieden werden können, deren Härte bei Schichtdicken von über 15 nm einem Hall-Petch-Verhalten folgt und daher über die Schichtdicke eingestellt werden kann.

Contents

List of Abbreviations, Variables and Constants

a	thermodynamic activity
A	surface area
CE	current efficiency
d	(sub-)layer thickness
e	elementary charge ($1.602 \cdot 10^{-19}$ C)
E	potential
F	Faraday constant (96485.34 C mol^{-1})
h	sample height
HPT	high pressure torsion
m	mass
M	molar mass
N	number of revolutions
N_A	Avogadro constant ($6.02 \cdot 10^{23}$ mol^{-1})
r	radius
R	gas constant (8.314 J K^{-1} mol^{-1})
SEM	scanning electron microscopy
SPD	severe plastic deformation
t	time
T	temperature
TEM	transmission electron microscopy
XRD	X-ray diffraction
z	number of elementary charges
γ	shear strain
ε_{vM}	von Mises equivalent strain
η	overpotential
ρ	density

I. Introduction

Nanostructured materials – and in particular nanocomposites – have been used already in ancient times mainly due to their functional properties (e.g. in color pigments [1, 2]), but also due to their exceptional mechanical strength (e.g. in the Damascus sword [3, 4]). Whereas the reason for the unique properties were unknown in those days, a vast number of investigations during the last decades has assembled the huge knowledge about structures, properties and structure-property relationships of these materials, that we have today.

The different properties of nanostructured materials as compared to their coarse-grained counterparts are mainly based on the increase in specific interface area with decreasing structural size [5]. Due to the different bonding conditions of atoms near the interfaces, many properties are affected, as was described already in the early work by Gleiter in 1981 [6]. Often, size effects, that are known from coarser structures, remain valid when decreasing the specific size down to the nanometer scale. However, when the specific interface area – or, due to the non-infinitesimally small width of actual interfaces, the specific interface volume – reaches a certain threshold value, new atomistic processes become relevant. For example, the Hall-Petch relation, that was originally empirically found for steels with a grain size in the micrometer range [7, 8], provides a good description for the size dependency of the yield stress in nanostructured metals down to a grain size of about 10-50 nm [9, 10]. On the contrary, further decrease of grain size results in a yield stress plateau or even a decrease in yield stress when the grain size approaches the size of a dislocation loop and new deformation mechanisms such as grain boundary sliding or grain rotation become dominant [10-12].

Whereas inconsistent definitions of 'nanostructured materials' can be found in the past [13], a common definition is today widely accepted and also specified in an ISO standard, saying that nanostructured materials have an "internal structure or surface structure in the nanoscale", i.e. in the range between 1 nm and 100 nm [14].

In spite of the enormous progress in this field during the last decades, many questions are still unsolved. Furthermore, the technological development of new preparation methods and experimental techniques continuously extends the range of available nanostructures and observable structural details. In this thesis, a few selected aspects are investigated experimentally, focusing on nanostructured iron-based alloys. Relationships between preparation conditions, structures and mechanical properties are discussed emphasizing the impact of non-equilibrium phases, microstructural anisotropy and light non-metallic alloying elements.

I.1. Preparation of Nanostructured Metallic Materials

I.1.1. Overview

Nanostructured materials can be produced via a large number of different preparation techniques. Some of them, such as electrodeposition, are also widely used in the production of coarse-grained materials and the modification of certain processing parameters reduces the structural size to the nanometer range [15]. Other methods have been specifically developed for the preparation of nanostructured materials, often using and exhausting commonly known ways of structural refinement (as in accumulative roll bonding [16]). Whereas the ongoing development of new methods and the arbitrary distinction of sub-methods makes a comprehensive overview difficult, two general approaches can be distinguished. In the bottom-up approach, the nanostructured material is built up from tiny building blocks, usually atoms or molecules [17]. This approach includes all deposition methods, growing films on substrates via the deposition of atoms, ions or molecules from a liquid or gaseous phase [17]. On the contrary, the top-down approach starts with a bulk piece of (usually coarse-grained) material, the internal structure of which is refined during the process resulting in a characteristic structural size in the nanometer range [17]. The top-down approach includes all severe plastic deformation (SPD) techniques, which push the limits of the long-known structural refinement via plastic deformation towards smaller length scales utilizing deformation geometries, in which extremely large plastic strains can be realized [18]. Table 1 gives an overview of the most important bottom-up and top-down preparation techniques.

Although all these methods produce nanostructured materials, the products differ widely in structure and properties, depending on the preparation technique and the specific preparation

Table 1: Preparation methods of nanostructured materials [17, 19, 20]

Bottom-up approach	Top-down approach
- electrodeposition - physical vapor deposition - thermal evaporation - magnetron sputtering - chemical vapor deposition - atomic layer deposition - inert gas condensation - microwave plasma synthesis	- ball milling - severe plastic deformation (SPD) - high pressure torsion (HPT) - equal-channel angular pressing - accumulative roll bonding - multiple forging - surface mechanical attrition

conditions. Structural differences include the chemistry (homogeneity, purity), the microstructure (grain size and shape, interface structure) as well as the crystallography (phases, texture) of the material. This opens up the possibility to produce tailored nanostructured materials by an appropriate choice of the preparation technique and conditions.

In the present work, electrodeposition and high pressure torsion (HPT), i.e. one technique from each approach, are used and will, thus, be introduced in the following.

I.1.2. High Pressure Torsion

In HPT, large shear strains are utilized to create ultrafine-grained or nanocrystalline structures via dislocation multiplication, their re-arrangement in small-angle grain boundaries via dynamic recovery and the transfer to high-angle grain boundaries upon the integration of further dislocations [18, 21]. The simultaneous application of hydrostatic pressure facilitates the application of large shear strains due to suppressed crack formation [22, 23]. Whereas the first HPT experiments were performed in the 1930s by Bridgman in order to investigate the effects of this type of deformation on several materials in general [24], HPT as a tool to prepare nanostructured materials was introduced in the 1980s by Valiev et al. [25, 26].

The ideal HPT process consists of a disc-shaped sample compressed and sheared between two anvils with planar surfaces [23]. The shear strain, γ, obtained via rotation of one anvil by N turns with respect to the other anvil equals [23]

$$\gamma = \frac{2\pi N r}{h} \quad .$$
(1)

This means, that the strain in a sample of thickness h increases linearly with increasing distance, r, from the disc center. The corresponding von Mises equivalent strain, ε_{vM}, is

$$\varepsilon_{vM} = \frac{\gamma}{\sqrt{3}} = \frac{2\pi N r}{\sqrt{3} h} \quad .$$
(2)

The practical application of such an ideal HPT tool is quite limited due to the continuous sample thickness decrease and inhomogeneous strain distribution in the unconstrained case and due to the effects of friction in the constrained case [27]. Thus, cavities in both anvils were already proposed in 1960 [28] and introduced to the modern HPT community in 2003 [29]. They are now common standard in the so-called quasi-strained HPT, that is used in modern HPT facilities [27, 30]. Equations (1) and (2) are also valid in this case in a good approximation.

Besides the dislocation-based understanding of grain refinement, that is known from ball milling and from other SPD techniques [31], refinement of the microstructure during HPT can also be considered from a geometrical point of view. Assuming approximately isotropic grains (or phase

regions) in the initial microstructure, the shear strain via HPT results in elongation along the shear direction and reduction of the smallest grain dimension (Figure 1a) [32]. Although this model can be transferred to reality only in a very limited range due to dynamic recovery and strain inhomogeneities (e.g. over the sample thickness [27] or locally due to plastic anisotropy of neighboring grains), structures aligned with respect to the shear direction are commonly observed after HPT processing and will be further discussed in chapter I.3. The commonly used terminology to discribe the different directions in HPT-treated samples is illustrated in Figure 1b.

As proposed by both the dislocation-based and the geometrical approach, the grain size of materials usually decreases during HPT treatments as a function of shear strain [21, 32]. However, this refinement is decelerated and finally stopped after a certain amount of deformation due to dynamic recovery, resulting in a dynamic equilibrium between dislocation multiplication and recovery processes, i.e. a macroscopically stable microstructure upon further deformation [21, 32]. The grain size in this state of saturation is in the ultrafine-grained size regime for pure metals and is reduced to the nanostructured length scale for alloys and composites [21]. For a given material, it can be modified via various deformation parameters [21]. The strongest influence is usually observed for the deformation temperature, since enhanced recovery processes at elevated temperature result in a larger saturation grain size [21]. Because this saturation state does not depend on the initial microstructure [33], also grain growth during HPT treatments can be observed when a nanostructured material with a grain size below the saturation grain size is used as starting material [34].

Whereas equations (1) and (2) describe the shear strain obtained in perfectly homogeneous deformation, inhomogeneity is regularly inherent to HPT experiments. On the one hand, macroscopic regions can be deformed more or less than predicted by equation (1) for example due to axial inhomogeneity or due to dead zones near the edge of the HPT samples [27]. On the other hand, shear band formation can result in strain localization in small volumes, significantly reducing the plastic deformation in the remaining part of the sample [36].
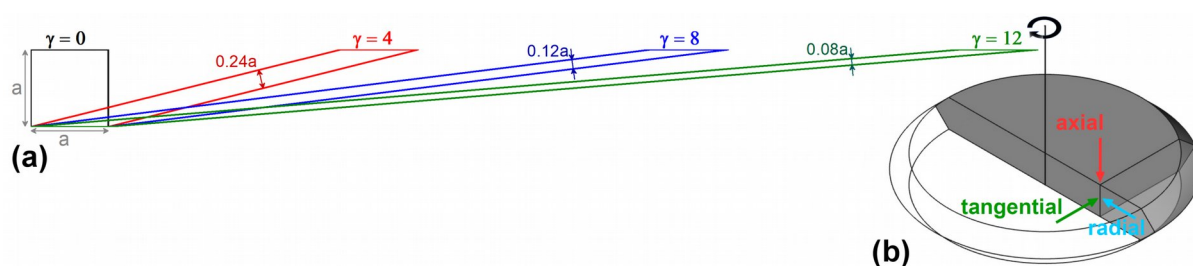

Figure 1: (a) The geometric consideration of refinement and grain shape change during HPT. For a sample height of 0.8 mm (as used in this work), the shear strains of 4, 8, and 12 are approximately obtained after half a turn at radius 1, 2 and 3 mm, respectively. (b) Terminology of directions used to describe HPT-deformed structures.

Although HPT is used for the preparation of nanostructured materials since several decades, the process is still subject of ongoing improvement and development. Furthermore, a number of modifications of the HPT technique have been proposed during the last years such as cyclic HPT [37], continuous HPT [38], high pressure double torsion [39], incremental HPT [40] or planar HPT [41].

I.1.3. Electrodeposition

In electrodeposition, a film is grown on a substrate via the electrochemical reaction of ions from an adjacent electrolyte [15]. Most commonly, metal films are deposited via the electrochemical reduction of the corresponding metal cations from the electrolyte. Its industrial application in electroplating technology is widely spread and used to improve for example the corrosion or wear resistance, the electrical conductivity or the solderability of surfaces [15]. Depending on the deposition conditions, the grain size of the films can be varied in a wide range from epitaxial single crystals [42] to nanostructured deposits [43, 44]. The availability of grain sizes in the nanometer range for certain electrodeposits had been known many years before the term 'nanostructured materials' was introduced in the 1980s [5]. For example, Dehlinger and Giesen reported a grain size of 15 to 20 nm calculated from X-ray diffraction (XRD) line broadening of electrodeposited brass already in 1932 [45].

The experimental setup for electrodeposition consists of an electrochemical cell including at least one electrolyte and two electrodes, i.e. electric conductors immersed in the electrolyte. When an electrode is immersed in an electrolyte, generally the electrochemical potentials are not identical in both phases resulting in a driving force for a transition of atoms from one phase to another [46]. In the case of a metal immersed in an electrolyte containing cations of the same metal, the difference in their electrochemical potentials results in either the oxidation of atoms from the solid and their dissolution in the electrolyte or in the reduction of ions and their incorporation into the solid phase [46]. However, this reaction causes the formation of an electrical voltage between the two phases that inhibits the continuation of the reaction [46]. For this reason, a state of dynamic equilibrium is reached after some time. The voltage, that exists between solid and electrolyte in this dynamic equilibrium, is called the equilibrium potential of the electrode, E^{eq} [15, 46]. In this context, the term 'electrode' is used for a complete half-cell, consisting of the electric conductor and the surrounding electrolyte [15]. Since measuring the potential requires inserting a second conductor into the electrolyte, which results in the same processes at the new interface, only differences between electrochemical potentials can be measured and the potential of the standard hydrogen electrode (platinized platinum immersed in an acidic solution with hydrogen ion activity of 1 mol l^{-1} bubbled with hydrogen gas of 1031 hPa pressure) has been

defined as the zero point of the potential scale [47]. Potentials under standard conditions (ion activity 1 mol dm^{-3}) are tabulated and called standard potentials, E_0^{eq} [15]. The dependence of the equilibrium electrode potential, E^{eq}, on the ion activity in the electrolyte, a_{Me+}, is described by the Nernst equation, that can be derived from the definition of the electrochemical potential [47] and equals

$$E^{eq} = E_0^{eq} + \frac{R \cdot T}{z \cdot F} \ln\left(a_{Me^{z+}}\right) \tag{3}$$

where R is the gas constant, F is the Faraday constant and T is the absolute temperature.

During metal electrodeposition, the electrode of interest, the working electrode, is the place of the metal reduction, i.e. the cathode. In galvanostatic deposition, the formation of a metal film is obtained by applying a controlled current or current density (current per substrate area) between this electrode and the anode (counter electrode). Since the electrode potentials of both electrodes change as a function of the applied current, a third electrode, the reference electrode, is needed in order to measure the change of the working electrode potential, E, as a function of the applied current (Figure 2a) [47]. This knowledge is important since the overpotential, η, which equals

$$\eta = \left| E - E^{eq} \right| \quad , \tag{4}$$

has large impact on the structure and properties of the deposit [15]. In potentiostatic deposition, the potential, i.e. the voltage between working and reference electrode, is directly controlled resulting in a corresponding current between working and counter electrode [15].

The measureable overpotential can be considered as the sum of overpotentials originating from the different steps of the transfer from a metal ion in the electrolyte to an atom incorporated in the solid deposit, as schematically depicted in Figure 2b [15]. First, the ions have to be transported to the vicinity of the electrode surface. Since convection is inhibited near the electrode surface and migration is often negligible in the whole system, the consumption of ions in the reduction process at the interface can only be compensated by mass transport via diffusion [15]. This results in an ion concentration gradient next to the interface, that can be approximated by the Nernst diffusion layer [48]. Next, the ions have to penetrate the electric double layer, that is formed close to the interface due to adsorption and Coulomb interaction at the charged electrode surface [49], get rid of their hydration or other ligand shell and get discharged at the interface [15]. After this charge transfer, the adsorbed atoms finally have to be incorporated into the solid structure. For crystalline deposits, this process is known as electrocrystallization [50, 51] and adds another component to the overall overpotential [15].
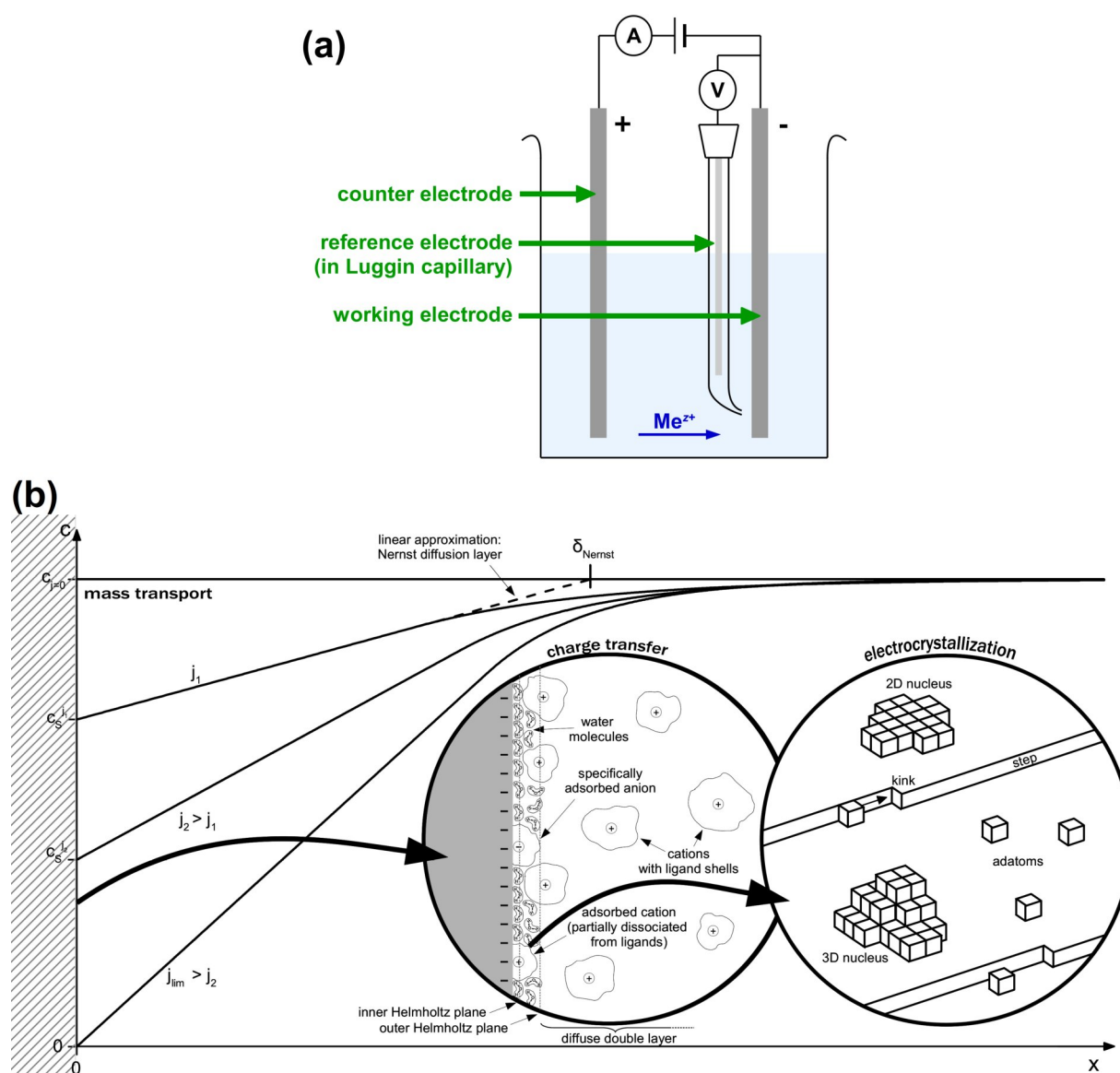
Figure 2: (a) Three-electrode setup for electrodeposition.
(b) Schematic drawing of the processes during metal electrodeposition [15, 46]

Usually, relatively high overpotentials (often several hundred millivolts up to more than one volt) are needed to obtain fine-grained or even nanocrystalline deposits [15]. In the potential range, that is normally used in electrodeposition, the grain size decreases with increasing overpotential due to an increase in nucleation rate [52, 53]. Since iron, which is the metal of interest in this thesis, belongs to the group of metals with the highest overpotentials [15], fine-grained deposits are regularly obtained in this case [54]. Additionally, enhanced nucleation rates can be achieved using pulsed current [55] or certain bath additives ('grain refiners') [15, 53].

Due to its low standard potential, the electrodeposition of iron is always accompanied by the formation of hydrogen, which can either be incorporated in the deposit or leave the system in the

form of hydrogen gas [47, 56]. This side reaction lowers the current efficiency of the deposition process, since a fraction of the current is not used for metal reduction, but for the formation of hydrogen. If only the intended reduction of metal ions, Me^{z+}, to metal atoms, Me, takes place, the mass, m_{nom}, and the nominal thickness, d_{nom}, of the deposits after homogeneous deposition for time t at current density j are given by Faraday's law [15]

$$m_{nom} = \frac{M \cdot j \cdot A \cdot t}{z \cdot e \cdot N_A} \tag{5a}$$

$$d_{nom} = \frac{M \cdot j \cdot t}{z \cdot e \cdot N_A \cdot \rho} \tag{5b}$$

where M is the molar mass, A is the substrate area, e the elementary charge, N_A the Avogadro constant and ρ the density of the deposited film. If side reactions, such the formation of hydrogen, take place, the actually observed mass or thickness is reduced. Thus, the current efficiency, CE, which equals [15]

$$CE_m = \frac{m_{real}}{m_{nom}} \tag{6a}$$

or

$$CE_d = \frac{d_{real}}{d_{nom}} \quad , \tag{6b}$$

is smaller than 100 % in this case.

Due to is versatility, low costs and the transferability of both existing knowledge and experimental setups from conventional electroplating, electrodeposition is widely used for the preparation of nanostructured materials [57, 58]. In contrast to other deposition methods such as magnetron sputtering, the availability of high growth rates facilitates the preparation of nanostructured materials with a film thickness of up to several millimeters [59, 60]. This provides the possibility to investigate bulk materials in similar dimensions and with a comparable grain size, but with significant structural differences (e.g. concerning dislocation density) compared to the products of SPD.

I.2. Formation of Supersaturated Solid Solutions

Metastable non-equilibrium phase compositions are observed in many materials and differ widely in their thermodynamic (meta-)stability [61]. One popular example of a quite stable non-equilibrium phase is the cementite in Fe-C alloys, which is even that stable that the metastable phase diagram containing this phase is commonly used [61, 62]. Although observed in coarser structures as well, non-equilibrium phases occur much more frequently in nanostructured materials. This is due to the large energy input during their production in order to provide the excess energy for the large specific interface area as well as due to the influence of the large specific interface area on the phase stability [63]. While also completely new phases as compared to the phase diagram are found regularly (cf. chapter III.4), the most common deviation from the equilibrium phase composition in nanostructured materials is supersaturation, i.e. the extension of equilibrium phases beyond their compositional range according to the phase diagram. Solid solution strengthening results in an additional hardening effect besides the small grain size in these materials. Furthermore, supersaturated solid solutions are used to create nanostructured composites with unique properties via decomposition during tailored heat treatments [64].

Many properties of supersaturated solid solution, such as the enhanced strength, are independent of the preparation method. However, their formation is based on completely different mechanisms in bottom-up and top-down preparation techniques. In the bottom-up approach, the nanostructured material is formed completely from different phases. Thus, the formation of supersaturated solid solutions is obtained via the suppression of sufficient atom mobility to approach the thermodynamic equilibrium directly during the phase formation. The growing volume of the new phase usually has already its final composition. On the contrary, the formation of supersaturated solid solutions in top-down techniques usually starts with a mixture of several phases containing a phase with the crystallographic structure of the later supersaturated solution. Upon processing, the composition of this phase (or several phases) is then gradually shifted out of its equilibrium composition range via the dissolution of atoms from other phases until a state of saturation is reached [65]. Therefore, the supersaturation is obtained gradually in composition, but simultaneously in the whole volume (even if not necessarily homogeneously) [65].

During solidification from the melt, supersaturated solid solution are formed when the cooling rate is sufficiently high to suppress phase separation via diffusion. This principle generally holds for all bottom-up techniques. In electrodeposited alloys, supersaturation is a common phenomenon in many systems such as iron-, copper- or silver-based alloys [15, 66]. Solubility often increases with decreasing grain size or increasing overpotential, respectively [66]. Many alloys are deposited at enhanced overpotentials due to the addition of complexing agents or

surface-active additives to the bath, increasing the probability that non-equilibrium structures such as supersaturated solid solutions are formed. Besides the overpotential, the specific adsorption of chemical species during the deposition process has significant impact on the formation of solid solutions and the deposition of alloys in general [67]. On the one hand, they affect the mobility of discharged metal atoms at the interface and, thus, the diffusion that is necessary for phase separation. On the other hand, they can be incorporated into the deposit, changing its composition and thermodynamics [67].

In top-down preparation methods, the formation of supersaturated solid solutions requires the transfer of atoms from one phase to another, that increases – or at least would increase in a coarse-grained structure – the internal energy of the system. Several atomistic mechanisms for this process have been proposed, debated and also proven in experiments. First, the excess interface energy of nanostructured materials was suggested as a possible driving force for intermixing, but turned out to be insufficient to explain this phenomenon [68-70]. The contribution of the high dislocation densities in severely deformed materials, providing both a driving force and a fast diffusion path for intermixing [69], and an analogous process for excess vacancies [71-73] have also been discussed. Another model, proposed by Yavari, localizes the intermixing in small fragments with curvature radii approaching one nanometer and less, which dissolve due to their extremely high local excess interface energy [68, 74-76]. Additionally, mechanisms of mechanically driven intermixing have been proposed, in which atoms are transported from one phase to another by carriers of plastic deformation (dislocations or shear bands) crossing the interface. Examples are the kinetic interface roughening model [77] and the dislocation shuffling mechanism [78].

In general, the composition range, in which supersaturated solid solutions can be obtained, depends on the preparation method and its processing parameters as well as on the system under investigation (particularly lattice structures and enthalpy of mixing [79]). For both electrodeposition and high pressure torsion, single-phase solid solutions over a large or even the whole composition range have been reported for certain systems that are thermodynamically immiscible [79-82].

I.3. The Effect of Microstructural Anisotropy

Anisotropic properties exist in most materials and can originate from texture, residual stresses, composition gradients or the preferred orientation of grain and phase boundaries (microstructural anisotropy). In many cases, several of these effects occur simultaneously and it is difficult to separate their individual consequences on the material's properties. Microstructural anisotropy has been found to be a suitable tool to tailor mechanical properties in terms of combining high strength and fracture toughness or improving the fatigue behavior in certain loading directions [83-85].

Microstructural anisotropy is a common feature of many nanostructured materials. In electrodeposits, plate-like grains (needle-shaped in cross-sections) are regularly observed with the short axis either parallel or perpendicular to the growth direction, depending on the deposition parameters [52]. Besides this self-alignment under constant deposition conditions, an intended modulation of the structure can be realized by changing the deposition parameters during the film growth. This has been demonstrated on multilayer structures of alternating microstructures in pure copper electrodeposits [86], but is mainly used for the deposition of multilayer structures containing sublayers of different chemical composition (and often also different crystallographic structures) [87, 88]. Such multilayer structures can be prepared either by deposition from a single bath, containing all atomic species to be deposited, and the specified modulation of deposition parameters (e.g. current density), or by the sample transfer between multiple electrolytes after the deposition of each sublayer [87]. Both approaches have been applied successfully for a number of systems. Nevertheless, finding appropriate deposition conditions for the single-bath approach and avoiding contamination during the bath transfer in the dual-bath technique is often challenging [87]. Thus, the large majority of investigations on nanostructured multilayer systems have been performed using other bottom-up preparation techniques, in particular magnetron sputtering.

Also SPD techniques are able to produce multilayer-like lamellar structures. HPT of immiscible alloys can result in alternating lamellae with a lamellar spacing of a few nanometers [36, 89]. The creation of such structures necessitates homogeneous codeformation of all phases without destruction of the lamellar structure via shear bands or swirls [90, 91]. Dissolution of one phase via mechanically induced intermixing is supposed to destroy the lamellar structure as well [92]. However, there are also examples showing that segregation at grain boundaries after dissolution of one phase can stabilize the interfaces of a lamellar structure, such as in heavily cold-drawn pearlitic steel [93]. Elongated grains along the shear direction are found in HPT-deformed single-phase materials, too [94]. Whereas their aspect ratio usually varies between one and four [94], aspect ratios of up to eight have been found recently in HPT-treated tantalum [95].

I.4. The Effect of Light Nonmetallic Alloying Elements

The nonmetallic elements, located in the upper part – especially in the first two periods, but to a certain extend also in the third period – of the periodic table, are of special interest as alloying elements in transition metals (and in particular iron) for several reasons. Their small atomic radii give rise to the formation of interstitial solid solutions [96]. The transition to substitutional solid solutions depends on both the solvent and the solute; for iron, the non-metallic elements of the first two periods form interstitial solid solutions (for boron both interstitial and substitutional behavior is reported [97, 98]), whereas larger solute atoms form substitutional solid solutions [99]. Via interstitials, solid solutions of elements with strongly different atomic radii are obtained, since the Hume-Rothery rules [100] do not apply in this case. However, the solute atoms are usually much larger than the interstitial sites of the solvent, limiting the solubility [99]. Due to the small atomic size, the diffusivity of these light alloying elements is high as compared to larger alloying atoms, enabling diffusion over substantial distances in a reasonable time scale, particularly when the characteristic structural size becomes small as in nanostructured materials [99]. For example, carbon has a diffusion coefficient of about 10^{-16} cm^2 s^{-1} in iron at room temperature [101]. Thus, in these structures, carbon atoms move about 15 nm in one hour. Another specific characteristic of the light nonmetallic elements is their high electronegativity, which limits their solubility in transition metals due to the formation of ceramic compounds under (near-)equilibrium conditions. These compounds differ from intermetallic (metal-metal) compounds in their more ionic bonding character. However, often the formation of compounds can be suppressed and metastable supersaturated solid solutions are obtained, especially in nanostructured alloys. The influence of light nonmetallic elements on the properties of alloys have been investigated in countless studies and a complete comprehensive review of all results is almost impossible. Thus, in the following only the most important effects with respect to nanostructured alloys, and in particular nanostructured iron-based alloys, with a focus on materials prepared by HPT or electrodeposition are presented.

Hydrogen, the lightest chemical element, causes embrittlement in many metals and alloys due to either segregation at defect sites or the formation of brittle compounds [102, 103]. For this reason, hydrogen is mostly undesired as alloying element. However, hydrogen is regularly introduced during production of metal parts. For example, electrodeposition of any metal with a negative electrochemical potential from an aqueous electrolyte results in the codeposition of hydrogen, which can either be released in the form of hydrogen gas or remain in the form of atomic hydrogen that can diffuse into the solid [56]. Whereas hydrogen embrittlement of iron and steel via this process is of main industrial importance during the coating of iron-based parts with

other metals such as nickel or chromium, the codeposition of hydrogen also takes place during the deposition of iron and iron-based alloys as the deposition material, as it is investigated in parts of this thesis. Besides embrittlement, codeposition and diffusion of hydrogen results in tensile residual stresses that are inherent to iron-based electrodeposits [15]. On the contrary, hydrogen plays rarely a role during preparation of nanostructured materials via SPD.

For boron, the electrochemical codeposition with the elements of the iron group results in ferritic solid solutions for low boron contents (that go far beyond the solubility according to the phase diagram [104]), whereas with higher boron contents a metastable amorphous phase is formed [104-106]. The analogous behavior of phosphorus is long known [107] and used for the Ni-P coatings that are widely used for example in electronics and automotive industry. For the Fe-P system, the transition from crystalline solid solutions to an amorphous phase is used in this thesis for the preparation of amorphous/crystalline multilayers (chapter III.4). In SPD, these elements are rarely used due to segregation and embrittlement [108-110], but the influence of SPD on previously quenched amorphous alloys has been investigated [111].

On the very opposite, carbon is the most regularly used alloying element in steels, which is reflected in the vast majority of carbon steels in the worldwide steel production. Besides its strong strengthening effect, a large number of materials with different microstructures and properties can be created from carbon steels depending on the processing path. This has also lead to a large number of investigations on the nanostructuring of these materials via top-down methods like HPT. Starting with a near-equilibrium ferritic-pearlitic or fully pearlitic structure, partial dissolution of the cementite has been observed [112-115] and is also known from cold-drawn pearlitic wires [116-121]. Carbon segregation at grain boundaries results in the stabilization of a much finer structure as compared to pure iron. Also for other HPT-treated metals, the effect of carbon, stabilizing dislocations and interfaces via segregation and, thus, resulting in a smaller grain size and higher strength, has been shown [122, 123]. Contrary to these manifold investigations of carbon alloying in HPT, carbon in electrodeposits is often just considered as contamination. A discussion of its impact, possibilities and limits including a comprehensive literature review is given in chapter III.3 and Publication D.

What has been said about carbon, can be transferred to a certain extent to nitrogen. Although much less investigated than carbon, the partial dissolution of nitrides resulting in the stabilization of finer structures with higher strength after HPT deformation has been reported, too [124]. To the author's knowledge, electrochemical codeposition of nitrogen has not been investigated yet.

In contrast to carbon and nitrogen, that are both used for bulk alloying as well as for surface treatments (carburizing, nitriding, carbonitriding, nitrocarburizing [125]) and are considered

generally as intended alloying elements, the light elements of the sixth group of the periodic table, oxygen and sulfur, are often introduced unintendedly as impurities. Their contents are reduced and controlled upon industrial alloy production usually below 50 ppm [126]. The reason for these low contents is, that both oxygen and sulfur segregate at grain boundaries leading to strong embrittlement [127-129]. This also holds after nanostructuring via SPD. However, in this case segregation also results in the formation of finer and stronger structures, similar to carbon and nitrogen [130]. Furthermore, the stabilization of the grain boundaries results in an enhanced thermal stability [130]. For these reasons, certain amounts of oxygen are often accepted in SPD, for example in the powder route of HPT. In electrodeposits, nanostructured deposits can be stabilized by oxygen or sulfur segregation, too. The codeposition of these impurities (depending on the deposition conditions) is long known [15, 52], although the detailed deposition mechanisms are often unclear. Sulfur originates from sulfur-containing components in the electrolyte, such as saccharin, a regularly used grain refiner and brightener [131, 132]. These components are adsorbed at the growth front of the deposit and then partially incorporated and degradated upon further deposition or codeposited via metal sulfides [131]. Either the same mechanism or the incorporation of hydroxides results in the codeposition of oxygen, that will be further discussed in chapter III.3. Briefly, oxygen and sulfur are generally unwanted in nanostructured alloys, but are often accepted to a certain level in order to achieve and stabilize smaller structures.

The halogens and noble gases play no significant role as alloying elements neither in electrodeposition nor in SPD due to their very high and very low chemical reactivity, respectively.

II. Experimental Setups

The nanostructured materials investigated in this thesis were prepared using the two contrary techniques HPT and electrodeposition. The HPT device used in this work has been described in detail in [27]. The maximum load capacity of 400 kN and the necessity of hydrostatic pressures of about three times the flow stress of the material under investigation [32] allows processing of iron-based alloys of up to a sample size of approximately 8 mm diameter (cf. chapter III.2). Deformation at elevated temperatures is facilitated by inductive heating via a water-cooled copper coil and an infrared pyrometer.

The setup for electrodeposition is depicted in Figure 3 and was installed for the experiments of this thesis. It is based on a commercial double-walled corrosion measuring cell connected to a circulation thermostat to adjust the bath temperature during deposition. Additional heating as well as the possibility for bath agitation is provided by a magnetic stirrer placed below the cell. Adaption for the purpose of electrodeposition was realized using costum-made substrate holders based on [133] and various metal rods of about 80 mm in height and 15 mm in diameter, utilized as counter electrodes for the material systems under investigation. Power supply via a computer-controlled IPS Jaissle PGU10V-2A-OEM-MI potentiostat allows the definition of arbitrary temporal profiles of either current density or potential via the corresponding software package. This makes many electrochemical experiments possible, ranging from the deposition under constant conditions over pulse plating and multilayer deposition up to electrochemical measurements such as cyclic voltammetry in both galvanostatic and potentiostatic mode.
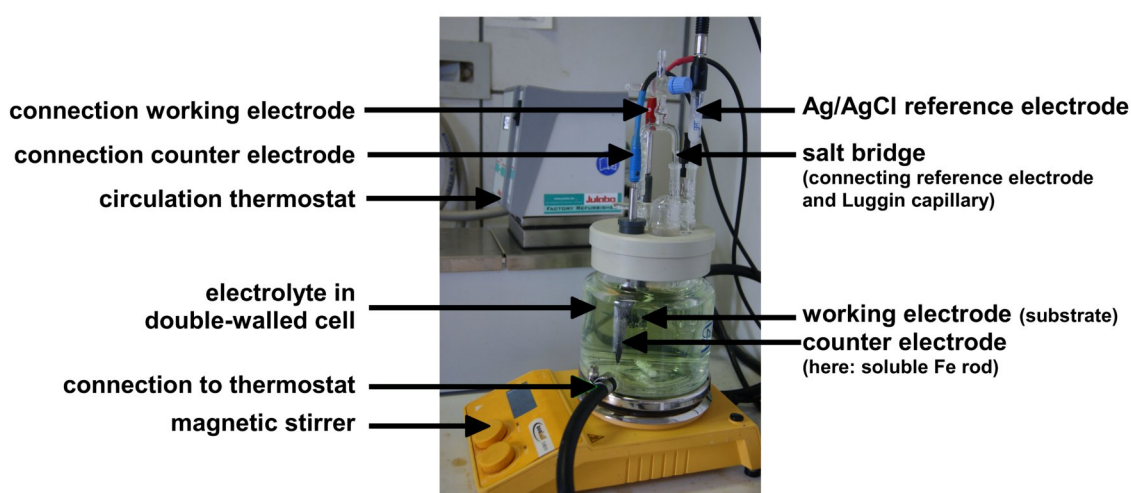

Figure 3: Setup for the electrodeposition experiments in this work.

Most of the samples in this work were deposited on polycrystalline copper discs of 12 mm diameter and about 2 mm thickness, that were mounted in a custom-made holder and aligned vertically in the cell for the deposition process (Figure 3). This sample size is sufficient for microstructural investigations, micromechanics and (subject to the condition that a sufficiently thick film can be deposited) further processing via the HPT device mentioned above or bulk testing techniques that are also used for the HPT samples (e.g. tensile tests as described in [134]). Furthermore, even extraordinary high current densities up to more than 1700 mA/cm², that are rarely reached even in pulse plating, are feasible with this sample size without exceeding the limits of the potentiostat (2A, 10V). An additional benefit in comparison to larger samples is the reduced change of the total bath composition during the deposition process.

III. Results and Discussion

III.1. On the Use of Coated Powders in the HPT Powder Route

The use of powders as starting materials for HPT deformation was already considered in the pioneering work by Bridgman [24]. In modern HPT, in particular powder mixtures, which enable the simple preparation of composites with arbitrary compositions, are widely used [135-142]. The native oxide layer on the metal powder particles stabilizes grain boundaries against both dynamic recovery during the HPT process and grain growth upon subsequent annealing leading to smaller grain sizes, higher hardness and improved thermal stability [130]. One of the main drawbacks of the powder route is the inhomogeneity of consolidated powder mixtures. Several laborious techniques have been developed in powder metallurgy to improve their homogeneity [143]. When powders are mixed in small amounts for the preparation of a few millimeter-sized HPT samples, manual mixing often results in surprisingly homogeneous distributions. However, even in this case, powder mixtures with strongly different particle sizes can result for example in films of the finer powder at the bottom edge of the sample. Such films might result in strain localization and inhomogeneous deformation upon further HPT deformation. For powder mixtures of larger volume, inhomogeneity is an even more severe problem as shown by EDX measurements in Publication A.

For this reason, the use of coated powders as a starting material for HPT was investigated in this work and is presented in Publication A. Fe-Cu was taken as a model system since it is well investigated concerning the HPT deformation of powder mixtures [135, 140]. Iron can be easily coated with copper via immersion coating, as is well-known from the popular school experiment of coating an iron (or steel) nail in cupric sulfate solution [144]. In a simple redox reaction, ions of the more noble copper are reduced at the interface between electrolyte and solid, forming metallic copper, whereas iron atoms at the surface are oxidized and dissolved:

$$Fe + Cu^{2+} \rightleftharpoons Fe^{2+} + Cu \tag{7}$$

However, this idealized process is complicated by several aspects such as the presence of cuprous and ferric ions (Cu^+, Fe^{3+}), incomplete removal of the oxidized iron ions or inhomogeneous coating of the surface area. Thus, the quality of this coating depends strongly on the deposition conditions and, in particular, on the composition of the electrolyte. Some copper-coated iron powder particles obtained from various electrolytes are shown in Figure 4a-c. Citrate-based electrolytes result in a decelerated coating process and a more homogeneous thickness of the coating over the surface area. This observation is in agreement with former findings reported in
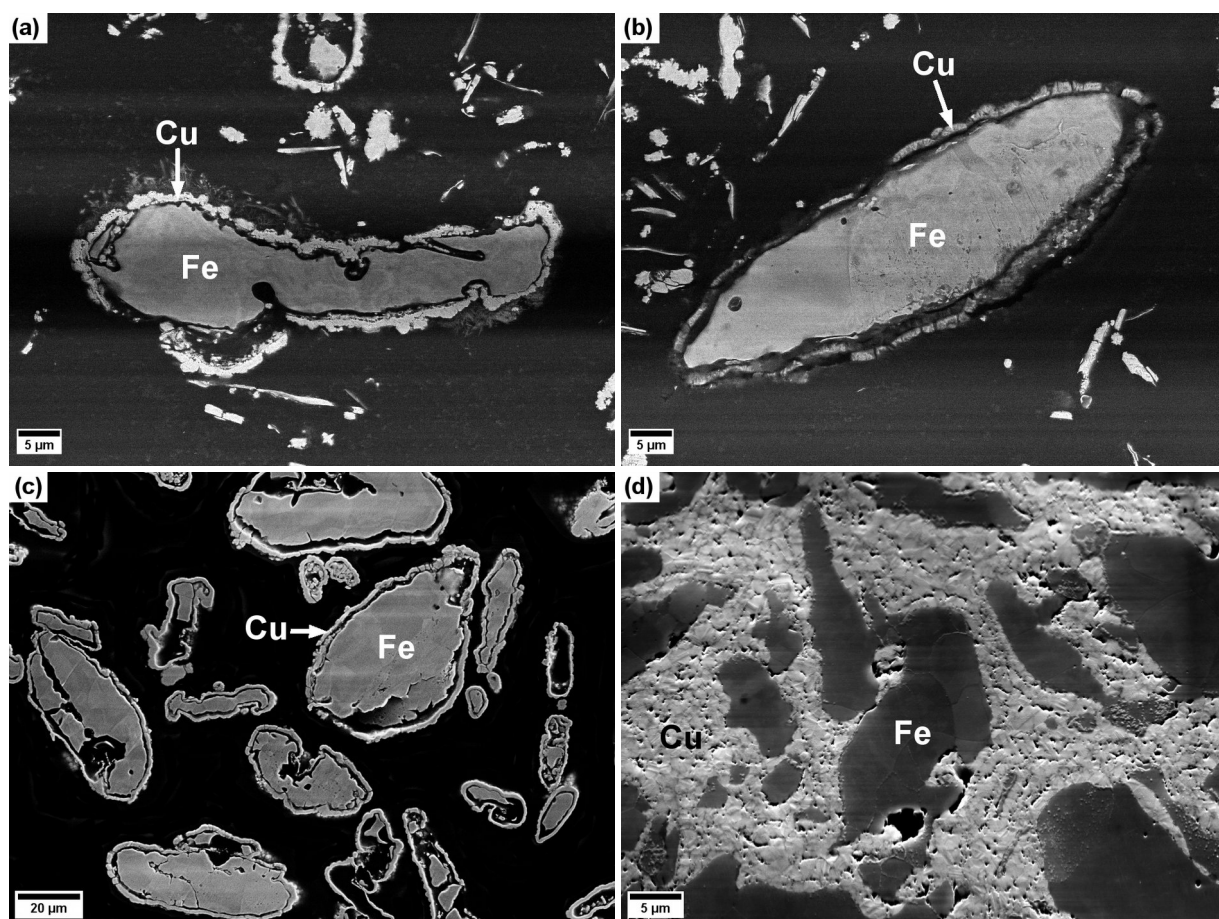
Figure 4: Cross-section SEM images of (a-c) Cu-coated iron powder particles obtained from electrolytes containing (a) 100 g/l CuSO$_4 \cdot$ 5 H$_2$O, (b) 50 g/l CuSO$_4 \cdot$ 5 H$_2$O + 22.6 g/l ammonium citrate dibasic, (c) 200 g/l CuSO$_4 \cdot$ 5 H$_2$O + 117.6 g/l tri-sodium citrate dihydrate and (d) compacted powder obtained from (c) via inductive hot pressing.

literature [145]. For this reason, an electrolyte of 200 g/l cupric sulfate pentahydrate (CuSO$_4 \cdot$ 5 H$_2$O) and 117.6 g/l tri-sodium citrate dihydrate (Na$_3$C$_6$H$_5$O$_7 \cdot$ 2 H$_2$O) was used in Publication A to prepare the coated powders for subsequent HPT deformation. The ultrafine-grained structure of the copper coating, obtained from this electrolyte, is even preserved after compaction via inductive hot pressing (Figure 4d). The comparison to the corresponding powder mixtures shows that the homogeneity of the consolidated powder can be significantly improved by the coating process.

Another consequence of the coating process is also revealed by the cross-sections of the powder particles in Figure 4. The copper layer does not stick directly on the iron, but has a poor adhesion and a black interlayer is formed between the two phases. As confirmed by XRD (Figure 5), magnetite, i.e. iron oxide, results from the coating process. This oxide originates either from oxidation of iron, when immersed in the electrolyte, or from iron atoms, that are reduced during the redox reaction of the coating process and not dissolved in the electrolyte, but rather

transformed into oxide via a chemical reaction with oxygen from the bath. Although some oxygen contamination is also present in powder mixtures due to the native oxide layers of the powder particles, no oxide is detectable in the XRD patterns, indicating lower oxygen contents than for the coated powder samples (Figure 5). No oxides are detected via XRD in the HPT-deformed samples from both coated powders and powder mixtures which is due to their refinement and (partial) dissolution. However, the higher oxygen content is still present in the coated powder samples and results in crack formation during HPT deformation at room temperature and higher strength due to stabilization of smaller grains after HPT at elevated temperatures, as discussed in Publication A.
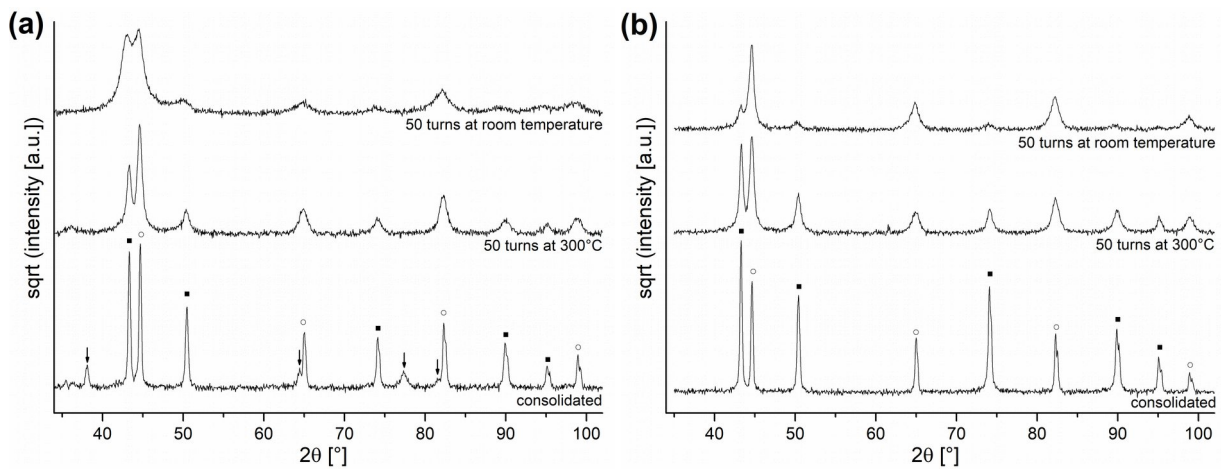

Figure 5: XRD patterns of (a) copper-coated iron powder and (b) Fe/Cu powder mixtures after powder consolidation and after subsequent HPT deformation. ■ and ○ indicate the Bragg peaks of Cu and Fe, respectively. The visible oxide peaks are marked with arrows.

III.2. Severe Plastic Deformation of Martensitic Carbon Steels

The probably best investigated system concerning supersaturated solid solutions are carbon steel martensites. These solid solutions of carbon in a ferritic matrix have found their way into many introductory classes and textbooks of materials science [146-148] due to their industrial importance for the production of hardened steels. Although carbon steel martensites can be considered as a single-phase material, their actual structure deviates from the standard textbook knowledge of carbon atoms homogeneously distributed on the interstitial sites of the ferritic lattice causing solid solution strengthening. They rather consist of inhomogeneous carbon distributions providing high strength via segregation-stabilized dislocations and grain boundaries [149-151]. Thus, the main structural difference as compared to heavily cold-drawn pearlitic steel wires – the strongest steels known today with a tensile strength of up to almost 7 GPa after mechanically induced dissolution of the cementite phase [93] – is not the carbon distribution, but the larger grain size and the large amount of grain boundaries with specific orientation relationships. Grain refinement and the destruction of ordered interfaces is usually achieved much faster via HPT compared to the complete dissolution of a phase via mechanically induced intermixing. For this reason, the HPT deformation of martensitic steels was investigated in the present work as a possibly effective alternative way to create structures comparable to heavily deformed pearlite.

For low carbon steels, the preparation of fully martensitic samples is challenging due to their high martensite start temperature leading to the precipitation of carbides via autotempering already during quenching [150, 151]. Quenching of small volumes, than means quenching of individual HPT samples (discs of 8 mm diameter, final thickness 0.8 mm), in salt water provides the most efficient way to obtain rapid cooling throughout the whole sample. However, even in this case a
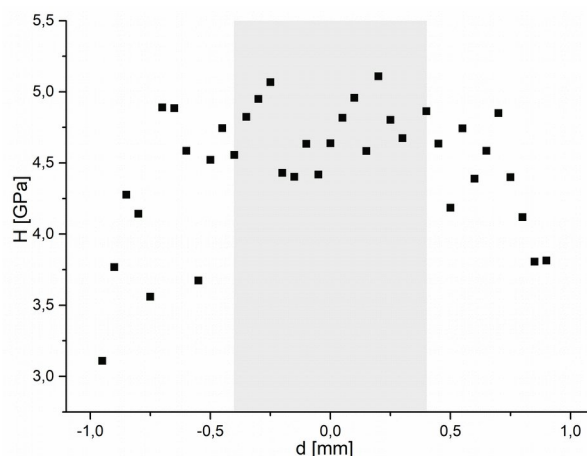

Figure 6: Hardness profile over the height of a as-quenched martensitic Ck10 sample as obtained from nanoindentation with a cube corner indenter with a maximum load of 6 mN. The gray area indicates the approximate region that was used for HPT deformation after grinding from both sides.

softer structure is formed next to the surface (Figure 6). This is caused either by decarburization during annealing or by carbide precipitation during cooling in air in the short moment between taking the sample out of the furnace and getting in contact with the salt water. Any inhomogeneity of the as-quenched material might result in inhomogeneous, localized deformation during HPT. Indeed, inhomogeneity due to pronounced deformation of this soft surface layer was observed when the whole sample volume was used for HPT deformation. For this reason, both the oxide layers and the soft surface layer have to be removed (e.g. via grinding) prior to the HPT treatment in order to obtain homogeneous deformation.

Whereas the as-quenched structure of Ck10 steel (0.1 wt.-% C) is a typical lath martensite with elongated grains (laths) of random orientation in the sample (Figure 7a), elongated grains strongly aligned along the shear direction are obtained after HPT. The grain size decreases with increasing plastic strain and is approximately 30 nm at a radius $r = 3$ mm after one turn ($\varepsilon_{vM} = 15$) in axial direction (cf. TEM images in Publication B). However, the applicable strain via HPT is limited due to crack formation which is often observed after one turn in the higher-strained outer part of the samples and expands towards the center upon further deformation. Nevertheless, already the deformation by one turn results in nanocrystalline structures with a hardness of up to about 750 HV, which is more than what can be accessed via 20 turns of HPT deformation from the as-received ferritic-pearlitic structure (Figure 7b). Tensile tests show that the Ck10 martensite after one turn HPT has an ultimate tensile strength of 2.4 ± 0.1 GPa, which is more than ever reported for a carbon steel with such low carbon content. This enormous strength, a more detailed analysis of the microstructure as well as the mechanical behavior of this HPT-treated martensite in micro-pillar compression tests, showing strong similarity to HPT-deformed pearlite [152], are discussed in Publication B. Furthermore, a systematic comparison of combined HPT and heat treatments in any temporal sequence has been performed for the Ck10 martensite and is presented in Publication C. It is shown that each processing sequence, i.e. heating prior, during or after HPT processing, has different consequences for the structure of the final material and has to be taken into consideration in order to tailor and optimize the properties for individual applications.
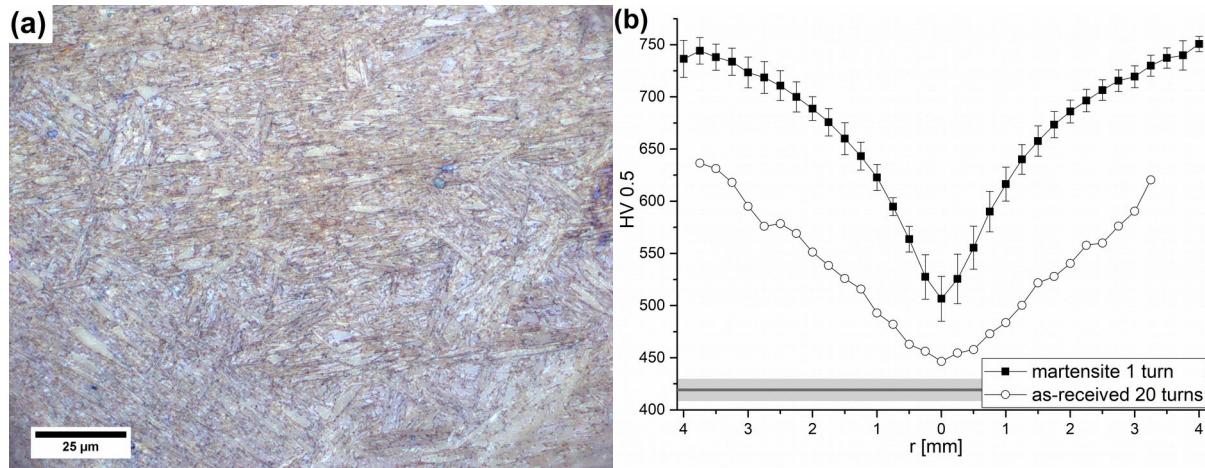
Figure 7: Microstructure and hardness evolution of martensitic Ck10 steel upon HPT deformation. (a) Optical micrograph of the as-quenched structure (etched with sodium disulfite solution). (b) Hardness profile of martensitic Ck10 after one turn HPT compared to as-received, ferritic-pearlitic Ck10 after 20 turns HPT. The gray horizontal line indicates the hardness of the as-quenched martensite plus/minus standard deviation.

For carbon steels with higher carbon contents, the lower martensite start temperature facilitates the suppression of carbide precipitation during quenching. However, the increasing hardness of martensite with increasing carbon content makes its deformation via HPT experimentally challenging. The hardness evolution of a martensitic Ck35 carbon steel (0.35 wt.-% C) upon HPT treatments is shown in Figure 8a. The hardening does not only depend on the applied shear strain, but deviates for identical strains applied via different numbers of rotations at different radii, indicating a decreased hardening rate with increasing number of rotations (Figure 8a). A similar phenomenon appears for the Ck10 martensite from a certain amount of strain on and is attributed to crack formation (cf. Publication B). However, this explanation does not hold for the Ck35 martensite since the phenomenon occurs before any cracks are present. Due to the higher carbon content, this material reaches and exceeds the hardness of the anvils which were made of a S390 high-speed steel with a hardness of about 800 HV for the experiments in this work. Thus, the shear strain is not concentrated in the sample, but is partially relocated into the anvil material. Plastic deformation of the anvils, i.e. change of the cavity shape by the HPT experiment, was also observed experimentally. The fraction of shear strain, that is taken over by the anvil material, increases with increasing number of rotations due to the hardening of the sample causing the apparent decrease of the hardening rate in Figure 8a. Nevertheless, the hardness profiles indicate grain refinement, that is also observed in the corresponding micrographs although the grains are not well-aligned in the shear plane (Figure 8b+c). On the other hand, also slippage between the anvils and the sample becomes a concern for the martensitic Ck35 due to the enhanced hardness exceeding the maximum hydrostatic pressure supplied by the HPT machine.
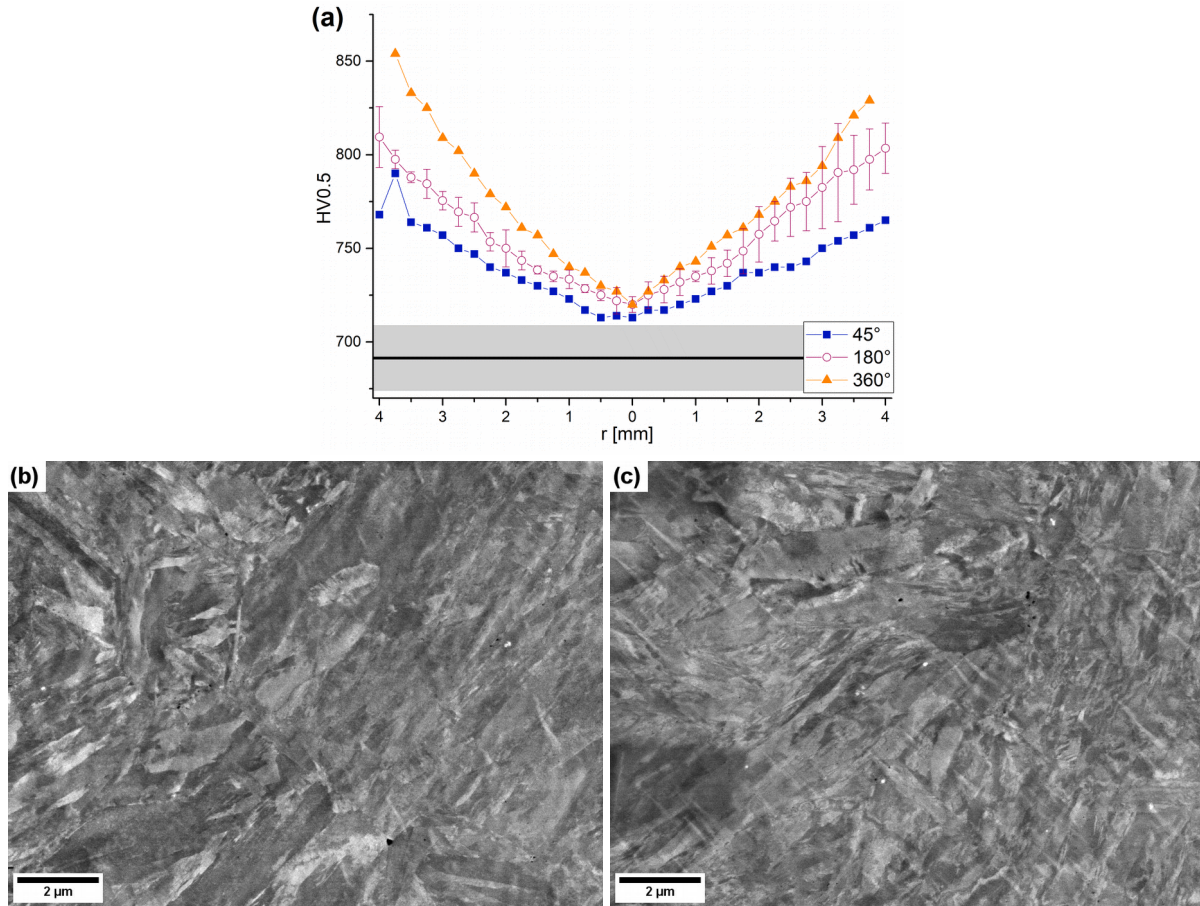
Figure 8: (a) Hardness profiles of martensitic Ck35 steel after different HPT treatments. The gray horizontal line shows the hardness in the as-quenched state plus/minus standard deviation. (b+c) Microstructure of martensitic Ck35 deformed via HPT by 90° at a radius of (b) r = 1mm (ε_{vM} = 1.1) and r = 3mm (ε_{vM} = 3.4) in tangential view.

These experimental problems during HPT deformation become more severe for even higher carbon contents. For a martensitic Ck60 steel (0.60 wt.-% C), the hardness in the as-quenched state equals 822 ± 15 HV and, thus, already exceeds the hardness of the anvils. Although a hardness increase up to more than 1000 HV is accessible via HPT (Figure 9a), no alignment of the elongated grains in the shear plane is obtained (Figure 9b). Instead, very fine lamellar structures with a lamellar spacing of less than 10 nm occur locally, as observed in both SEM and TEM (Figure 9b+c). These lamellae do not have any specific orientation with respect to the shear direction. Although their nature was not investigated further until now, they might be twins, as regularly observed in martensitic carbon steels with high carbon contents [153]. In contrary to the negligible amount of retained austenite in the martensitic Ck10 low carbon steel (cf. Publication B), about 5 wt.-% retained austenite are present in the as-quenched Ck60 martensite according to Rietveld refinement of the XRD data shown in Figure 9d. It is reduced to 3.5 wt.-% by the application of the hydrostatic pressure in the HPT device prior to any shear deformation. Torsion results in further reduction of the retained austenite content (Figure 9d). The observed transformation of the retained austenite under compressive stress agrees well with reports on mechanically induced transformation of retained austenite in various carbon steels [150,154,155].
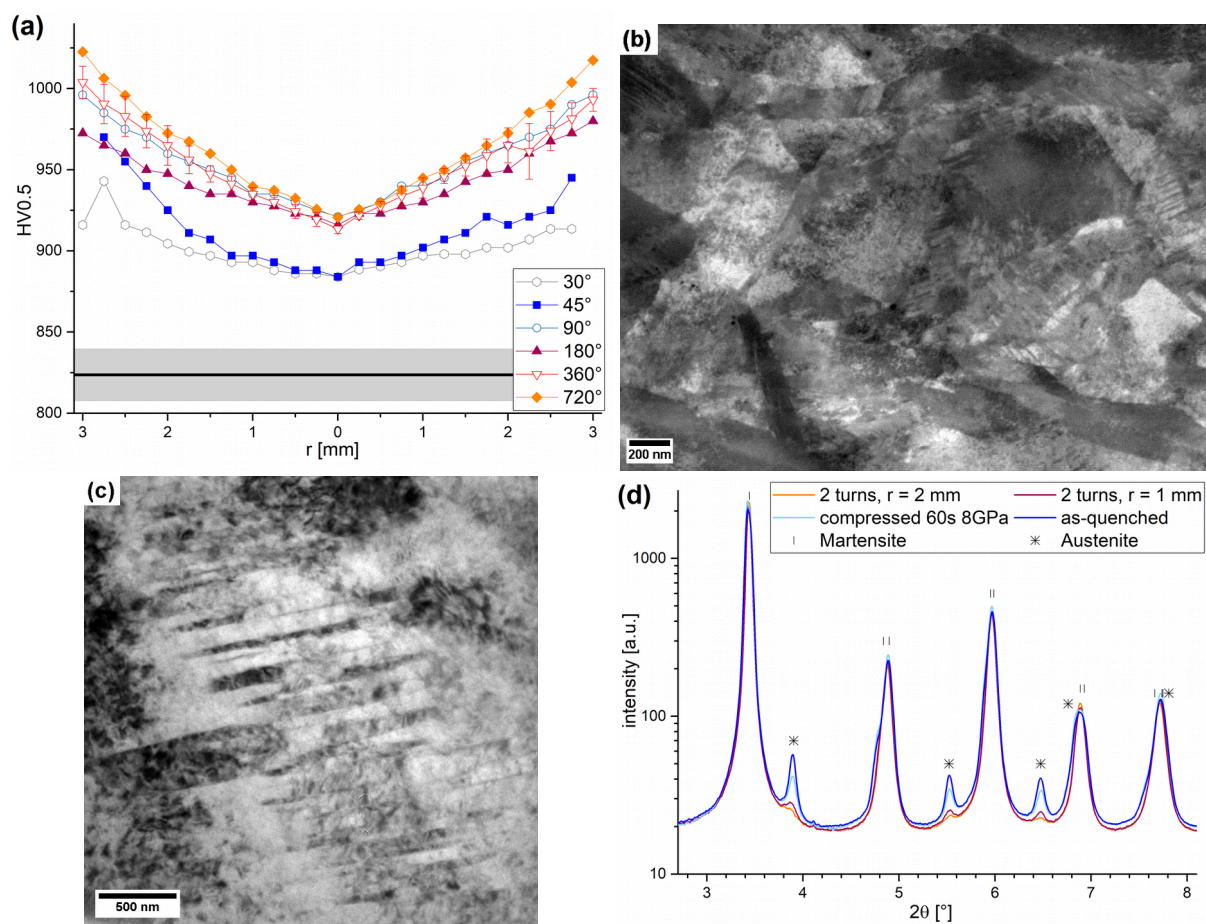
Figure 9: Hardness and structure of martensitic Ck60 after HPT treatments. (a) Hardness profiles. The gray horizontal line shows the hardness in the as-quenched state plus/minus standard deviation. (b) SEM micrograph in tangential direction after 90° HPT at radius *r* = 3 mm (c) TEM image recorded in tangential direction after two turns HPT at radius *r* = 2.5 mm (d) Integrated patterns of high-energy XRD performed at the beamline P07 of PETRA III [156].

Although the retained austenite might cause problems upon deformation in terms of strain localization, the primary experimental challenge for HPT of martensitic medium and high carbon steel is the codeformation of the anvils. HPT anvils made of hard metal have already been used for various systems [30, 157, 158]. However, preliminary HPT experiments using hard metal anvils have revealed their brittleness as the crucial factor for the deformation of martensitic Ck60 steel. Failure of either the anvil material next to the cavity or of a whole anvil – often already in the initial loading step – has prevailed any homogeneous HPT deformation of Ck60 martensite so far. Besides the availability of a suitable anvil material, the question of the optimum surface morphology in the cavity of the anvils arises. The morphology directly determines the friction coefficient between anvil and sample, which has large impact on the homogeneity of the HPT deformation [159, 160]. SEM investigations reveal fundamental differences in the surface morphology of steel anvils, that are usually roughened via sand blasting, and hard metal anvils roughened via etching (Figure 10). To optimize the processing of extremely hard material, further research in this field is necessary which might include the comparison of practically available surface morphologies in experiments and simulations.
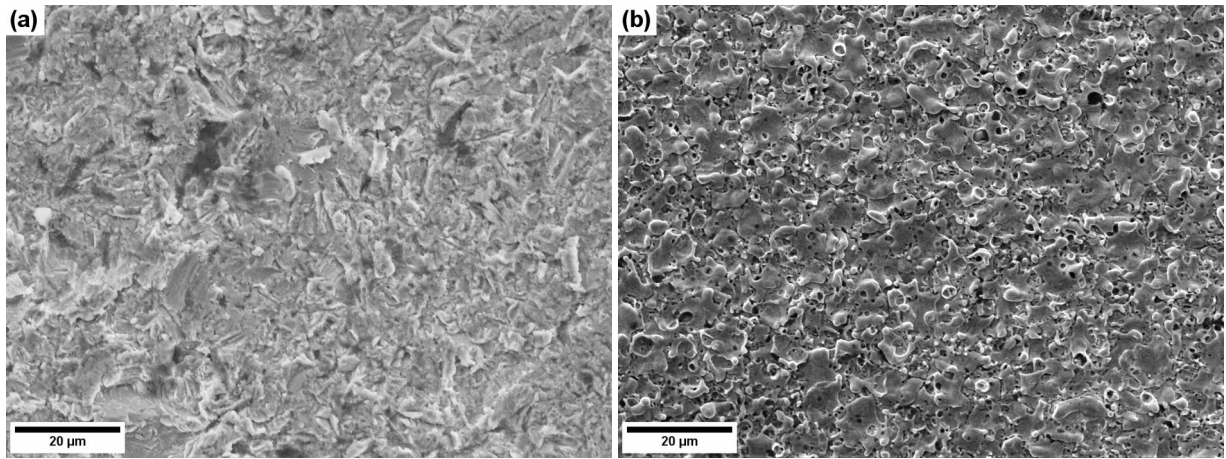
Figure 10: SEM micrographs of (a) a sandblasted S390 steel anvil and (b) an etched hard metal anvil.

III.3. Electrodeposition of Fe-C Alloys

The incorporation of foreign substances such as hydroxides, organic species or other bath components in electrodeposits is long known [52]. Many of these substances consist mainly of light elements, in particular hydrogen, carbon and oxygen. In spite of the significant effect of light alloying elements in metals and alloys (cf. chapter I.4), they are often only considered as impurities and little attention is paid to their codeposition. Considering the huge scientific and industrial impact of carbon steels and the strong dependence of their properties on the carbon content, the codeposition of carbon with iron, i.e. the electrochemical preparation of Fe-C alloys, was investigated in this work.

Previous studies have shown that carbon is codeposited with iron from different electrolytes containing hydroxy-polycarboxylic acids or dicarboxylic acids [161, 162]. Carbon contents of about 1 wt.-% are achieved with the most regularly used electrolytes, which are based on ferrous sulfate and citric acid [163-168]. Fe-C electrodeposits consist of a martensitic structure, i.e. a supersaturated solid solution of carbon in a ferritic matrix, but with a much smaller tetragonal distortion as expected from metallurgically prepared martensite of the same composition [165]. Although a hardness of up to 810 HV [168] and an additional hardening capacity upon annealing [164, 165] make these deposits potential candidates for high-strength materials, previous mechanical characterization has been restricted to microhardness testing and one wear test study [169]. A full review of the manageable number of previous investigations on Fe-C electrodeposition is given in Publication D.

The aim of the present work was to test the potential of electrodeposition to create thick layers of nanostructured Fe-C alloys and to compare their microstructure and mechanical properties to that of other nanostructured bulk Fe-C alloys. To prepare thick samples in reasonable time, deposition at high current densities with reasonable current efficiency is an essential prerequisite. High current densities can usually be realized in electrolytes containing high ion concentrations and conductive salts. For this reason, the suitability of a new citrate-based electrolyte, that was adopted from a similar bath for the electrodeposition of cobalt [170] and that is more concentrated compared to the Fe-C electrolytes in literature, was tested for the electrodeposition of Fe-C. First, tests were performed with film thicknesses of a few tens of microns. Next, the most promising deposition conditions were used to prepare films with a thickness in the range of several hundred microns.

Figure 11a shows the current efficiency and microhardness of electrodeposits with a nominal thickness of 25 μm, which were deposited from an electrolyte consisting of 139 g/l ferrous sulfate heptahydrate ($FeSO_4 \cdot 7\ H_2O$), 59 g/l tri-sodium citrate dihydrate ($Na_3C_6H_5O_7 \cdot 2\ H_2O$), 3 g/l
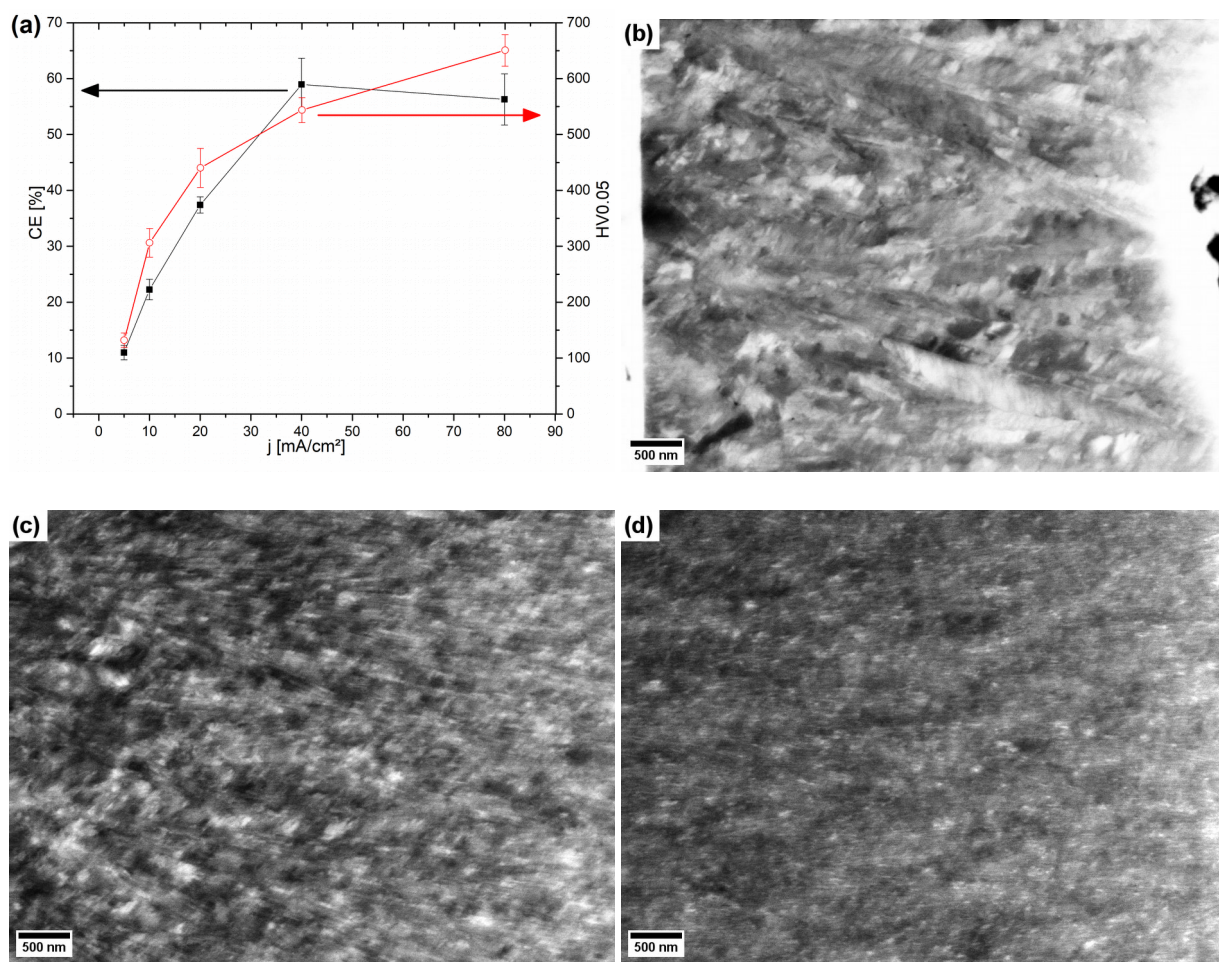
Figure 11: (a) Current efficiency (CE) for electrodeposition of Fe-C films with a nominal thickness of 25 µm and hardness HV0.1 of the corresponding deposits. (b-d) Cross-sections of deposits obtained at current densities of (b) -10 mA/cm². (c) -20 mA/cm² and (d) -80 mA/cm².

ascorbic acid ($C_6H_8O_6$) and 0.2 g/l sodium dodecyl sulfate ($NaC_{12}H_{25}SO_4$) at 75 °C under different current densities. The hardness increase with increasing current density is based on a decrease in grain size from the micron to the nanometer range. Deposits, which were prepared with a current density of -20 mA/cm² or more, consist of elongated grains with a width of about 20 nm (Figure 11c-d). For -10 mA/cm², this structure is already present in parts of the film, but still coexists with coarser, equi-axed grains (Figure 11b). XRD reveals the presence of a single bcc phase in the deposits for all current densities (Figure 12a+b). The high current efficiencies at high current densities (Figure 11a) resulting in a nanocrystalline structure make this electrolyte a promising candidate for the deposition of thick, nanostructured Fe-C films.

Upon annealing, precipitation of cementite is observed for the films deposited at current densities of -10 mA/cm² or more, whereas at -5 mA/cm² no additional phases occur (Figure 12a+b). This proves the codeposition of carbon at high current densities, which is in agreement with literature [164, 165]. However, not all Bragg peaks can be attributed to ferrite and cementite, but are explained by the additional presence of magnetite, implying the additional codeposition of
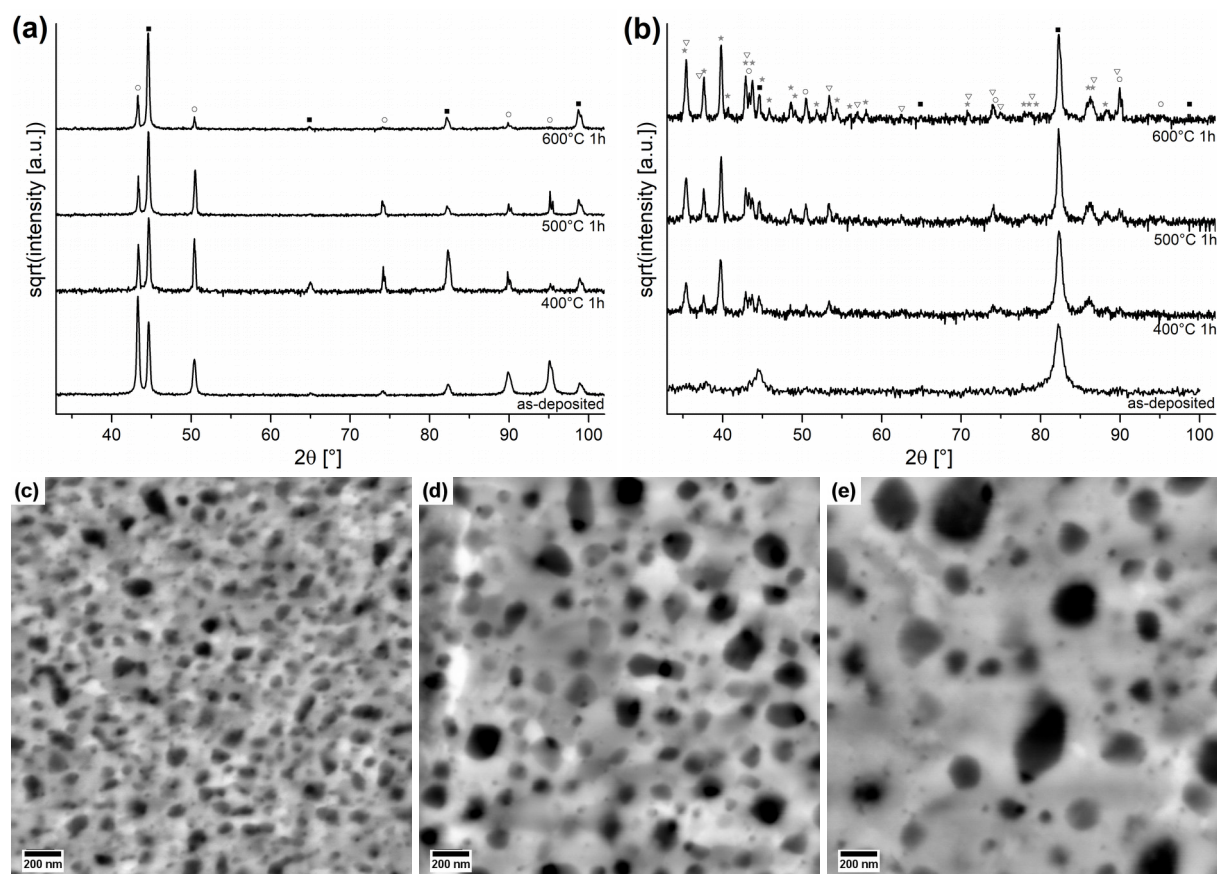
Figure 12: Annealing behavior of Fe-C films with a nominal thickness of 25 μm. (a+b) XRD patterns after different isothermal annealing treatments of films deposited at (a) -5 mA/cm² and (b) -80 mA cm-². Bragg peaks are indicated for iron (■), the copper substrate (○), cementite (★) and magnetite (▽). (c-e) Microstructure of deposits obtained at a -80 mA/cm² after annealing at (c) 500 °C, (d) 600 °C and (e) 700 °C. All annealing treatments were performed for one hour in a vacuum furnace at about 10^{-5} mbar.

oxygen (Figure 12b). Codeposition of oxygen with iron and Fe-C alloys has been reported in previous investigations, but the oxygen amounts differ in a large range [165, 169, 171]. The cementite and magnetite precipitates are of approximately spherical shape and grow in size with increasing annealing temperature (Figure 12c-e).

The electrolyte is suitable for deposits up to a thickness of about 300 μm. However, further expansion of the deposition process results in massive incorporation of ceramic particles in the deposits. Although not experimentally proven, the ceramic particles are probably hydroxides that form when the pH of the electrolyte in the vicinity of the working electrode is increased upon a certain threshold value due to hydrogen reduction. The appearance of the particles is shifted to larger deposit thicknesses by further improvements of the deposition conditions. Sodium dodecyl sulfate is a surfactant, commonly used to improve the smoothness of electrodeposits [172]. However, in the present case, it limits the maximum thickness of homogeneous films and promotes the formation of the ceramic particles. Without sodium dodecyl sulfate, homogeneous films with a thickness of more than 500 μm are producible.

These films still consist of a single bcc phase and have a strong 211 fibre texture, as shown by high-energy XRD measurements with synchrotron radiation at the P07 beamline of PETRA III (Figure 13) [156]. The line broadening in diffraction patterns integrated ±10° around the in-plane direction of Figure 13b indicates a domain size of 26 ± 6 nm according to the Williamson-Hall method [173, 174]. This is in good agreement with the approximately 20 nm found in the SEM over the whole film thickness. The average hardness of the films is 657 ± 32 HV with a slight increase with increasing distance from the substrate. This is in contradiction with commonly observed increase in grain size causing a decreasing hardness with increasing deposition time in many electrodeposits [175, 176]. It might be caused by an increase of hydroxide incorporation due to the increase of pH during the experiments.

The suitability for thick film deposition of a slightly further improved electrolyte and the structure and properties of the corresponding deposits compared to those from another electrolyte from literature [168] are discussed in Publication D. The new electrolyte is well-suited for the deposition of thick films due to higher usable current densities, that means higher growth rates. However, the codeposition of oxygen and its segregation at grain boundaries result in embrittlement of the deposits limiting their mechanical load bearing capacity.

The codeposition of carbon is caused without doubt by the incorporation of molecules of citric acid, sodium citrate, ascorbic acid or degradation products of those, since further carbon-containing species are not present in the electrolyte. On the contrary, the origin of codeposition of oxygen can be twofold. On the one hand, oxygen might originate from the incorporation of the same species as carbon, since all of them also contain oxygen atoms. On the other hand, the
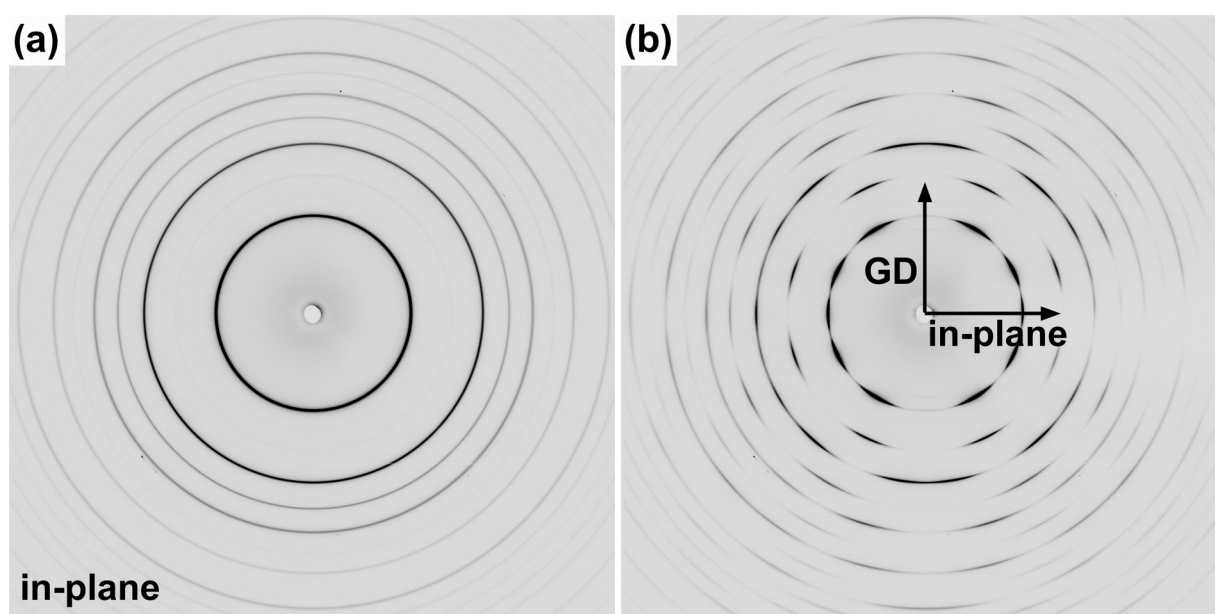

Figure 13: High-energy XRD patterns of a thick Fe-C electrodeposit recorded in transmission with the primary beam (a) in growth direction and (b) in-plane (GD indicates the growth direction).

incorporation of hydroxides is also well-known [52]. The comparison of the chemical structure of the organic bath components with the carbon and oxygen contents of the films (cf. Publication D) indicates, that hydroxide incorporation accounts for the main fraction of oxygen in the films. This agrees with the reduced oxygen incorporation reported for electrolytes spoiled with inert gas or containing boric acid [171].

For this reason, the use of citrate buffer solutions was investigated. The goal was to stabilize the pH next to the working electrode and avoid hydroxide incorporation. Table 2 summarizes the hardness and current efficiency of deposits from several citrate buffer solutions. Both are lower than for the electrolytes used in Publication D. Furthermore, XRD of annealed samples reveals no significant reduction of the oxygen content. These result indicate that citrate buffer solutions do not provide a way to improve the electrodeposition of Fe-C alloys.

Table 2: Hardness, current efficiency and pH change of Fe-C electrodeposits from citrate buffer solutions. All samples were deposited with a current density of -30 mA/cm² for 22 hours at 50 °C. The values obtained for the electrolytes from Publication D are given for comparison.

Electrolyte Components (besides 120 g/l FeSO$_4$ · 7 H$_2$O)	HV0.5	CE_d	pH$_{t=0}$	pH$_{t=22h}$
22.7 g/l citric acid, 24.1 g/l tri-sodium citrate dihydrate	603±6	6 %	3.0	3.0
15.8 g/l citric acid, 5.3 g/l tri-sodium citrate dihydrate	608±15	11 %	2.3	2.5
16.8 g/l citric acid, 47.8 g/l tri-sodium citrate dihydrate	588±8	16 %	3.6	3.5
6.7 g/l citric acid, 19.1 g/l tri-sodium citrate dihydrate	605±11	24 %	3.1	3.6
11.3 g/l citric acid, 12.1 g/l tri-sodium citrate dihydrate	619±17	27 %	2.8	3.1
11.3 g/l citric acid, 12.1 g/l tri-sodium citrate dihydrate, 3g/l ascorbic acid	621±6	25 %	2.9	3.0
Bath A50 from Publication D	556±10	54 %	4.2	4.3
Bath A65 from Publication D (-50 mA/cm² at 65°C)	662±28	45 %	4.2	4.4
Bath B50 from Publication D	660±17	41 %	2.5	3.2

III.4. Electrodeposition of amorphous/crystalline multilayers

Similar to the bulk lamellar structures considered in the previous chapters, also multilayer films, that can be produced with a sublayer thickness in the nanometer range via bottom-up preparation techniques, have been attracted much attention in the last decades [15, 87, 177, 178]. Concerning mechanical behavior, multilayer structures composed of crystalline and amorphous sublayers are of particular interest due to the different deformation mechanisms and their interaction at the interfaces [179-182]. Several studies on the mechanical behavior of sputtered amorphous/crystalline multilayers films have shown that the crystalline sublayers prevent shear localization and catastrophic failure of the amorphous structure in a localized shear band, whereas the addition of the amorphous component enables higher strengths as compared to purely crystalline films [181, 182]. Although the possibility to produce certain amorphous/crystalline multilayer films via electrodeposition is already known since the 1980s [183], their mechanical behavior has been rarely investigated yet.

Electrodeposits of Ni-P, Co-P and Fe-P behave similar in terms of the transformation from crystalline to amorphous structure with increasing phosphorous content and the dependence of the phosphorous content on the current density [107]. Whereas only the amorphous Ni-P and Co-P alloys have been used in electrodeposited amorphous/crystalline multilayer structures so far, the electrodeposition of multilayer structures of alternating crystalline and amorphous Fe-P alloys were investigated in the present work. Publication E shows that the hardness of such structures obtained via the single-bath electrodeposition technique depends on the sublayer thickness of the crystalline layers. For a sublayer thickness of more than 15 nm, the size effect is well described by a Hall-Petch relation, whereas a hardness plateau is obtained for thinner sublayers. Furthermore, the microbending experiments in Publication E show, that crack deflection can be achieved by a proper choice of the sublayer thickness.

However, it is also shown that the structure of alternating amorphous and crystalline layers breaks down below an average sublayer thickness of 15 nm, which might be related to the roughness of the layers exceeding the sublayer thickness. The roughness of the amorphous/crystalline multilayer deposits increases during the deposition process, as was proven by roughness analysis of SEM cross-sections via manual color-coding of the sublayer interfaces (Figure 14a) and subsequent automated roughness analysis. This analysis method allows to extract the roughness evolution upon deposition from a single sample, significantly reducing the sample preparation work in comparison to the whole series of samples that would be necessary to obtain similar data via surface investigations using atom force microscopy. Furthermore, scatter among different samples can be ignored for the analysis of the roughness evolution under fixed conditions (i.e.
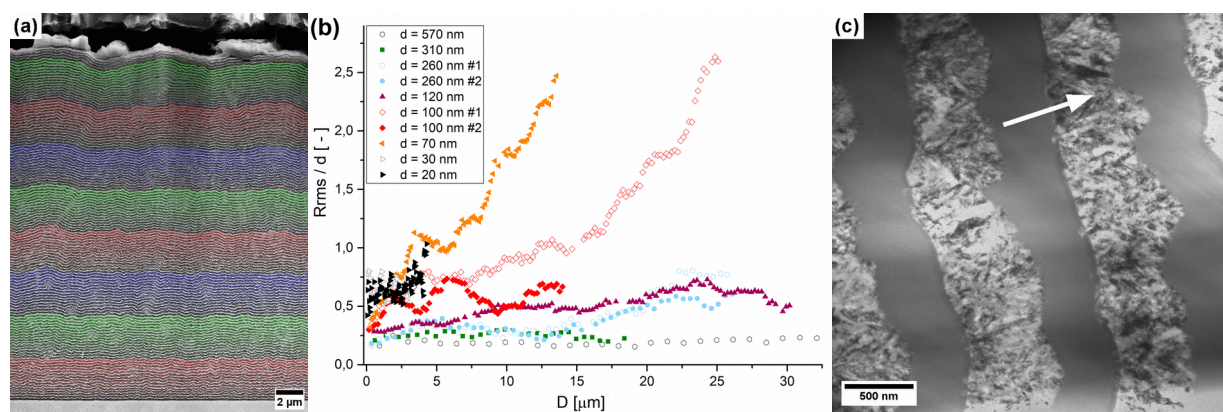
Figure 14: Roughness analysis of amorphous/crystalline multilayer electrodeposits. (a) Exemplary color-coded SEM image from the roughness analysis. (b) Evolution of the ratio of roughness to sublayer thickness during the growth process of multilayer structures with different sublayer thicknesses. For two samples, two different SEM images from the same sample were analyzed, indicated by #1 and #2. (c) TEM bright-field cross-section of a deposit with an average sublayer thickness of 250 nm showing roughness reduction during growth of the amorphous layers. The white arrow indicates the growth direction.

within one sample) and only becomes important for the comparison of different conditions (e.g. different sublayer thicknesses). The observed roughness increase with increasing film thickness is a common phenomenon in electrodeposits [15]. The absolute roughness increases with increasing sublayer thickness. However, the ratio of the roughness to the sublayer thickness increases with decreasing sublayer thickness (Figure 14b). Therefore, the loss of the multilayer structure might be caused be the roughness, as discussed in Publication E. Unfortunately, the accuracy and the film thickness range, that is explorable with this roughness analysis method, decreases with decreasing sublayer thickness due to the need of SEM images with sufficient resolution to detect the interface profiles. For this reason, only parts of the total films could be analyzed for the thinnest layers (Figure 14b).

TEM investigations indicate a decrease of the interface roughness during the growth of amorphous sublayers (Figure 14c) that is superimposed by the roughness increase upon the growth of the subsequent crystalline layer resulting in the overall roughness increase, discussed above. Therefore, the increase of the thickness of the amorphous sublayers with respect to the crystalline sublayers might reduce the overall roughness and might path the way to multilayer structures with even thinner crystalline layers in the future.

Incorporation of hydroxides or phosphides is discussed in Publication E as a possible reason for structural defects, resulting in a large scatter of nanoindentation and microbending data and contributing to the brittleness of the deposits. Reduction of the amount of sodium hypophosphite in the electrolyte was found to increase the bath stability, which might result in less codeposition of unintended species and improve the properties of the deposits. Indeed, multilayer structures are obtainable from electrolytes containing only 1 g/l sodium hypophosphite hydrate (in Publication

E: 15 g/l). However, substructures in the amorphous layers are visible in the SEM (Figure 15a) indicating that these layers are not fully amorphous. This hypothesis is supported by XRD measurements revealing no amorphous phase in the deposits (Figure 15b). For this reason, the mechanical analysis in Publication E was performed with deposits from the less stable electrolyte containing 15 g/l sodium hypophosphite hydrate.

The analysis of the effect of the sublayer thickness on hardness in Publication E shows a Hall-Petch behavior with a Hall-Petch constant comparable to interstitial-free steels as expected for Fe-P alloys. It is known from literature that the Hall-Petch constant of carbon steels is higher compared to interstitial-free steels by a factor of at least four [184]. Such an increase of the Hall-Petch constant would further increase the hardness of the nanostructured multilayers. For this reason, the addition of citrate and ascorbic acid, as used for the deposition of Fe-C alloys in the previous chapter, was investigated. However, the presence of ascorbic acid impedes the phosphorus codeposition. No indications of an amorphous phase were found after addition of 3 g/l ascorbic acid to the electrolyte described in Publication E. For this reason, the two-bath multilayer deposition technique would be necessary in order to produce structures, including both an amorphous and a carbon-containing phase. With this technique, the phosphorous content of the crystalline sublayers could be reduced to zero, reducing the brittleness of the structures. However, multilayer deposition with the two-bath technique is beyond the scope of the present work since it requires special experimental setups as described in [183] and is further complicated in the case of iron-based deposits due to their fast oxidation.
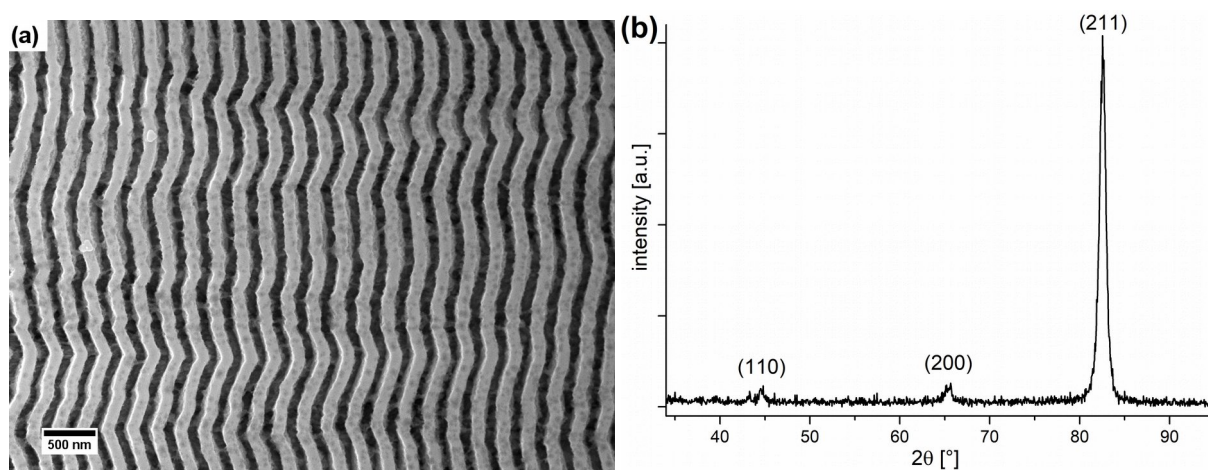

Figure 15: Fe-P multilayer structures deposited from a bath with 1 g/l sodium hypophosphite hydrate.
(a) SEM image of an etched cross-section with 122 nm average sublayer thickness.
(b) XRD pattern of a sample with 39 nm average sublayer thickness.

IV. Conclusions

The results of the present work show that the efficiency of HPT deformation in multi-component systems can be significantly enhanced using starting materials with a fine and homogeneous structure. The shorter distances for mechanically induced intermixing – or even its anticipation in the case of atomically mixed starting materials – give rise to much finer and stronger materials after moderate strains applied via HPT. Although this approach can principally be transferred to arbitrary multi-component systems and arbitrary ways of homogenization, specific peculiarities are inherent to each system and processing procedure. In the first model system, copper-coated iron powder, the incorporation of oxides during the coating process results in an additional strengthening effect and some thermal stability, but also in enhanced brittleness of the HPT-treated composites. The second model system, quenched carbon steel martensite, differs from other quenched solid solutions (in particular metal-metal solid solutions) concerning the high mobility of the solute carbon atoms. Therefore, the single phase starting material not only eliminates the mechanically induced intermixing during HPT, but the carbon atoms can segregate and, thus, stabilize also new dislocations and grain boundaries, that are created during deformation. This results in the extraordinary strength of the HPT-deformed structure, that is already obtained after moderate strains of one turn HPT.

Stabilization of grain boundaries via segregation is also the basis for the fine structure, high hardness and considerable thermal stability of the Fe-C electrodeposits under investigation. However, the segregation of codeposited oxygen makes these nanostructures extremely brittle and results in catastrophic failure already at low mechanical loads. On the contrary, the mechanical properties of the electrodeposited amorphous/crystalline Fe-P multilayers can be varied over a large range via modification of the sublayer thickness, i.e. via the deposition parameters. The results show that electrodeposition is a suitable technique to produce high-strength nanostructured iron-based materials if the codeposition of impurities and other strength-limiting effects such as residual stresses or roughness can be kept at an acceptable level. However, this is more laborious in the case of iron-based alloys as compared to the electrodeposition of metals such as nickel, which have already been widely investigated in previous works.

V. References

1   M. José-Yacamán, L. Rendón, J. Arenas, M.C.S. Puche, Maya blue paint: An ancient nanostructured material, Science 273 (1996), 223-225. http://dx.doi.org/10.1126/science.273.5272.223

2   G. Chiari, R. Giustetto, J. Druzik, E. Doehne, G. Ricchiardi, Pre-columbian nanotechnology: reconciling the mysteries of the maya blue pigment, Appl. Phys. A 90 (2008), 3-7. http://dx.doi.org/10.1007/s00339-007-4287-z

3   M. Reibold, P. Paufler, A.A. Levin, W. Kochmann, N. Pätzke, D.C. Meyer, Carbon nanotubes in an ancient Damascus sabre, Nature 444 (2006), 286. http://dx.doi.org/10.1038/444286a

4   M. Reibold, P. Paufler, A.A. Levin, W. Kochmann, N. Pätzke, D.C. Meyer, Discovery of nanotubes in ancient Damascus steel, in: D.T. Cat, A. Pucci, K. Wandelt (Eds.), Physics and Engineering of New Materials, Springer Proceedings in Physics Vol. 127, Springer, Berlin, 2009, pp. 305-310. http://dx.doi.org/10.1007/978-3-540-88201-5_35

5   H. Gleiter, Nanocrystalline materials, Prog. Mater. Sci. 33 (1989), 223-315. http://dx.doi.org/10.1016/0079-6425(89)90001-7

6   H. Gleiter, Materials with ultra-fine grain sizes, in: N. Hansen, T. Leffers, H. Lilholt (Eds.), Proceedings of the Second Risø International Symposium on Metallurgy and Materials Science, Roskilde, 1981, pp. 15-22.

7   E.O. Hall, The deformation and ageing of mild steel, Proc. Phys. Soc. B 64 (1951), 747-753. http://dx.doi.org/10.1088/0370-1301/64/9/303

8   N.J. Petch, The cleavage strength of polycrystals, J. Iron Steel Inst. 174 (1953), 25-28.

9   E. Arzt, Size effects in materials due to microstructural and dimensional constraints: A comparative review, Acta Mater. 46 (1998), 5611-5626. http://dx.doi.org/10.1016/S1359-6454(98)00231-6

10 C.S. Pande, K.P. Cooper, Nanomechanics of Hall-Petch relationship in nanocrystalline materials, Prog. Mater. Sci. 54 (2009), 689-706. http://dx.doi.org/10.1016/j.pmatsci.2009.03.008

11 T.G. Nieh, J. Wadsworth, Hall-Petch relation in nanocrystalline solids, Scr. Metall. Mater. 25 (1991), 955-958. http://dx.doi.org/10.1016/0956-716X(91)90256-Z

12 Y.T. Zhu, B.Q. Han, E.J. Lavernia, Deformation mechanisms of nanostructured materials, in: M.J. Zehetbauer, Y.T. Zhu (Eds.), Bulk Nanostructured Materials, Wiley-VCH, Weinheim, 2009, pp. 89-108. http://dx.doi.org/10.1002/9783527626892.ch4

13 H. Gleiter, Nanostructured materials: Basic concepts and microstructure, Acta Mater. 48 (2000), 1-29. http://dx.doi.org/10.1016/S1359-6454(99)00285-2

14 International Organization for Standardization, ISO/TS 80004-4:2011 Nanotechnologies – Vocabulary – Part 4: Nanostructured materials, 2011.

15 Yu.D. Gamburg, G. Zangari, Theory and Practice of Metal Electrodeposition, Springer, New York, 2011. http://dx.doi.org/10.1007/978-1-4419-9669-5

16 N. Tsuji, Y. Saito, S.-H. Lee, Y. Minamino, ARB (accumulative roll-bonding) and other new techniques to produce bulk ultrafine grained materials, Adv. Eng. Mater. 5 (2003), 338-344. http://dx.doi.org/10.1002/adem.200310077

17 C.C. Koch, Nanostructured materials: An overview, in: M.J. Zehetbauer, Y.T. Zhu (Eds.), Bulk Nanostructured Materials, Wiley-VCH, Weinheim, 2009, pp. 3-20. http://dx.doi.org/10.1002/9783527626892.ch1

18 R.Z. Valiev, R.K. Islamgaliev, I.V. Alexandrov, Bulk nanostructured materials from severe plastic deformation, Prog. Mater. Sci. 45 (2000), 103-189. http://dx.doi.org/10.1016/S0079-6425(99)00007-9

19 C.C. Koch, Top-down synthesis of nanostructured materials: Mechanical and thermal processing methods, Rev. Adv. Mater. Sci. 5 (2003), 91-99.

20 Y. Ivanisenko, A. Darbandi, S. Dasgupta, R. Kruk, H. Hahn, Bulk nanostructured materials: Non-mechanical synthesis, Adv. Eng. Mater. 12 (2010), 666-676. http://dx.doi.org/10.1002/adem.201000131

21 R. Pippan, F. Wetscher, M. Hafok, A. Vorhauer, I. Sabirov, The limits of refinement by severe plastic deformation, Adv. Eng. Mater. 8 (2006), 1046-1056. http://dx.doi.org/10.1002/adem.200600133

22 P.W. Bridgman, On torsion combined with compression, J. Appl. Phys. 14 (1943), 273-283. http://dx.doi.org/10.1063/1.1714987

23 R. Pippan, High-pressure torsion: Features and applications, in: M.J. Zehetbauer, Y.T. Zhu (Eds.), Bulk Nanostructured Materials, Wiley-VCH, Weinheim, 2009, pp. 217-233. http://dx.doi.org/10.1002/9783527626892.ch9

24 P.W. Bridgman, Effects of high shearing stress combined with high hydrostatic pressure, Phys. Rev. 15 (1935), 825-847. http://dx.doi.org/10.1103/PhysRev.48.825

25 R.Z. Valiev, O.A. Kuznetsov, R.I. Kaibyshev, R.S. Musalimov, N.K. Tsenev, Low-temperature superplasticity of metallic materials, Dokl. Akad. Nauk SSSR 301 (1988), 864-866.

26 R.Z. Valiev, R.R. Mulyukov, W. Ovchinnikov, Direction of a grain-boundary phase in submicrometer-grained iron, Philos. Mag. Lett. 62 (1990), 253-256. http://dx.doi.org/10.1080/09500839008215131

27 A. Hohenwarter, A. Bachmaier, B. Gludovatz, S. Scheriau, R. Pippan, Technical parameters affecting grain refinement by high pressure torsion, Int. J. Mat. Res. 100 (2009), 1653-1661. http://dx.doi.org/10.3139/146.110224

28 H.T. Hall, Ultra-high-pressure, high-temperature apparatus: the "Belt", Rev. Sci. Instrum. 31 (1960), 125-131. http://dx.doi.org/10.1063/1.1716907

29 R. Wadsack, R. Pippan, B. Schedler, Structural refinement of chromium by severe plastic deformation, Fusion Eng. Des. 66-68 (2003), 265-269. http://dx.doi.org/10.1016/S0920-3796(03)00136-4

30 K. Edalati, Z. Horita, A review on high-pressure torsion (HPT) from 1935 to 1988, Mater. Sci. Eng. A 652 (2016), 325-352. http://dx.doi.org/10.1016/j.msea.2015.11.074

31 C.C. Koch, The synthesis and structure of nanocrystalline materials produced by mechanical attrition: A review, Nanostruct. Mater. 2 (1993), 109-129. http://dx.doi.org/10.1016/0965-9773(93)90016-5

32 R. Pippan, S. Scheriau, A. Taylor, M. Hafok, A. Hohenwarter, A. Bachmaier, Saturation of fragmentation during severe plastic deformation, Annu. Rev. Mater. Res. 40 (2010), 19-43. http://dx.doi.org/10.1146/annurev-matsci-070909-104445

33 M. Hafok, R. Pippan, High-pressure torsion applied to nickel single crystals, Philos. Mag. 88 (2008), 1857-1877. http://dx.doi.org/10.1080/14786430802337071

34 B. Yang, H. Vehoff, A. Hohenwarter, M. Hafok, R. Pippan, Strain effects on the coarsening and softening of electrodeposited nanocrystalline Ni subjected to high pressure torsion, Scr. Mater. 58 (2008), 790-793. http://dx.doi.org/10.1016/j.scriptamat.2007.12.039

35 D.J. Lee, H.S. Kim, Finite element analysis for the geometry effect on strain inhomogeneity during high-pressure torsion, J. Mater. Sci. 49 (2014), 6620-6628. http://dx.doi.org/10.1007/s10853-014-8283-3

36 K.S. Kormout, P. Ghosh, V. Maier-Kienter, R. Pippan, Deformation mechanisms during severe plastic deformation of a Cu-Ag composite, J. Alloys Compd. 695 (2017), 2285-2294. http://dx.doi.org/10.1016/j.jallcom.2016.11.085

37 F. Wetscher, R. Pippan, Cyclic high-pressure torsion of nickel and Armco iron, Philos. Mag. 86 (2006), 5867-5883. http://dx.doi.org/10.1080/14786430600838288

38 K. Edalati, Z. Horita, Continuous high-pressure torsion, J. Mater. Sci. 45 (2010), 4578-4582. http://dx.doi.org/10.1007/s10853-010-4381-z

39 M. Jahedi, M. Knezevic, M.H. Paydar, High-pressure double torsion as a severe plastic deformation process: Experimental procedure and finite element modeling, J. Mater. Eng. Perform. 24 (2015), 1471-1482. http://dx.doi.org/10.1007/s11665-015-1426-0

40 A. Hohenwarter, Incremental high pressure torsion as a novel severe plastic deformation process: Processing features and application to copper, Mater. Sci. Eng. A 626 (2015), 80-85. http://dx.doi.org/10.1016/j.msea.2014.12.041

41 A. Hohenwarter, R. Pippan, Introduction of planar high pressure torsion (P-HPT) for fabrication of nanostructured sheets, Adv. Eng. Mater. (2018). http://dx.doi.org/10.1002/adem.201800050

42 J.W. Shin, A. Standley, E. Chason, Epitaxial electrodeposition of freestanding large area single crystal substrates, Appl. Phys. Lett. 90 (2007), 261909. http://dx.doi.org/10.1063/1.2752531

43 U. Erb, G. Palumbo, J.L. McCrea, The processing of bulk nanocrystalline metals and alloys by electrodeposition, in: S.H. Whang (Ed.), Nanostructured Metals and Alloys: Processing, Microstructure, Mechanical Properties and Applications, Woodhead Publishing, Cambridge, 2011, pp. 118-151. http://dx.doi.org/10.1533/9780857091123.1.118

44 F. Nasirpouri, Electrodeposition of Nanostructured Materials, Springer Series in Surface Sciences Vol. 62, Springer, Cham, 2017. http://dx.doi.org/10.1007/978-3-319-44920-3

45 U. Dehlinger, F. Giesen, Über den Zusammenhang zwischen regelmäßiger Atomverteilung und Resistenzgrenzen, Z. Metallkd. 24 (1932), 197-198.

46 C.H. Hamann, W. Vielstich, Elektrochemie, 4th edition, Wiley-VCH, Weinheim, 2005.

47 E. Gileadi, Physical Electrochemistry: Fundamentals, Techniques and Applications, Wiley-VCH, Weinheim, 2011. http://dx.doi.org/10.1002/anie.201104618

48 W. Nernst, Theory of reaction velocities in heterogeneous systems, Z. Phys. Chem. 47 (1904), 52-55.

49 R. Parsons, Electrical double layer: Recent experimental and theoretical developments, Chem. Rev. 90 (1990), 813-826. http://dx.doi.org/10.1021/cr00103a008

50 H. Fischer, Electrocrystallization of metals under ideal and real conditions, Angew. Chem. internat. Edit. 8 (1969), 108-119. http://dx.doi.org/10.1002/anie.196901081

51 E. Budevski, G. Staikov, W.J. Lorenz, Electrocrystallization – Nucleation and growth phenomena, Electrochim. Acta 45 (2000), 2559-2574. http://dx.doi.org/10.1016/S0013-4686(00)00353-4

52 H. Fischer, Elektrolytische Abscheidung und Elektrokristallisation von Metallen, Springer, Berlin, 1954. http://dx.doi.org/10.1007/978-3-642-86549-7

53 Yu.D. Gamburg, Development of the electrocrystallization theory, Russ. J. Electrochem. 52 (2016), 832-846. http://dx.doi.org/10.1134/S1023193516090032

54 M. Izaki, Electrodeposition of iron and iron alloys, in: M.. Schlesinger, M. Paunovic (Eds.), Modern Electroplating, 5th edition, John Wiley & Sons, Inc., Hoboken, 2010, pp. 79-114. http://dx.doi.org/10.1002/9780470602638.ch11

55 W.E.G. Hansal, S. Roy, Pulse-Plating, Leuze, Bad Saulgau, 2012.

56   D.R. Gabe, The role of hydrogen in metal electrodeposition processes, J. Appl. Electrochem. 27 (1997), 908-915. http://dx.doi.org/10.1023/A:1018497401365

57   U. Erb, K.T. Aust, G. Palumbo, Electrodeposited nanocrystalline metals, alloys, and composites, in: C. Koch (Ed.), Nanostructured Materials: Processing, Properties, and Applications, 2nd edition, William Andrew Inc, Norwich, 2007, pp. 235-292. http://dx.doi.org/10.1016/B978-081551534-0.50008-7

58   I. Gurrappa, L. Binder, Electrodeposition of nanostructured coatings and their characterization – a review, Sci. Technol. Adv. Mater. 9 (2008), 043001. http://dx.doi.org/10.1088/1468-6996/9/4/043001

59   K. Schüler, B. Philippi, M. Weinmann, V.M. Marx, H. Vehoff, Effects of processing on texture, internal stresses and mechanical properties during the pulsed electrodeposition of nanocrystalline and ultrafine-grained nickel, Acta Mater. 61 (2013), 3945-3955. http://dx.doi.org/10.1016/j.actamat.2013.03.008

60   D. Rathmann, M. Marx, C. Motz, Crack propagation and mechanical properties of electrodeposited nickel with bimodal microstructures in the nanocrystalline and ultrafine grained regime, J. Mater. Res. 32 (2017), 4573-4582. http://dx.doi.org/10.1557/jmr.2017.353

61   M. Baricco, P. Palumbo, D. Baldissin, E. Bosco, L. Battezzati, Metastable phases and phase diagrams, Metall. Ital. 11-12 (2004) 1-8.

62   H. Okamoto, The C-Fe (carbon-iron) system, J. Phase Equilib. 13 (1992), 543-565. http://dx.doi.org/10.1007/BF02665767

63   U. Herr, Phase stability in nanostructures, Adv. Eng. Mater. 3 (2001), 889-893. http://dx.doi.org/10.1002/1527-2648(200111)3:11<889::AID-ADEM889>3.0.CO;2-9

64   A. Bachmaier, M. Pfaff, M. Stolpe, H. Aboulfadl, C. Motz, Phase separation of a supersaturated nanocrystalline Cu-Co alloy and its influence on thermal stability, Acta Mater. 96 (2015), 269-283. http://dx.doi.org/10.1016/j.actamat.2015.05.053

65   C. Suryanarayana, Mechanical alloying and milling, Prog. Mater. Sci. 46 (2001), 1-184. http://dx.doi.org/10.1016/S0079-6425(99)00010-9

66   V.V. Povetkin, T.E. Ivanova, A.V. Ismagilova, Structure and properties of electrolytic copper alloys with low-melting metals, Int. J. Appl. Eng. Res. 12 (2017), 5416-5420.

67   E. Raub, The 16th William Blum Lecture: Theoretical and Practical Aspects of Alloy Plating Part 1, Plating & Surface Finishing 63 (1976), 29-37.

68   A.R. Yavari, P.J. Desré, T. Benaumeur, Mechanically driven alloying of immiscible elements, Phys. Rev. Lett. 68 (1992), 2235-2238. http://dx.doi.org/10.1103/PhysRevLett.68.2235

69   J. Eckert, J.C. Holzer, C.E. Krill III, W.L. Johnson, Mechanically driven alloying and grain size changes in nanocrystalline Fe-Cu powders, J. Appl. Phys. 73 (1993), 2794-2802. http://dx.doi.org/10.1063/1.353055

70   J.Z. Jiang, C. Gente, R. Bormann, Mechanical alloying in the Fe-Cu system, Mater. Sci. Eng. A 242 (1998), 268-277. http://dx.doi.org/10.1016/S0921-5093(97)00522-4

71   M. Angiolini, F. Cardellini, M. Krasnowski, G. Mazzone, A. Montone, M. Vittori-Antisari, Electron microscopy investigation on the effect of plastic deformation in the alloying of the immiscible system Cu-Fe, Microsc. Microanal. Microstruct. 6 (1995), 601-609. http://dx.doi.org/10.1051/mmm:1995150

72   G. Mazzone, M. Vittori-Antisari, Structural and magnetic properties of metastable fcc Cu-Fe alloys, Phys. Rev. B 54 (1996), 441-446. http://dx.doi.org/10.1103/PhysRevB.54.441

73   M. Angiolini, G. Mazzone, A. Montone, M. Vittori-Antisari, Mechanical alloying in immiscible systems, Mater. Sci. Forum 235-238 (1997), 175-180. http://dx.doi.org/10.4028/www.scientific.net/MSF.235-238.175

74   A.R. Yavari, P.J. Desre, Mechanical alloying of immiscible elements, in: A.R. Yavari (Ed.), Ordering and Disordering in Alloys, Elsevier, Barking, 1992, pp. 414-422. http://dx.doi.org/10.4028/10.1007/978-94-011-2886-5_43

75   A.R. Yavari, Phase transformations in nanocrystalline alloys, Mater. Sci. Eng. A 179 (1994), 20-26. http://dx.doi.org/10.1016/0921-5093(94)90157-0

76   R. Yavari, O. Drbohlav, A. Hernando, P. Crespo, A. Garcia Escorial, J.M. Barandiaran, I. Orue, Metastable phase formation and decomposition in nanomixtures of immiscible Cu and Fe, Mater. Sci. Forum 155-156 (1994), 463-474. http://dx.doi.org/10.4028/www.scientific.net/MSF.155-156.463

77   P. Bellon, R.S. Averback, Nonequilibrium roughening of interfaces in crystals under shear: Application to ball milling, Phys. Rev. Lett. 74 (1995), 1819-1822. http://dx.doi.org/10.1103/PhysRevLett.74.1819

78   D. Raabe, S. Ohsaki, K. Hono, Mechanical alloying and amorphization in Cu–Nb–Ag in situ composite wires studied by transmission electron microscopy and atom probe tomography, Acta Mater. 57 (2009), 5254-5263. http://dx.doi.org/10.1016/j.actamat.2009.07.028

79   K.S. Kormout, R. Pippan, A. Bachmaier, Deformation-induced supersaturation in immiscible material systems during high-pressure torsion, Adv. Eng. Mater. 19 (2017), 1600675. http://dx.doi.org/10.1002/adem.201600675

80   Y. Ueda, N. Kikuchi, Structure and magnetic properties of electrodeposited Fe-Cu alloy films, Jpn. J. Appl. Phys. 32 (1993), 1779-1782. http://dx.doi.org/10.1143/JJAP.32.1779

81   A.E. Mohamed, S.M. Rashwan, S.M. Abdel-Wahaab, M.M. Kamel, Electrodeposition of Co–Cu alloy coatings from glycinate baths, J. Appl. Electrochem. 33 (2003), 1085-1092. http://dx.doi.org/10.1023/A:1026209715687

82   R. Bernasconi, J.L. Hart, A.C. Lang, L. Magagnin, L. Nobili, M.L. Taheri, Structural properties of electrodeposited Cu-Ag alloys, Electrochim. Acta 251 (2017), 475-481. http://dx.doi.org/10.1016/j.electacta.2017.08.097

83   A. Hohenwarter, A. Taylor, R. Stock, R. Pippan, Effect of large shear deformations on the fracture behavior of a fully pearlitic steel, Metall. Mater. Trans. A 42 (2011), 1609-1618. http://dx.doi.org/10.1007/s11661-010-0541-7

84   R. Pippan, A. Hohenwarter, The importance of fracture toughness in ultrafine and nanocrystalline bulk materials, Mater. Res. Lett. 4 (2016), 127-136. http://dx.doi.org/10.1080/21663831.2016.1166403

85   T. Leitner, G. Trummer, R. Pippan, A. Hohenwarter, Influence of severe plastic deformation and specimen orientation on the fatigue crack propagation behavior of a pearlitic steel, Mater. Sci. Eng. A 710 (2018), 260-270. http://dx.doi.org/10.1016/j.msea.2017.10.040

86   W. Blum, The structure and properties of alternately electrodeposited metals, Trans. Am. Electrochem. Soc. 40 (1921), 307-320.

87   C.A. Ross, Electrodeposited multilayer thin films, Annu. Rev. Mater. Sci. 24 (1994), 159-188. http://dx.doi.org/10.1146/annurev.ms.24.080194.001111

88   L. Péter, I. Bakonyi, Electrodeposition and properties of nanoscale magnetic/non-magnetic metallic multilayer films, in: G. Staikov (Ed.), Electrocrystallization in Nanotechnology, Wiley-VCH, Weinheim, 2007, pp. 242-260. http://dx.doi.org/10.1002/9783527610198.ch12

89   J.M. Rosalie, P. Ghosh, J. Guo, O. Renk, Z. Zhang, Microstructural and texture evolution of copper-(chromium, molybdenum, tungsten) composites deformed by high-pressure-torsion, submitted (2018). https://arxiv.org/abs/1801.09989v1

90   R. Kulagin, Y. Beygelzimer, Y. Ivanisenko, A. Mazilkin, H. Hahn, High pressure torsion: from laminar flow to turbulance, IOP Conf. Ser.: Mater. Sci. Eng. 194 (2017), 012045. http://dx.doi.org/10.1088/1757-899X/194/1/012045

91 P. Ghosh, K.S. Kormout, J. Todt, U. Lienert, J. Keckes, R. Pippan, An investigation on shear banding and crystallographic texture of Ag-Cu alloys deformed by high-pressure torsion, Proc. Inst. Mech. Eng. Part C (2018). http://dx.doi.org/10.1177/0954406218761508

92 A. Bachmaier, J. Schmauch, H. Aboulfadl, A. Verch, C. Motz, On the process of co-deformation and phase dissolution in a hard-soft immiscible Cu-Co alloy system during high-pressure torsion deformation, Acta Mater. 115 (2016), 333-346. http://dx.doi.org/10.1016/j.actamat.2016.06.010

93 Y. Li, D. Raabe, M. Herbig, P.-P. Choi, S. Goto, A. Kostka, H. Yarita, C. Borchers, R. Kirchheim, Segregation stabilizes nanocrystalline bulk steel with near theoretical strength, Phys. Rev. Lett. 113 (2014), 106104. http://dx.doi.org/10.1103/PhysRevLett.113.106104

94 A. Vorhauer, R. Pippan, On the onset of a steady state in body-centered cubic iron during severe plastic deformation at low homologous temperatures, Metall. Mater. Trans. A 39 (2008), 417-429. http://dx.doi.org/10.1007/s11661-007-9413-1

95 O. Renk, P. Ghosh, R. Pippan, Generation of extreme grain aspect ratios in severely deformed tantalum at elevated temperatures, Scr. Mater. 137 (2017), 60-63. http://dx.doi.org/10.1016/j.scriptamat.2017.04.024

96 C. Wagner, Point defects and their interaction, Ann. Rev. Mater. Sci. 7 (1977), 1-22. http://dx.doi.org/10.1146/annurev.ms.07.080177.000245

97 W.R. Thomas, G.M. Leak, Condition of boron in alpha iron, Nature 176 (1955), 29-31. http://dx.doi.org/10.1038/176029b0

98 D.H.R. Fors, G. Wahnström, Nature of boron solution and diffusion in α-iron, Phys. Rev. B 77 (2008), 132102. http://dx.doi.org/10.1103/PhysRevB.77.132102

99 H.K.D.H. Bhadeshia, R. Honeycombe, Steels: Microstructure and Properties, 3rd edition, Butterworth-Heinemann, Oxford, 2006, pp. 1-16. http://dx.doi.org/10.1016/B978-075068084-4/50003-0

100 W. Hume-Rothery, H.M. Powell, On the theory of super-lattice structures in alloys, Z. Kristallogr. 91 (1935), 23-47. http://dx.doi.org/10.1524/zkri.1935.91.1.23

101 C.A. Wert, Diffusion coefficient of C in α-iron, Phys. Rev. 79 (1950), 601-605. http://dx.doi.org/10.1103/PhysRev.79.601

102 M. Aucouturier, Grain boundary segregations and hydrogen embrittlement, J. Phys. Colloq. 43 (1982), C6-175-C6-186. http://dx.doi.org/10.1051/jphyscol:1982617

103 D. Eliezer, E. Tal-Gutelmacher, Th. Boellinghaus, Hydrogen embrittlement in hydride- and non hydride-forming systems – Microstructural/phase changes and cracking mechanisms, EUROCORR 2005 Proceedings, 2005.

104 Yu. N. Bekish, S.S. Grabchikov, L.S. Tsybul'skaya, V.A. Kukareko, S.S. Perevoznikov, Electroplated cobalt-boron alloys: Formation and structure features, Prot. Met. Phys. Chem. Surf. 49 (2013), 319-324. http://dx.doi.org/10.1134/S2070205113030040

105 M. Onoda, K. Shimizu, T. Tsuchiya, T. Watanabe, Preparation of amorphous/crystalloid soft magnetic multilayer Ni-Co-B alloy films by electrodeposition, J. Magn. Magn. Mater. 126 (1993), 595-598. http://dx.doi.org/10.1016/0304-8853(93)90697-Z

106 C.-R. Chang, K.-H. Hou, M.-D. Ger, J.-R. Wang, Characteristics of nickel boron coatings prepared by direct current electrodeposition technique, Int. J. Electrochem. Sci. 12 (2017), 2055-2069. http://dx.doi.org/10.20964/2017.03.17

107 A. Brenner, Electrodeposition of Alloys: Principles and Practice Vol. II, Academic Press, New York, 1963, pp. 457-483. http://dx.doi.org/10.1016/B978-1-4831-9807-1.50026-X

108 A.M. Tarasov, Effect of boron on embrittlement of constructional steel during tempering, Met. Sci. Heat Treat. 1 (1959), 57-60. http://dx.doi.org/10.1007/BF01167420

109 J.J. Rice, J.-S. Wang, Embrittlement of interfaces by solute segregation, Mater. Sci. Eng. A 107 (1989), 23-40. http://dx.doi.org/10.1016/0921-5093(89)90372-9

110 G.L. Krakso, G.B. Olson, Effect of boron, carbon, phosphorus and sulphur on intergranular cohesion in iron, Solid State Commun. 76 (1990), 247-251. http://dx.doi.org/10.1016/0038-1098(90)90832-V

111 R.V. Sundeev, A.M. Glezer, A.P. Menushenkov, A.V. Shalimova, O.V. Chernysheva, N.V. Umnova, Effect of high pressure torsion at different temperatures on the local atomic structure of amorphous Fe-Ni-B alloys, Mater. Des. 135 (2017), 77-83. http://dx.doi.org/10.1016/j.matdes.2017.08.062

112 Yu. Ivanisenko, W. Lojkowski, R.Z. Valiev, H.-J. Fecht, The mechanism of formation of nanostructure and dissolution of cementite in a pearlitic steel during high pressure torsion, Acta Mater. 51 (2003), 5555-5570. http://dx.doi.org/10.1016/S1359-6454(03)00419-1

113 Yu. Ivanisenko, I. MacLaren, X. Sauvage, R.Z. Valiev, H.-J. Fecht, Shear-induced $\alpha \rightarrow \gamma$ transformation in nanoscale Fe-C composite, Acta Mater. 54 (2006), 1659-1669. http://dx.doi.org/10.1016/j.actamat.2005.11.034

114 F. Wetscher, R. Pippan, S. Sturm, F. Kauffmann, C. Scheu, G. Dehm, TEM investigations of the structural evolution in a pearlitic steel deformed by high-pressure torsion, Metall. Mater. Trans. A 37 (2006), 1963-1968. http://dx.doi.org/10.1007/s11661-006-0138-3

115 X. Sauvage, Y. Ivanisenko, The role of carbon segregation on nanocrystallisation of pearlitic steels processed by severe plastic deformation, J. Mater. Sci. 42 (2007), 1615-1621. http://dx.doi.org/10.1007/s10853-006-0750-z

116 A.R. Waugh, S. Paetke, D.V. Edmonds, A study of segregation to the dislocation substructure in patented steel wire using atom-probe techniques, Metallography 14 (1981), 237-251. http://dx.doi.org/10.1016/0026-0800(81)90029-X

117 J. Languillaume, G. Kapelski, B. Baudelet, Cementite dissolution in heavily cold drawn pearlitic steel wires, Acta Mater. 45 (1997), 1201-1212. http://dx.doi.org/10.1016/S1359-6454(96)00216-9

118 H.G. Read, W.T. Reynolds Jr., K. Hono, T. Tarui, APFIM and TEM studies of drawn pearlitic wire, Scr. Mater. 37 (1997), 1221-1230. http://dx.doi.org/10.1016/S1359-6462(97)00223-6

119 F. Danoix, D. Julien, X. Sauvage, J. Copreaux, Direct evidence of cementite dissolution in drawn pearlitic steels observed by tomographic atom probe, Mater. Sci. Eng. A 250 (1998), 8-13. http://dx.doi.org/10.1016/S0921-5093(98)00529-2

120 W.J. Nam, C.M. Bae, S.J. Oh, S.-J. Kwon, Effect of interlamellar spacing on cementite dissolution during wire drawing of pearlitic steel wires, Scr. Mater. 42 (2000), 457-463. http://dx.doi.org/10.1016/S1359-6462(99)00372-3

121 K. Hono, M. Ohnuma, M. Murayama, S. Nishida, A. Yoshie, T. Takahashi, Cementite decomposition in heavily drawn pearlitic steel wire, Scr. Mater. 44 (2001), 977-983. http://dx.doi.org/10.1016/S1359-6462(00)00690-4

122 G.B. Rathmayr, R. Pippan, Influence of impurities and deformation temperature on the saturation microstructure and ductility of HPT-deformed nickel, Acta Mater. 59 (2011), 7228-7240. http://dx.doi.org/10.1016/j.actamat.2011.08.023

123 A. Bachmaier, C. Motz, On the remarkable thermal stability of nanocrystalline cobalt via alloying, Mater. Sci. Eng. A 624 (2015), 41-51. http://dx.doi.org/10.1016/j.msea.2014.11.062

124 S.O. Rogachev, S.A. Nikulin, V.M. Khatkevich, Structural and phase transformations in internally nitrided corrosion-resistant steel during severe plastic deformation and subsequent annealings, Steel Res. Int. 88 (2017), 1700070. http://dx.doi.org/10.1002/srin.201700070

125 J.E. Mittemeijer, M.A.J. Somers, Kinetics of thermochemical surface treatments, in: J.E. Mittemeijer, M.A.J. Somers (Eds.), Thermochemical Surface Engineering of Steels, Woodhead Publishing, Cambridge, 2015. http://dx.doi.org/10.1533/9780857096524.1.113

126 L. Zhang, B.G. Thomas, X. Wang, K. Cai, Evaluation and control of steel cleanliness – Review, Steelmaking Conf. Proc. 85 (2002), 431-452.

127 W.C. Johnson, J.E. Doherty, B.H. Kear, A.F. Giamei, Confirmation of sulfur embrittlement in nickel alloys, Scr. Metall. 8 (1974), 971-974. http://dx.doi.org/10.1016/0036-9748(74)90394-9

128 D.J. Allen, D.A. Wolstenholme, Sulphur segregation and intergranular microcracking in ferritic steel weld metal, Met. Technol. 9 (1982), 266-273. http://dx.doi.org/10.1179/030716982803285800

129 D.A. Woodford, R.H. Bricknell, Environmental embrittlement of high temperature alloys by oxygen, Treatise Mater. Sci. Technol. 25 (1983), 157-199. http://dx.doi.org/10.1016/B978-0-12-341825-8.50011-8

130 A. Bachmaier, A. Hohenwarter, R. Pippan, New procedure to generate stable nanocrystallites by severe plastic deformation, Scr. Mater. 61 (2009), 1016-1019. http://dx.doi.org/10.1016/j.scriptamat.2009.08.016

131 J. George, J. Rantschler, S.-E. Bae, D. Litvinov, S.R. Brankovic, Sulfur and saccharin incorporation into electrodeposited CoFe alloys: Consequences for magnetic and corrosion properties, J. Electrochem. Soc. 155 (2008), D589-D594. http://dx.doi.org/10.1149/1.2948377

132 G.A. Di Bari, Electrodeposition of nickel, in: M.. Schlesinger, M. Paunovic (Eds.), Modern Electroplating, 5th edition, John Wiley & Sons, Inc., Hoboken, 2010, pp. 79-114. http://dx.doi.org/10.1002/9780470602638.ch3

133 B. Philippi, Gezielte Variation der Mikrostruktur bei der gepulsten Elektrodeposition von nanokristallinem und ultrafeinkörnigem Nickel, diploma thesis, Saarland University, 2011.

134 G.B. Rathmayr, A. Bachmaier, R. Pippan, Development of a new testing procedure for performing tensile tests on speciments with sub-millimetre dimensions, J. Test. Eval. 41 (2013), 635-646. http://dx.doi.org/10.1520/JTE20120175

135 A. Bachmaier, M. Kerber, D. Setman, R. Pippan, The formation of supersaturated solid solutions in Fe–Cu alloys deformed by high-pressure torsion, Acta Mater. 60 (2012), 860-871. http://dx.doi.org/10.1016/j.actamat.2011.10.044

136 A. Bachmaier, R. Pippan, Generation of metallic nanocomposites by severe plastic deformation, Int. Mater. Rev. 58 (2013), 41-62. http://dx.doi.org/10.1179/1743280412Y.0000000003

137 A. Bachmaier, J. Keckes, K.S. Kormout, R. Pippan, Supersaturation in Ag–Ni alloy by two-step high-pressure torsion processing, Philos. Mag. Lett. 94 (2014), 9-17. http://dx.doi.org/10.1080/09500839.2013.852284

138 A. Bachmaier, E. Neubauer, M. Kitzmantel, R. Pippan, C. Motz, Microstructural evolution in immiscible alloys processed by high-pressure torsion,   IOP Conf. Ser.: Mater. Sci. Eng. 63 (2014), 012023. http://dx.doi.org/10.1088/1757-899X/63/1/012023

139 K.S. Kormout, B. Yang, R. Pippan, Transmission electron microscope investigations on Cu-Ag alloys produced by high-pressure torsion, IOP Conf. Ser.: Mater. Sci. Eng. 63 (2014), 012092. http://dx.doi.org/10.1088/1757-899X/63/1/012092

140 L. Krämer, S. Wurster, R. Pippan, Deformation behavior of Cu-composites processed by HPT, IOP Conf. Ser.: Mater. Sci. Eng. 63 (2014), 012026. http://dx.doi.org/10.1088/1757-899X/63/1/012026

141 L. Krämer, K.S. Kormout, D. Setman, Y. Champion, R. Pippan, Production of bulk metallic glasses by severe plastic deformation, Metals 2 (2015), 720-729. http://dx.doi.org/10.3390/met5020720

142 L. Krämer, Y. Champion, R. Pippan, From powders to bulk metallic glass composites, Sci. Rep. 7 (2017), 6651. http://dx.doi.org/10.1038/s41598-017-06424-4

143 F. Thümmler, R. Oberacker, Introduction to Powder Metallurgy, The Institute of Materials Series on Powder Metallurgy, London, 1993, p. 113.

144 M.S. Herrmann, An easy-to-do plating experiment, J. Chem. Educ. 69 (1992), 60-61. http://dx.doi.org/10.1021/ed069p60

145 A. Turoňová, M. Gálová, M. Gernátová, Study of electroless copper deposition on Fe powder, Part. Sci. Technol. 26 (2008), 126-135. http://dx.doi.org/10.1080/02726350701483842

146 W.D. Callister Jr., Materials Science and Engineering: An Introduction, 7th edition, John Wiley & Sons Inc., New York, 2007, p. 331.

147 G. Gottstein, Physikalische Grundlagen der Materialkunde, 3rd edition, Springer, Berlin, 2007, p. 416. http://dx.doi.org/10.1007/978-3-540-71105-6

148 E.J. Mittemeijer, Fundamentals of Materials Science: The Microstructure-Property Relationship Using Metals as Model Systems, Springer, Berlin, 2011, p. 404. http://dx.doi.org/10.1007/978-3-642-10500-5

149 D. Kalish, E.M. Roberts, On the distribution of carbon in martensite, Metall. Trans. 2 (1971), 2783-2790. http://dx.doi.org/10.1007/BF02813252

150 G. Krauss, Martensite in steel: strength and structure, Mater. Sci. Eng. A 273-275 (1999), 40-57. http://dx.doi.org/10.1016/S0921-5093(99)00288-9

151 B. Hutchinson, J. Hagström, O. Karlsson, D. Lindell, M. Tornberg, F. Lindberg, M. Thuvander, Acta Mater. 59 (2011), 5845-5858. http://dx.doi.org/10.1016/j.actamat.2011.05.061

152 M.W. Kapp, A. Hohenwarter, S. Wurster, B. Yang, R. Pippan, Anisotropic deformation characteristics of an ultrafine- and nanolamellar pearlitic steel, Acta Mater. 106 (2016), 239-248. http://dx.doi.org/10.1016/j.actamat.2015.12.037

153 I. Tkalcec, Mechanical Properties and Microstructure of a High Carbon Steel, PhD thesis, University of Zagreb, 2004.

154 C.L. Magee, R.G. Davies, The structure, deformation and strength of ferrous martensites, Acta Metall. 19 (1971), 345-354. http://dx.doi.org/10.1016/0001-6160(71)90102-7

155 R. Hossain, F. Pahlevani, M.Z. Quadir, V. Sahajwalla, Stability of retained austenite in high carbon steel under compressive stress: an investigation from macro to nano scale, Sci. Rep. 6 (2016), 34958. http://dx.doi.org/10.1038/srep34958

156 N. Schell, A. King, F. Beckmann, T. Fischer, M. Müller, A. Schreyer, The high energy materials science beamline (HEMS) at PETRA III, Mater. Sci. Forum 772 (2014) 57-61. http://dx.doi.org/10.4028/www.scientific.net/MSF.772.57

157 M. Faleschini, H. Kreuzer, D. Kiener, R. Pippan, Fracture toughness investigations of tungsten alloys and SPD tungsten alloys, J. Nucl. Mater. 367-370 (2007), 800-805. http://dx.doi.org/10.1016/j.jnucmat.2007.03.079

158 M. Mito, H. Matsui, K. Tsuruta, T. Yamaguchi, K. Nakamura, H. Deguchi, N. Shirakawa, H. Adachi, T. Yamasaki, H. Iwaoka, Y. Ikoma, Z. Horita, Large enhancement of superconducting transition temperature in single-element superconducting rhenium by shear strain, Sci. Rep. 6 (2016), 36337. http://dx.doi.org/10.1038/srep36337

159 Y. Song, W. Wang, D. Gao, E.Y. Yoon, D.J. Lee, H.S. Kim, Finite element analysis of the effect of friction in high pressure torsion, Met. Mater. Int. 20 (2014), 445-450. http://dx.doi.org/10.1007/s12540-014-3007-4

160 Y. Song, M. Chen, B. Xu, D. Gao, J. Gao, L. Xu, Z. Wang, H.S. Kim, Effects of friction and anvil design on plastic deformation during the compression stage of high-pressure torsion, Korean J. Met. Mater. 54 (2016), 831-837. http://dx.doi.org/10.3365/KJMM.2016.54.11.831

161 Y. Fujiwara, M. Izaki, H. Enomoto, A. Nakae, Effects of hydroxycarboxylic acids on the electrodeposition of Fe-C alloys, Denki Kagaku 61 (1993), 840-842.

162 Y. Fujiwara, T. Nagayama, A. Nakae, M. Izaki, H. Enomoto, E. Yamauchi, Electrodeposition of Fe-C alloys from baths containing dicarboxylic acids with a linear alkyl chain, J. Electrochem. Soc. 143 (1996), 2584-2590. http://dx.doi.org/10.1149/1.1837051

163 M. Izaki, H. Enomoto, T. Omi, Hardness and carbon content of Fe electroplate from sulfate bath containing l-ascorbic acid and citric acid, J. Surf. Fin. Soc. Jpn. 40 (1989), 1304-1305. http://dx.doi.org/10.4139/sfj.40.1304

164 M. Izaki, H. Enomoto, A. Nakae, S. Terada, E. Yamauchi, T. Omi, Phase transformations and hardness changes in electrodeposited Fe-C alloy films, J. Surf. Fin. Soc. Jpn. 45 (1994), 1302-1307. http://dx.doi.org/10.4139/sfj.45.1302

165 M. Izaki, T. Omi, Structural characterization of martensitic iron-carbon alloy films electrodeposited from an iron(II) sulfate solution, Metall. Mater. Trans. A 27 (1996), 483-486. http://dx.doi.org/10.1007/BF02648429

166 A.S.M.A. Haseeb, M.Z. Huq, Electrodeposition of martensitic iron-carbon alloy coatings at room temperature, Met. Finish. 95 (1997), 30-34. http://dx.doi.org/10.1016/S0026-0576(97)86770-0

167 Y. Fujiwara, M. Izaki, H. Enomoto, T. Nagayama, E. Yamauchi, A. Nakae, Optimization of bath composition for hard Fe-C alloy plating, J. Appl. Electrochem. 28 (1998), 855-862. http://dx.doi.org/10.1023/A:1003444610964

168 A.S.M.A. Haseeb, Y. Hayashi, M. Masuda, M. Arita, On the nature of the electrochemically synthesized hard Fe-0.96 mass pct C alloy film, Metall. Mater. Trans. B 33 (2002), 921-927. http://dx.doi.org/10.1007/s11663-002-0076-4

169 N. Miyamoto, K. Yoshida, M. Matsuoka, J. Tamaki, Effect of phosphorus content on mechanical properties of electrodeposited Fe-C-P alloys, J. Electrochem. Soc. 151 (2004), C645-C648. http://dx.doi.org/10.1149/1.1785798

170 T. Müller, Pulsed Electrodeposition of Nanocrystalline Co and Co/Cu Alloys, master thesis, Saarland University, 2014.

171 S. Gadad, T.M. Harris, Oxygen incorporation during the electrodeposition of Ni, Fe and Ni-Fe alloys, J. Electrochem. Soc. 145 (1998), 3699-3703. http://dx.doi.org/10.1149/1.1838861

172 H. Seema Mohammadi, M.A. Apoorva, R. Ravishankar, Effect of surfactants on the electrodeposited nickel composite coatings, Int. J. Techn. Res. Appl. 3 (2015), 398-406.

173 W.H. Hall, X-ray line broadening in metals, Proc. Phys. Soc. A 62 (1949), 741-743. http://dx.doi.org/10.1088/0370-1298/62/11/110

174 G.K. Williamson, W.H. Hall, X-ray line broadening from filed aluminium and wolfram, Acta Metall. 1 (1953), 22-31. http://dx.doi.org/10.1016/0001-6160(53)90006-6

175 T. Miller Harris, Hydrogen Diffusion and Trapping in Electrodeposited Nickel, PhD thesis, Massachusetts Institute of Technology, 1989.

176 H. Alimadadi, A. Bastos Fanta, M.A.J. Somers, K. Pantleon, Columns formed by multiple twinning in nickel layers – An approach of grain boundary engineering by electrodeposition, Appl. Phys. Lett. 103 (2013), 031918. http://dx.doi.org/10.1063/1.4816257

177 D.W. Schulze, J.M. Slaughter, C.M. Falco, Molecular beam epitaxy for multilayer fabrication, in: F.E. Christensen (Ed.), X-Ray Multilayers in Diffractometers, Monochromators, and Spectrometers, SPIE Proceedings Vol. 0984, The International Society for Optics and Photonics, Bellingham, 1988. http://dx.doi.org/10.1117/12.948772

178 J. A. Dobrowolski, James R. Pekelsky, R. Pelletier, M. Ranger, Brian T. Sullivan, and A. J. Waldorf, Practical magnetron sputtering system for the deposition of optical multilayer coatings, Appl. Opt. 31 (1992), 3784-3789. http://dx.doi.org/10.1364/AO.31.003784

179 A. Donohue, F. Spaepen, R.G. Hoagland, A. Misra, Suppression of the shear band instability during plastic flow of nanometer-scale confined metallic glasses, Appl. Phys. Lett. 91 (2007), 241905. http://dx.doi.org/10.1063/1.2821227

180 Y. Wang, J. Li, A.V. Hamza, T.W. Barbee Jr., Ductile crystalline-amorphous nanolaminates, Proc. Natl. Acad. Sci. 104 (2007), 11155-11160. http://dx.doi.org/10.1073/pnas.0702344104

181 W. Guo, E. Jägle, J. Yao, V. Maier, S. Korte-Kerzel, J.M. Schneider, D. Raabe, Intrinsic and extrinsic size effects in the deformation of amorphous CuZr/nanocrystalline Cu nanolaminates, Acta Mater. 80 (2014), 94-106. http://dx.doi.org/10.1016/j.actamat.2014.07.027

182 Y.Q. Wang, J.Y. Zhang, X.Q. Liang, K. Wu, G. Liu, J. Sun, Size- and constituent-dependent deformation mechanisms and strain rate sensitivity in nanolaminated crystalline Cu/amorphous Cu-Zr films, Acta Mater. 95 (2015), 132-144. http://dx.doi.org/10.1016/j.actamat.2015.05.007

183 L.M. Goldman, C.A. Ross, W. Ohashi, D. Wu, F. Spaepen, New dual-bath technique for electrodeposition of short repeat length multilayers, Appl. Phys. Lett. 55 (1989), 2182-2184. http://dx.doi.org/10.1063/1.102351

184 N. Nakada, M. Fujihara, T. Tsuchiyama, S. Takaki, Effect of phosphorus on Hall-Petch coefficient in ferritic steel, ISIJ Int. 51 (2011), 1169-1173. http://dx.doi.org/10.2355/isijinternational.51.1169

VI. List of Publications

Publication A

T. Müller, A. Bachmaier, E. Neubauer, M. Kitzmantel, R. Pippan

Strong and Stable Nanocomposites Prepared by High-Pressure Torsion of Cu-Coated Fe Powders

Metals 6 (2016), 228

http://dx.doi.org/10.3390/met6100228

Publication B

T. Müller, M.W. Kapp, A. Bachmaier, R. Pippan

Ultrahigh-Strength Low Carbon Steel Obtained from the Martensitic State via High Pressure Torsion

in preparation

Publication C

T. Müller, A. Bachmaier, A. Stark, N. Schell, R. Pippan

Nanostructured Low Carbon Steels Obtained from the Martensitic State via Severe Plastic Deformation, Precipitation, Recovery and Recrystallization

accepted for publication in Advanced Engineering Materials

Publication D

T. Müller, J. Grimwood, A. Bachmaier, R. Pippan

Electrodeposition of Fe-C Alloys from Citrate Baths: Structure, Mechanical Properties and Thermal Stability

submitted

Publication E

T. Müller, A. Bachmaier, R. Konetschnik, T. Schöberl, R. Pippan

Mechanical Properties of Electrodeposited Amorphous/Crystalline Multilayer Structures in the Fe-P System

Mater. Sci. Eng. A 715 (2018), 83-91

http://dx.doi.org/10.1016/j.msea.2017.12.090

Remarks:

In the appended publications, I, Timo Müller, performed all experiments, data analyses and compositions of the publications with the following exceptions:

- Erich Neubauer and Michael Kitzmantel performed the powder compaction via inductive hot pressing in Publication A.

- Marlene Kapp performed the microcompression tests in Publication B.

- Georg Rathmayr prepared the tensile samples for Publication B.

- Pradipta Ghosh, Andrea Bachmaier, Petra Erdely, Peter Staron, Andreas Stark, Norbert Schell and Torben Fischer helped performing the synchrotron XRD measurements in Publications B, C and D.

- Florian Spieckermann performed the DSC measurements in Publication C.

- Joseph Grimwood performed and analyzed parts of the XRD, nanoindentation and compression experiments in Publication D.

- Thomas Schöberl performed most nanoindentation experiments in Publications D and E.

- Ruth Konetschnik performed the microbending experiments in Publication E.

- Karoline Kormout recorded the HR-TEM images and the TEM-EDX results in Publication E.

- Andrea Bachmaier and Reinhard Pippan contributed to all publications with many ideas and a lot of advice.

Publication A

Strong and Stable Nanocomposites Prepared by High-Pressure Torsion of Cu-Coated Fe Powders

Timo Müller[1], Andrea Bachmaier[1], Erich Neubauer[2], Michael Kitzmantel[2] and Reinhard Pippan[1]

[1] Erich Schmid Institute of Materials Science, Austrian Academy of Sciences, Leoben, Austria

[2] RHP-Technology, Seibersdorf, Austria

Abstract

Segregation and chemical inhomogeneity are well-known problems in powder metallurgy and are also an issue for new applications of powder mixtures, for example as starting materials for severe plastic deformation. In this study, Cu-coated Fe powder was prepared via immersion deposition, inductively hot-pressed and subsequently deformed using high-pressure torsion. The homogeneity of the pressed material was found to be much better than that of powder mixtures that were prepared for comparison. During severe plastic deformation, higher hardness was observed for the coated powder as compared to powder mixtures even after low strains. In the saturation state, the coated powder was found to result in a hardness of about 600 HV, which is significantly harder than for the powder mixtures. This is attributed to the greater amount of impurities introduced by the coating process. It is shown that coated powders are promising starting materials for severe plastic deformation in order to reduce the amount of strain necessary to reach the saturation state and to obtain high strength and more homogeneous mechanical alloying.

A.1. Introduction

High-pressure torsion (HPT) is a promising top-down technique to produce bulk nanostructured materials. In contrast to other methods of severe plastic deformation, even very high strains can be obtained easily [A1]. Besides HPT deformation of bulk materials, the compaction and deformation of powders has introduced new possibilities to this technique. The oxide film on metal powder particles, for example, results in a higher amount of impurities as compared to bulk material which leads to a smaller saturation grain size and higher hardness during deformation [A2]. Also composites of any kind can be obtained easily by mixing the elemental powders of the components [A3].

An important issue for severe plastic deformation of composites is the structural homogeneity of the starting material. Although the initial microstructure does not affect the saturation state, which is obtained after a sufficient amount of strain, it has a strong impact on the homogeneity of deformation and the amount of strain which is necessary to obtain this state of saturation [A4]. In addition, the structural homogeneity of the starting material is also important for the formation of supersaturated solid solutions. This phenomenon has been reported for many systems, even for systems with a high positive enthalpy of mixing, which are generally considered to be immiscible [A5]. Various possible explanations for the supersaturation by plastic deformation have been discussed [A6]. Since homogeneous mixtures of small particles provide short diffusion paths, a large amount of heterogeneous interfaces as well as more parts with very small tips, such a starting material is expected to facilitate intermixing and result in faster formation of supersaturated solutions.

Inhomogeneity can occur in metallurgically prepared starting materials, for example when phase separation occurs on a length scale that approaches the HPT sample size. However, inhomogeneity is also an issue when powder mixtures are used as starting materials. Segregation is especially likely to occur when the various components of the powder mixture differ strongly in size and density, and can be only avoided using laborious techniques of mixing [A7]. On the contrary, if one component is added not as a second powder but as a coating on the powder particles of the other component, segregation cannot take place and the two components are separated in an invariable distance depending only on the size of the particle and the thickness of the coating. Coated powders have been used in [A2] to deform nickel with a significant amount of oxides homogeneously distributed throughout the sample. However, no HPT deformation of coated powders consisting of two metals has been reported so far, to the authors' knowledge.

Such coated powders are investigated in the present study using the Fe-Cu system. According to the phase diagram, the system can be considered as immiscible, since only negligible intermixing of Fe and Cu occurs at room temperature [A8]. However, supersaturated solid solutions have been observed and investigated in many studies using both mechanical alloying (see [A9] and references therein) and severe plastic deformation. Investigations on HPT-deformed Fe-Cu alloys have been reported using various starting materials. Teplov et al. [A10, A11] found single-phase solid solutions of up to 20 at.-% Cu on the iron-rich side and up to 20 at.-% Fe on the copper-rich side of the phase diagram for both master alloys and powder mixtures as starting materials. Bachmaier et al. [A12] developed a two-step HPT process to reduce the saturation grain size and obtain solid solutions in a more efficient way. Up to 15 at.-% from both sides of the phase diagram were found to result in single-phase solid solutions [A12]. For both alloys from the melt and powder mixtures, a continuous refinement of the Fe particles in Cu-rich alloys via

fragmentation and dissolution was reported [A13, A14]. Also, a composite of iron fibers in a copper matrix has been deformed via HPT and the dissolution of the iron fibers was observed [A15-A17]. In these studies, an inhomogeneous deformation of the composite due to Fe-rich and Fe-depleted regions in the samples was reported [A15, A17].

In the present study, copper-coated iron powders as starting materials for HPT deformation were produced via immersion deposition. Immersion deposition is a cheap and versatile technique for coating, since no expensive equipment and no vacuum is required. The immersion deposition of Cu on Fe has been known for more than a century [A18]. However, the deposition on powders is more complex since some processing steps (e.g. fast drying) cannot be directly transferred from the plating of macroscopic parts to powders. The coating of Fe powder with Cu via immersion deposition from an electrolyte with citrate complexation was investigated by Turoňová et al. [A19]. Citrate complexes slow down the deposition rate [A19]. This is not only of interest to reduce the reaction if it is unintended, but also to elongate the deposition process and enable more homogeneous coatings.

The aim of the present study is to investigate the effect of the coated powder on the microstructure and hardness evolution during HPT deformation, as compared to a powder mixture. Special attention is attributed to the homogeneity of the starting material, the deformation behavior as well as the formation of supersaturated solutions.

A.2. Materials and Methods

In this study, three different configurations of Fe-Cu alloys were deformed via high pressure torsion: a copper-coated iron powder, an undeformed powder mixture of iron and copper powders, and a powder mixture after previous HPT deformation. The coated powder was produced via immersion deposition. The electrolyte consisted of $0.8 \text{ mol} \cdot \text{dm}^{-3}$ cupric sulfate pentahydrate and $0.4 \text{ mol} \cdot \text{dm}^{-3}$ tri-sodium citrate dehydrate. Then 12 g of iron powder (-200 mesh, 99+% purity) were immersed in 0.15 cm^3 of electrolyte for 30 s. During this deposition process the bath was agitated using a magnetic stirrer at 500 rpm. Subsequently, the powder was removed from the electrolyte using a magnetic rod. It was rinsed with de-ionized water and isopropyl and then dried in a filter paper (grade MN 615). This procedure was repeated various times to obtain larger amounts of coated powders. Using only small amounts of powders at once enabled the fast removal of the powder from the electrolyte as well as homogeneous coating. The coated powder was compacted by RHP-Technology (Seibersdorf, Austria) using inductive hot pressing at 650 °C and 30 MPa for 15 min. Subsequently, disks of 8 mm diameter and about 0.8 mm height were cut out of the compacted composite and used for HPT deformation.

For comparison, a powder mixture was prepared consisting of 16 g (33 wt.-%) copper powder (−70 + 400 mesh, 99.9% purity) and 32 g (67 wt.-%) iron powder (−100 + 200 mesh, 99.9% purity). It was compacted and cut in the same way as described above for the coated powder.

Besides, a mixture of iron and copper powder, which had been pre-deformed in a larger HPT device, was also used for comparison. A mixture of Fe70Cu30 was prepared from copper (−170 + 400 mesh, 99.9% purity) and iron (−100 + 200 mesh, 99.9% purity) powders. The powder mixture was compacted and a disk of 50 mm diameter and 9.5 mm thickness was deformed via HPT (10 rotations). Disks with 8 mm diameter and about 0.8 mm thickness were cut in such a way from the larger HPT disk, that the axial direction for the following deformation experiments was approximately the radial direction of the previous deformation. A detailed description of this two-step HPT process can be found in [A12].

All samples were deformed via HPT at a pressure of 7.3 GPa with a sample size of 8 mm diameter and about 0.8 mm height. For deformation at elevated temperatures, the anvils and the sample were heated inductively. Room temperature experiments were performed at 0.2 rpm, whereas at elevated temperatures 0.6 rpm was used to reduce deformation time.

The structure of the undeformed and deformed state was investigated using light microscopy as well as scanning electron microscopy (SEM LEO 1525 from Zeiss, Oberkochen, Germany) with a back-scattered electron detector and an electron backscatter diffraction (EBSD) system from EDAX, Mahwah, NJ, USA. Grain size distributions of undeformed materials were obtained directly from EBSD measurements, whereas the grain size after deformation was estimated from manual analysis of SEM images obtained with the back scattered electron detector using ImageJ software. The given grain sizes are the shorter axis of fitted ellipses. The composition of the samples was also investigated with this device using an energy-dispersive x-ray spectroscopy (EDX) system from Oxford Instruments, Abingdon, UK. Vickers microhardness was measured using a Micromet 5104 (from BUEHLER, Chicago, IL, USA) with a load of 100 g (HV 0.1). All microstructural investigations and hardness measurements were carried out on a central cross-section of the HPT disc in tangential direction at different radii.

X-ray diffraction (XRD) experiments were performed with a SmartLab diffractometer (Rigaku Europe SE, Ettlingen, Germany) in parallel beam geometry using Cu-Kα radiation and a secondary monochromator in Leoben. Half of an HPT specimen with the axial direction parallel to the diffraction vector was used for these measurements. For analysis of peak position and peak width, the XRD pattern were fitted with pseudo-Voigt profiles and a parabolic background using Fityk software [A20].

A.3. Results

A.3.1. Initial Structure of the Coated Powder

The as-coated powder consists of Fe cores coated with a Cu layer of about 1-2 μm thickness. The size of the Fe cores varies from a few micrometers up to about a hundred micrometers in the long axis of the mostly ellipsoidal particles. As shown in Figure A1a, the Cu layer does not stick directly on the Fe. This poor adhesion might explain the Cu shells without cores that have been observed in the cross-sections of as-coated powder (Figure A1a), since the Fe core might have been removed during cross-section preparation. Besides, some small pure Cu particles with a size of a few microns are observed in the powder after coating. These might originate either from small Fe powder particles, which were replaced by Cu completely in the deposition process, or from larger Cu shells, which broke due to collisions of particles during powder processing. An improvement of the adhesion and quality of the coating might be achieved using a smaller particle concentration in the electrolyte [A19]. However, this is not investigated in the present study, since good adhesion is not absolutely necessary for the further processing and the amount of electrolyte to produce the same amount of powder would significantly increase.

After inductive hot pressing, the Fe cores of the coated powder particles are still apparent in the microstructure and are separated by a Cu layer network. Most grains of the Cu phase are in the ultra-fine grained region, whereas the Fe grains are 10 times larger (Figure A1b). On a length scale up to tens of microns, Fe- and Cu-rich regions can be found due to the size of the original powder particles. However, the material is very homogeneous on a larger scale (Figure A1c). The overall composition as determined via EDX is 33 wt.-% Cu and 67 wt.-% Fe.

XRD measurements (Figure A1d) show the presence of magnetite, Fe_3O_4, in the coated powder. A magnetite content of about 5 wt.-% was determined using TOPAS software [A21].
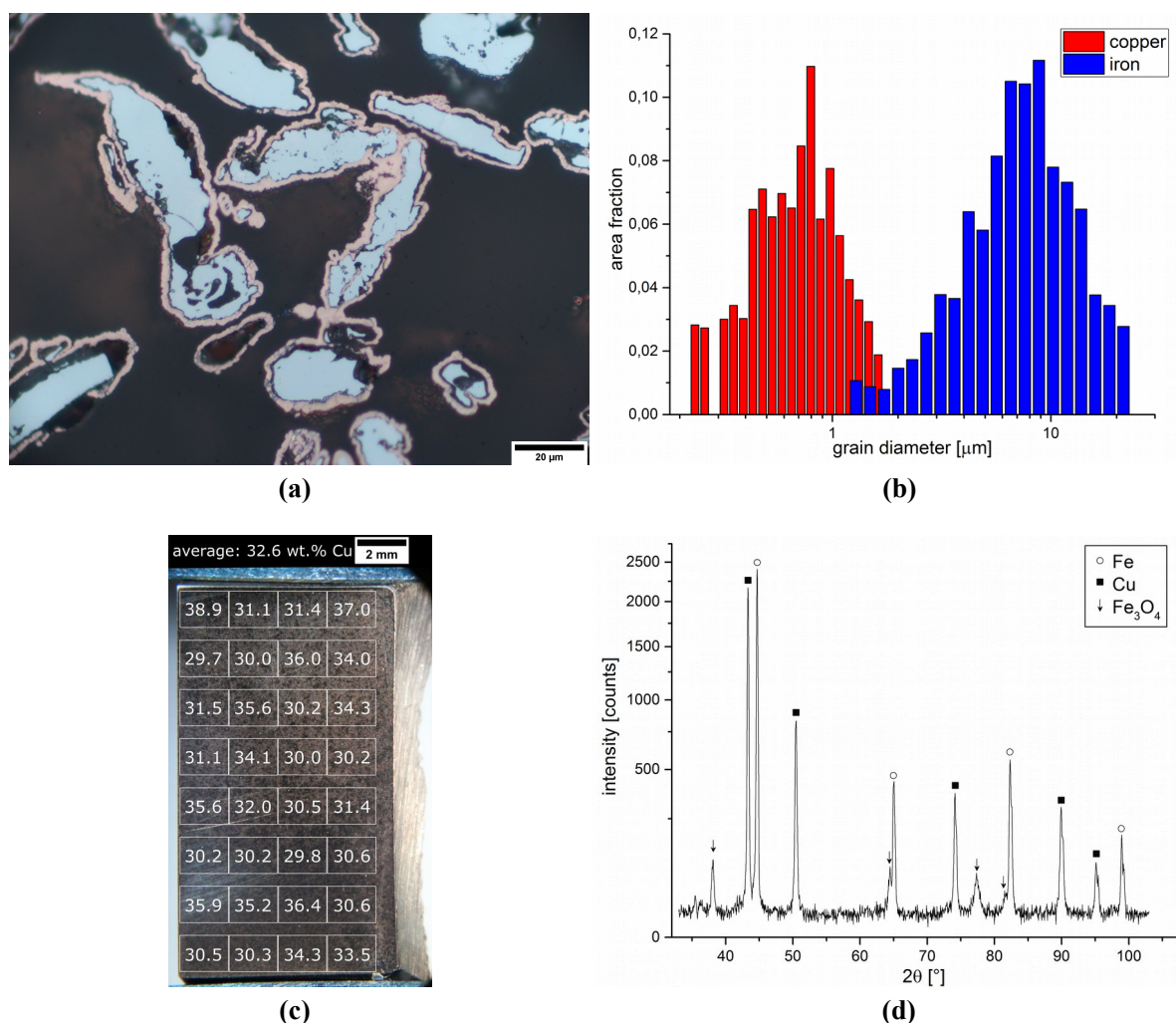
(a)

(b)

(c)

(d)

Figure A1: Structure of the coated powder before deformation: (a) Optical micrograph of a cross-section of powder particles after coating; (b) Grain size distributions- of Cu and Fe phases after hot pressing as obtained from EBSD measurements; (c) Light micrograph of a cross-section of the hot-pressed coated powder. The white overlay indicates the EDX measurement areas and the numbers give the measured Cu contents in wt.-%; (d) XRD pattern after hot pressing indicates a three-phase mixture of Fe, Cu and magnetite.

A.3.2. Initial Structure and Homogeneity of the Powder Mixtures

The powder mixture, which was also inductively hot-pressed, is very inhomogeneous on a macroscopic scale. Figure A2a shows the results of EDX measurements on a cross-section of the hot-pressed material. The concentrations scatter over a larger range on a length scale that is comparable to the size of the HPT samples. Besides the chemical inhomogeneity, a quite coarse structure is observed (Figure A2b). The individual Cu and Fe particles in the pressed material have a size up to several hundred microns. This is a consequence of particle clusters since the original powder particles were significantly smaller.
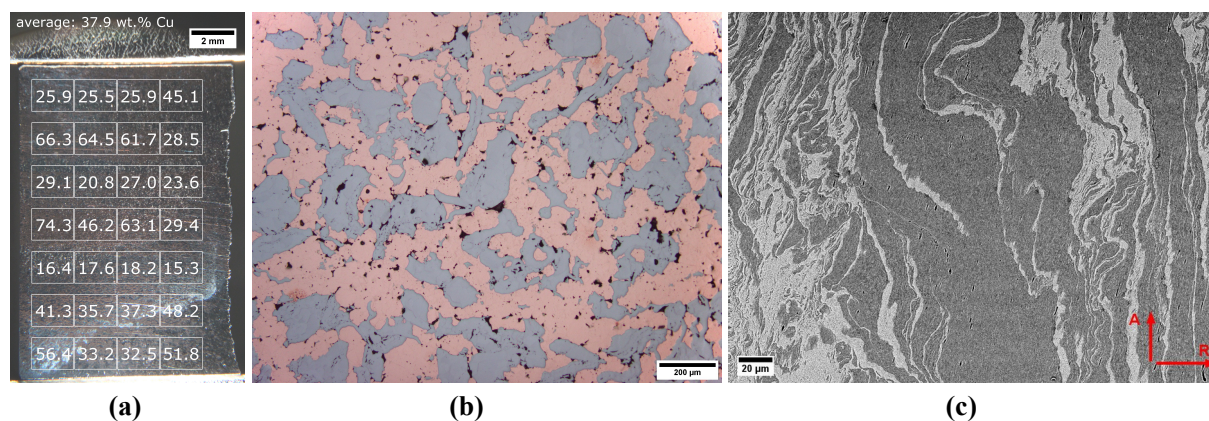
Figure A2: Structure of the powder mixtures before deformation: (a) Optical micrograph of a cross-section of the hot-pressed powder mixture. The numbers in the overlay give the Cu contents in wt.-% as obtained from EDX with measuring regions indicated by the white grid; (b) Optical micrograph showing the coarse structure of the hot-pressed powder mixture (in a Cu-rich region); (c) Back-scattered electron micrograph of the pre-deformed powder mixture. The arrows indicate the axial (A) and radial (R) directions of the second HPT step.

The second powder mixture, which was already pre-deformed in a large HPT tool, shows the typical structure of elongated particles after the first deformation step (Figure A2c). The Cu grains are almost spherical with a grain size of about 200 nm, whereas the Fe grains are mostly elongated with a grain size of 200 to 1000 nm in the long axis and 50 to 300 nm in the short axis. The samples for the second HPT deformation step are cut in such a way that the elongated grains are oriented with the long axis almost parallel to the axial direction of the second HPT deformation (Figure A2c). This results in a re-orientation of the grains in the second deformation step which is expected to accelerate the refinement process. For both powder mixtures, a two-phase mixture of Fe and Cu without any indication of oxides is revealed by XRD.

A.3.3. Structures and Hardness Evolution during Deformation at Room Temperature

For an HPT deformation of up to two turns, the structure refinement results in a linear increase of hardness with applied equivalent strain. The same hardening rate is observed for both the coated powder and the two-step HPT material (Figure A3a). Also the hardness in the center of the HPT discs, where no strain is applied in the idealized case, is the same for these two starting materials. This can be attributed to the ultra-fine-grained structure, which is present in the two-step HPT samples due to the previous deformation and in the Cu phase of the coated powder due to the coating process.
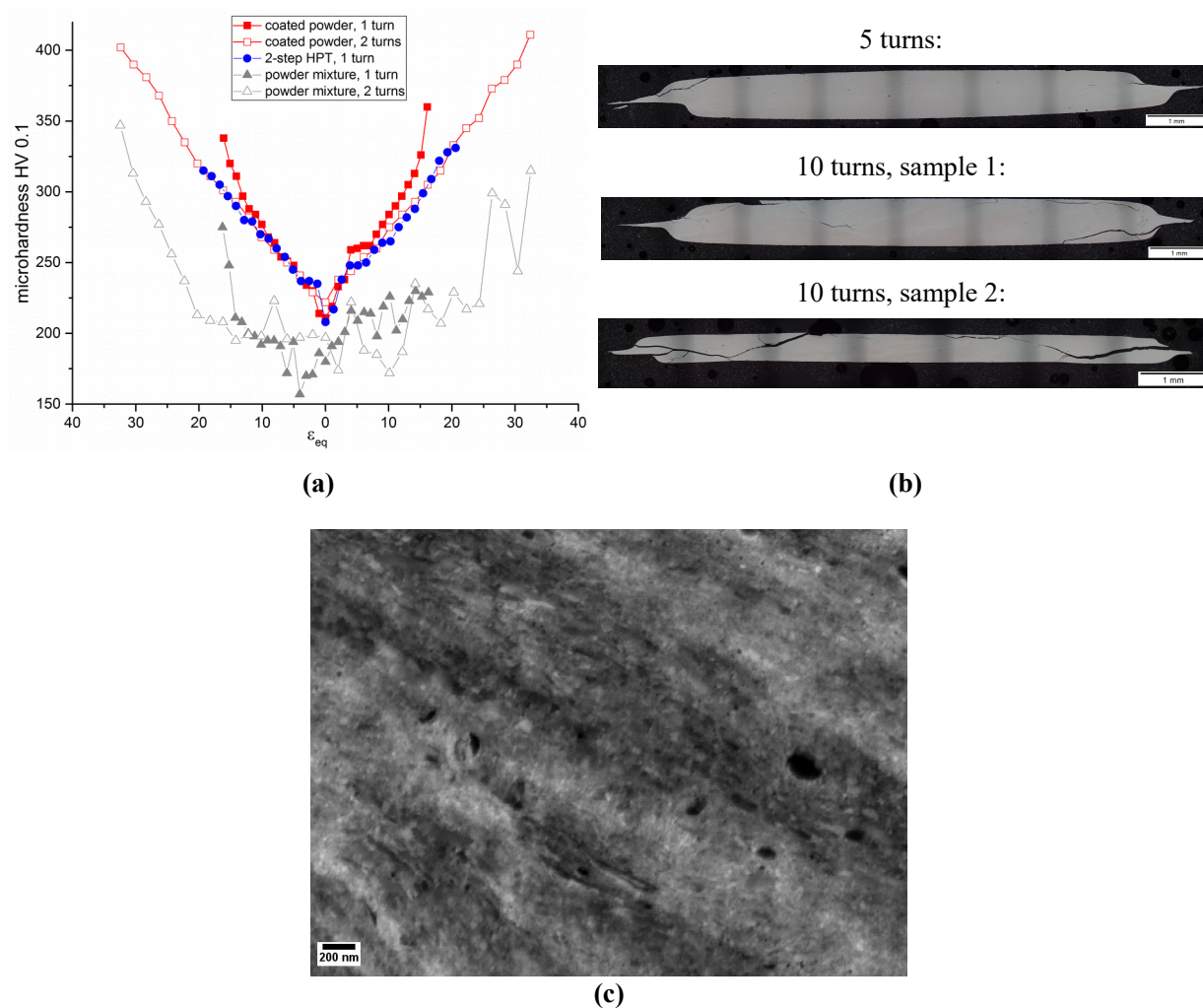
(a)

(b)

(c)

Figure A3: Structure and hardness evolution during HPT at room temperature: (a) Hardness profiles after one and two turns; (b) Optical micrographs of coated powder samples deformed by five or 10 turns, respectively; (c) Microstructure of a coated powder sample after 50 rotations at a radius of 3 mm (ε_{eq} = 700) imaged with back-scattered electron detector.

On the contrary, the hardness of the powder mixture samples is lower and a larger scatter occurs over the cross-section of an HPT sample (Figure A3a). The lower hardness is due to the coarser microstructure in the initial state. The scatter originates from both the chemical inhomogeneity and from the fact that the size of the Cu and Fe phase regions is of the same size or even larger than the microhardness indents. Hence, a higher or lower hardness is measured depending if the indent is placed in a Fe- or Cu-rich region, respectively. Nonetheless, the hardness of the powder mixture increases at approximately the same rate as the other two materials.

Whereas the powder mixtures with and without previous deformation are deformable up to extremely high strains (ε_{eq} > 1000), an increasing probability of crack formation with increasing strain is observed for the coated powder. After five turns (corresponds to ε_{eq} = 90 at the edge of the HPT disk), the first cracks occur at the edge of the sample. With further deformation, the number of cracks significantly increases (Figure A3b). We assume that these cracks are formed

during unloading after deformation. Therefore, the hardness profiles were also measured for fractured samples, since the structure evolution during deformation and thus the hardness should not be influenced. Such materials are of no practical use, and a way to avoid the formation of cracks will be discussed in the next paragraph.

After 50 turns, the hardness starts to saturate at the sample edge for all three starting materials (Figure A4b). Whereas with the coated powder a hardness of about 600 HV is obtained, both powder mixtures reach a maximum hardness of about 450 to 500 HV. For all three materials a nanocrystalline microstructure is obtained, which consists of regions of equi-axed grains co-existing with regions of elongated grains with the short axis in the axial direction of the HPT process
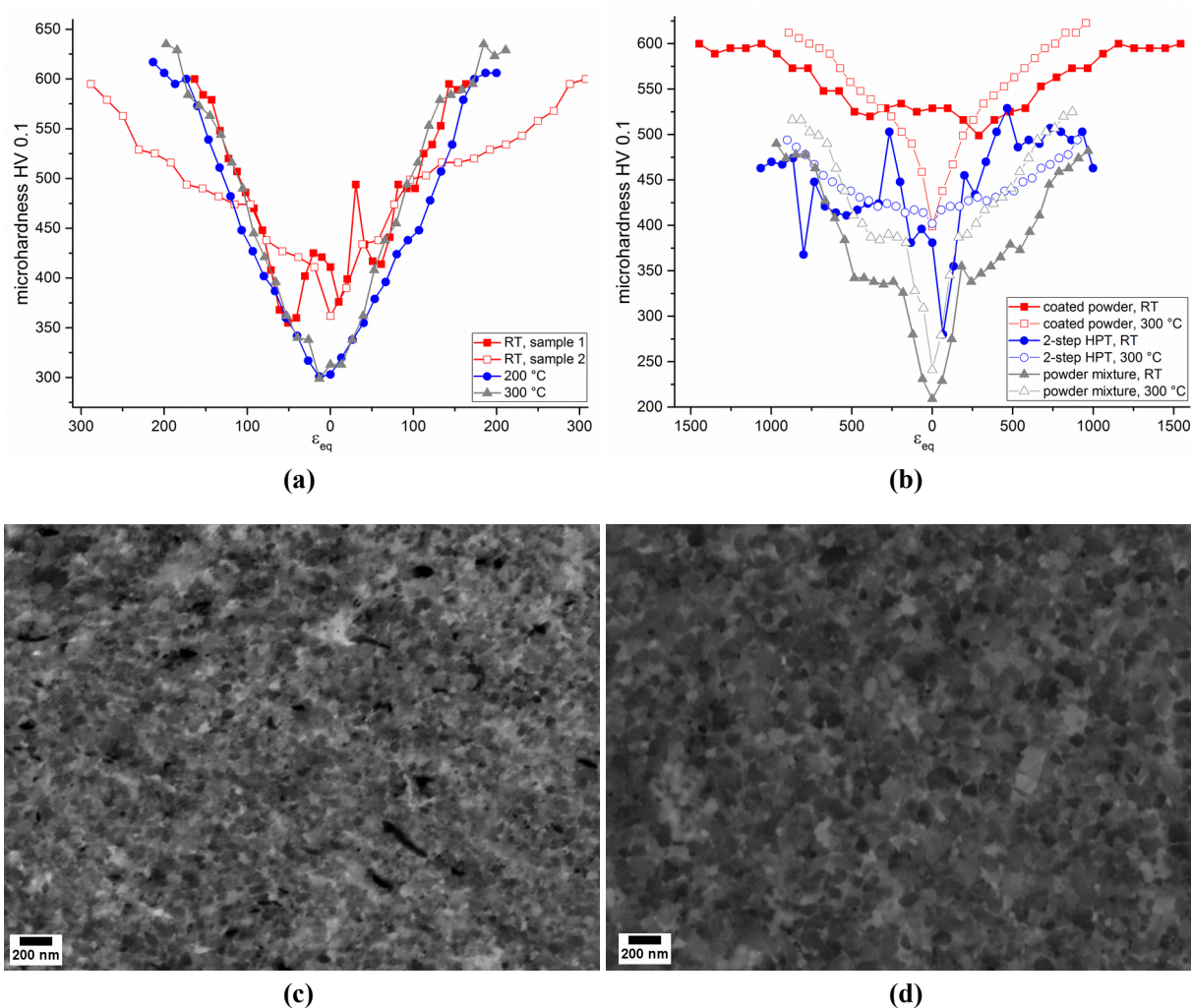

(a)

(b)

(c)

(d)

Figure A4: The effect of elevated temperature on the structure and hardness evolution: (a) Hardness profiles of HPT samples from coated powder after 10 turns at different temperatures (the differences between the two room-temperature samples can be attributed to different amounts of cracking, cf. Figure A3b); (b) Hardness profiles of HPT samples after 50 turns; Back-scattered electron micrographs of (c) coated powder and (d) pre-deformed (two-step HPT) powder mixture after 50 turns at 300 °C, measured at a radius of 3 mm (ε_{eq} = 700 without previous deformation).

(Figure A3c). Cu- and Fe-rich regions can no longer be distinguished in the SEM images for all three starting materials. The grain size in the coated powder sample is about 30 nm, whereas for the two-step HPT sample the grain size ranges from 50 to 100 nm. For the one-step HPT powder mixture, most parts of the sample are similar to the two-step HPT material. However, ultra-fine-grained regions with grain sizes up to several hundred nanometers are also observed, even at the edge of the sample after 50 turns ($\varepsilon_{eq} = 900$).

In the XRD patterns, all peaks of Fe and Cu are broadened and shifted towards smaller diffraction angles with an increasing amount of strain (Figure A5). A correlation of the broadening and the peak shift is observed. After 50 turns both the peak widths and the peak shifts are significantly larger for the coated powder sample as compared to the powder mixtures. The broadening and peak shifts of the two powder mixtures are very similar, with a tendency of slightly more broadening and peak shift for the two-step HPT sample. These results fit in well with the smaller grain size observed for the coated powder sample. However, no quantitative analysis of grain size or lattice parameters from the XRD data is performed, since strong nonlinearities are observed in the Williamson-Hall and Nelson-Riley plots, respectively. Possible explanations will be discussed in Section 4.3. For all deformed samples, no indications of oxide phases are found.
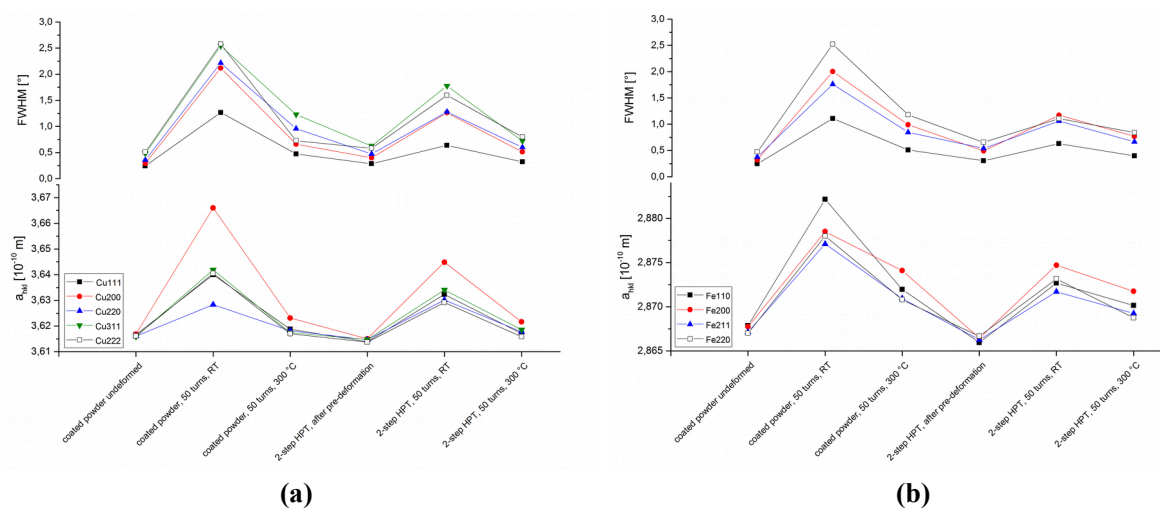

(a)   (b)

Figure A5: Peak width (full width at half maximum, FWHM) and lattice parameter calculated from the XRD peak positions, a_{hkl}, for the (a) Cu and (b) Fe phases.

A.3.4. Structures and Hardness Evolution during Deformation at Elevated Temperatures

To avoid the formation of cracks in the HPT samples of the coated powder, the deformation was performed at elevated temperatures. For all samples deformed at 300 °C, no severe cracking occurred. Figure A4a shows the hardness profiles of coated powder samples after 10 turns of HPT deformation at different temperatures. The same hardness evolution is obtained independent of the deformation temperature. For the deformation at room temperature, a slightly higher hardness is obtained near the center of the HPT disc. However, this is not caused by the deformation temperature, but might be due to a larger misalignment of the central axis of the HPT tool in these experiments.

Also, the saturation hardness, which is obtained after 50 turns at the edge of the sample ($\varepsilon_{eq} = 900$), is similar to the room temperature experiments for all three starting materials (Figure A4b). The difference in hardness of the coated powder sample as compared to the powder mixtures corresponds to a difference in grain size. For the coated powder, the grain size in saturation is about 30 to 50 nm (Figure A4c), whereas for the powder mixtures 60 to 100 nm are measured for both the one-step and two-step HPT deformation (Figure A4d). In contrast to the microstructures after deformation at room temperature, no regions with elongated grains are observed in the saturated regions of the samples deformed at elevated temperatures. As for samples deformed at room temperature, Cu- and Fe-rich regions cannot be distinguished in the SEM images of the saturated state anymore. Hence, only average grain sizes can be given.

XRD peak broadening and peak shifts towards smaller diffraction angles also occur for all samples deformed at 300 °C. As for the room temperature experiments, the broadening and the peak shifts are larger for the coated powder sample than for the powder mixtures (Figure A5). For the latter, no differences of one-step and two-step samples are observed. However, the broadening and the peak shifts obtained after deformation at 300 °C are significantly smaller than for deformation at room temperature. The peak widths and shifts of the coated powder sample deformed at 300 °C are similar to those of the powder mixtures deformed at room temperature for the Fe phase; for the Cu phase they are even smaller. The smaller broadening as compared to the room temperature samples cannot be attributed to a smaller grain size, since the grain size measured in SEM is the same. However, smaller densities of dislocations and small angle boundaries [A22] due to dynamic recovery processes during HPT at elevated temperature may explain the smaller peak broadening. Interestingly, a similar hardness is obtained in spite of these differences in structure.

A.4. Discussion

It has been shown that materials with higher saturation hardness can be obtained from HPT deformation of Cu-coated Fe powder as compared to powder mixtures of Fe and Cu. While the coated starting powders are prone to cracking when deformed at room temperature, extremely high strains can be applied without fracture at elevated temperature. In the following, the impact of the two main differences of the starting materials, chemical homogeneity and impurity concentration, on the structure evolution as well as the resulting differences concerning intermixing of Cu and Fe during deformation will be discussed.

A.4.1. Homogeneity of the Materials

The chemical inhomogeneity of the powder mixture after hot pressing (Figure A2a) results in HPT samples in which the composition varies to a significant extent, both from one sample to another as well as within each sample. The former will result in a scatter of evolving structures and properties. Since the Cu phase is generally softer than the Fe phase, samples with a higher Cu content result in a lower overall hardness after deformation. The inhomogeneity within one sample results in inhomogeneous deformation, strain concentrations and non-symmetric hardness profiles as shown in Figure A3a.

On the very contrary, the coated powder results in very homogeneous structures on all length scales larger than the size of the original powder particles. For all HPT samples from the coated powder, the Cu concentration from EDX measurements varied by less than 6 wt.-%. This homogeneity results in a more uniform deformation and stronger work hardening in the HPT process and consequently in a lower scatter of the hardness profiles (Figure A3a and Figure A4a,b). This makes the structure and the properties of the material after deformation more predictable and therefore more suitable for possible applications. The stronger work hardening is assumed to be due to the higher concentration of heterogeneous interfaces in the initial structure, providing obstacles for dislocation movement, as well as the enhanced intermixing (cf. Section 4.3) impeding the motion of dislocation via pinning of substitutional elements. In addition, the size restriction of Cu- and Fe-rich regions to the size of the initial powder particles reduces the distance of material transport, which has to be achieved via plastic flow to obtain a completely homogeneous saturation state after a certain amount of strain. Therefore, the state of saturation is reached faster than for starting materials where chemical inhomogeneity on a larger length scales is present.

Concerning homogeneity, the pre-deformed powder mixture lies between the undeformed powder mixture and the coated powder. Cu- and Fe-rich regions on a length scale of several hundred

micrometers are observed. Nevertheless, quite symmetric hardness profiles are obtained even at low strains of the second HPT deformation step (Figure A3a). This is attributed to the preliminary HPT deformation step. The change of the rotation axis from the first to the second HPT step results in an alignment of the lamellar structure after the first step that accelerates further structure refinement in the second step [A12]. Therefore, the same hardness values as for the coated powder can be obtained at low strains (Figure A3a). Since the structure and the properties in the saturation state are known not to depend on the microstructure of the starting material [A4], the differences of powder mixtures and coated powder at larger strains cannot be a result of the differences in homogeneity and possible explanations for the differences in the saturation state will be discussed in the following.

A.4.2. The Role of Impurities

As revealed from XRD, the coated powder contains a significant amount of oxides. The bad adhesion of the Cu coating and the compact nature of the Fe cores indicate that the Fe powder particles are oxidized at the surface when immersed in the electrolyte. Since Fe forms no dense oxide films, the coating process is not severely impeded by this oxide film. Also the powder mixtures contain some oxides, since it is well known that both Cu and Fe form native oxide films on their surfaces and the specific surface of the powders is relatively high [A23]. However, the oxide content in the powder mixtures is significantly lower than for the coated powder, which is evident from the XRD patterns.

The oxides found in the coated powder samples represent hard inclusions in a softer metallic matrix. During deformation, fragmentation occurs and parts of the oxides may dissolve in the matrix. Nevertheless, the oxides cause embrittlement and cracking of the samples for room temperature deformation. At elevated temperatures, stress concentrations caused by the oxide particles are reduced due to dynamic recovery and rewelding of small microcracks is more likely to occur. Therefore, no cracks are observed for coated powder samples deformed at elevated temperatures.

Besides this impact on the deformability of the material, the higher amount of oxides in the coated powder also affects the structure and properties in the saturation state. It is well known that the saturation state is a steady state determined by the competition of grain refinement via plastic deformation on the one hand, and dynamic recovery, thermally or mechanically induced coarsening, on the other hand [A1]. No oxide peaks are observed in XRD after deformation. Either the size of the oxides is reduced during deformation to such an extent that the broadened Bragg peaks of the oxide vanish in the background and the neighboring peaks of the metal phases, or parts of the oxygen dissolve in the matrix. Both atomic oxygen and oxide particles on

the nanometer scale provide obstacles for the movement of grain boundaries and stabilize a finer microstructure. The thermal stability of the nanocrystalline microstructure at 300 °C can also be attributed to the stabilization of the grain boundaries by the impurities, which may be thermodynamically or kinetically driven [A24].

In this context, the enhanced impurity level in the coated powder might be a further advantage of these materials as starting materials for HPT deformation, since stronger materials can be obtained, which are also thermally stable up to a certain temperature. However, these effects might also be achieved via powder mixtures with enhanced impurity content. To separate the effects of homogeneity and contamination on the structure and hardness evolution at low strains, further studies with coated powders of different contamination levels, which may be obtained via different coating processes, would be necessary. Nevertheless, the effects of more homogeneous deformation and less strain to obtain the saturation state (as discussed in Section 4.1) are assumed to be mainly due to the homogeneity of the powder mixture and not the higher amount of impurities. These effects could therefore not be obtained with powder mixtures of higher-impurity contents.

A.4.3. Mechanical Alloying

The shifts of the Bragg peaks of both fcc and bcc phases towards lower diffraction angles indicate mechanical alloying of Cu and Fe. However, macroscopic residual stresses and, for the Cu phase, the formation of stacking faults may result in additional peak shifts. Also a dependence of the lattice parameter, i.e. the shift of Bragg peaks, as a function of grain size has been discussed in the literature [A25]. However, the same peak shifts, which were observed in the present study, have already been described by Bachmaier et al. [A12] for the two-step HPT process of Fe-Cu alloys with different compositions, for which supersaturated solid solutions were also observed. In addition, the increase of the lattice parameter with the increasing solute concentration on both sides of the Fe-Cu phase diagram has been reported for supersaturated solid solutions by quenching [A26] and ball milling [A27]. Therefore, it can be concluded that the mutual intermixing of Fe and Cu is the main reason for the observed peak shifts.

With this assumption, the XRD results show an increasing amount of mechanical alloying with increasing peak broadening, i.e. decreasing grain size and increasing microstrain or increasing dislocation density. The larger peak shifts for the deformed coated powder as compared to the powder mixtures indicate that a larger amount of Fe is dissolved in the Cu phase, and vice versa, for the coated powder as starting material. Possible reasons are the smaller grain size and higher densities of stored dislocations, which are both stabilized by the higher amount of impurities. Therefore, the coated powder as a starting material seems to promote the mechanical alloying.

However, more detailed investigations are necessary to manifest this assumption, since also the dissolution of interstitials (e.g. oxygen) from the impurities itself may result in an increase of the lattice parameter, i.e. in a peak shift towards lower angles.

A.5. Conclusions

It is shown that coated powders are an appropriate alternative to powder mixtures in order to improve both the initial structural homogeneity and the homogeneity of deformation in HPT samples prepared via the powder route. The higher homogeneity enables obtaining harder materials even with low strains. Besides, modifications of the material due to the coating process change the structure and properties in the saturation state of severe plastic deformation. In this study, an enhanced impurity concentration induced by immersion coating results in higher hardness due to the impeded grain boundary motion which impedes grain growth and shifts the equilibrium between grain refinement and dynamic recovery towards a smaller grain size.

Author Contributions

T.M., A.B., and R.P. conceived and designed the experiments. T.M. performed the experiments and wrote the manuscript. E.N. and M.K. mixed and compacted the powders. A.B. prepared the pre-deformed HPT material. All authors contributed to the finalization of the manuscript.

References

A1   R. Pippan, F. Wetscher, M. Hafok, A. Vorhauer, I. Sabirov, The limits of refinement by severe plastic deformation, Adv. Eng. Mater. 8 (2006), 1046-1056. http://dx.doi.org/10.1002/adem.200600133

A2   A. Bachmaier, A. Hohenwarter, R. Pippan, New procedure to generate stable nanocrystallites by severe plastic deformation, Scr. Mater. 61 (2009), 1016-1019. http://dx.doi.org/10.1016/j.scriptamat.2009.08.016

A3   A. Bachmaier, R. Pippan, Generation of metallic nanocomposites by severe plastic deformation, Int. Mater. Rev. 58 (2013), 41-62. http://dx.doi.org/10.1179/1743280412Y.0000000003

A4 R. Pippan, A. Bachmaier, A. Hohenwarter, O. Renk, Nanocomposites and super saturated solid solutions generated by SPD: The effect of initial structure and strain path, in: S. Faester (Ed.), Nanometals-Status and Perspective, Proceedings of the 33rd Risø International Symposium on Materials Science, Department of Wind Energy, Technical University of Denmark, Roskilde, 2012, pp. 107-113.

A5 C. Suryanarayana, Mechanical alloying and milling, Prog. Mater. Sci. 46 (2001), 1-184. http://dx.doi.org/10.1016/S0079-6425(99)00010-9

A6 D. Raabe, P.-P. Choi, Y. Li, A. Kostka, X. Sauvage, F. Lecouturier, K. Hini, R. Kirchheim, R. Pippan, D. Embury, Metallic composites processed via extreme deformation: Toward the limits of strength in bulk materials, MRS Bull. 35 (2010), 982-991. http://dx.doi.org/10.1557/mrs2010.703

A7 F. Thümmler, R. Oberacker, Introduction to Powder Metallurgy, The Institute of Materials Series on Powder Metallurgy, London, 1993, p. 113.

A8 B. Predel, Cu-Fe (copper-iron), in: O. Madelung, Landolt-Börnstein–Group IV: Physical Chemistry (Cr-Cs–Cu-Zr), Springer, Berlin, 1994. http://dx.doi.org/10.1007/10086090_1073

A9 J.Z. Jiang, C. Gente, R. Bormann, Mechanical alloying in the Fe-Cu system, Mater. Sci. Eng. A 242 (1998), 268-277. http://dx.doi.org/10.1016/S0921-5093(97)00522-4

A10 V.A. Teplov, V.P. Pilugin, V.S. Gaviko, E.G. Chernyshov, Non-equilibrium solid solution and nanocrystal structure of Fe-Cu alloy after plastic deformation under pressure, Phil. Mag. B 68 (1993), 877-881. http://dx.doi.org/10.1080/13642819308217944

A11 V.A. Teplov, V.P. Pilugin, V.S. Gaviko, E.G. Chernyshov, Nanocrystalline Structure of Non-equilibrium Fe-Cu Alloys Obtained by Severe Plastic Deformation under Pressure, Nanostr. Mater. 6 (1995), 437-440. http://dx.doi.org/10.1016/0965-9773(95)00090-9

A12 A. Bachmaier, M. Kerber, D. Setman, R. Pippan, The formation of supersaturated solid solutions in Fe-Cu alloys deformed by high-pressure torsion, Acta Mater. 60 (2012), 860-871. http://dx.doi.org/10.1016/j.actamat.2011.10.044

A13 A. Lukyanov, A. Churakova, A. Filatov, E. Levion, R. Valiev, D. Gunderov, E. Antipov, Microstructure refinement in Cu-Fe alloys using high pressure torsion, IOP Conf. Ser. Mater. Sci. Eng. 63 (2014), 012102. http://dx.doi.org/10.1088/1757-899X/63/1/012102

A14 L. Krämer, S. Wurster, R. Pippan, Deformation behavior of Cu-composites processed by HPT, IOP Conf. Ser. Mater. Sci. Eng. 63 (2014), 012026. http://dx.doi.org/10.1088/1757-899X/63/1/012026

A15 X. Sauvage, F. Wetscher, P. Pareige, Mechanical alloying of Cu and Fe induced by severe plastic deformation of a Cu-Fe composite, Acta Mater. 53 (2005), 2127-2135. http://dx.doi.org/10.1016/j.actamat.2005.01.024

A16 X. Sauvage, R. Pippan, Nanoscaled structure of a Cu-Fe composite processed by high-pressure torsion, Mater. Sci. Eng. A 410-411 (2005), 345-347. http://dx.doi.org/10.1016/j.msea.2005.08.122

A17 X. Quelennec, A. Menand, J.M. le Breton, R. Pippan, X. Sauvage, Homogeneous Cu-Fe supersaturated solid solutions prepared by severe plastic deformation, Phil. Mag. 90 (2010), 1179-1195. http://dx.doi.org/10.1080/14786430903313682

A18 W.G. Clark, Improved method of coating thin iron or steel sheets, wire or tubing, or small iron articles such as nails or screws, with copper or its alloys, Patent GB 13445 (1909).

A19 A. Turoňová, M. Gálová, M. Gernátová, Study of electroless copper deposition on Fe powder, Particul. Sci. Technol. 26 (2008), 126-135. http://dx.doi.org/10.1080/02726350701483842

A20 M. Wojdyr, Fityk: A general-purpose peak fitting program, J. Appl. Cryst. 43 (2010), 1126-1128. http://dx.doi.org/10.1107/S0021889810030499

A21 Bruker AXS, TOPAS V4: General profile and structure analysis software for powder diffraction data, User's manual, Bruker AXS, Karlsruhe, 2008.

A22 T. Ungár, G. Tichy, J. Gubicza, R.J. Hellmig, Correlation between subgrains and coherently scattering domains, Powder Diffr. 20 (2005), 366-375. http://dx.doi.org/10.1154/1.2135313

A23 S. Suzuki, Y. Ishikawa, M. Isshiki, Y. Waseda, Native oxide layers formed on the surface of ultra high-purity iron and copper investigated by angle resolved XPS, Mater. Trans. JIM 38 (1997), 1004-1009.

A24 R.A. Andrievski, Review of thermal stability of nanomaterials, J. Mater. Sci. 49 (2014), 1449-1460. http://dx.doi.org/10.1007/s10853-013-7836-1

A25 G.K. Rane, U.Welzel, S.R. Meka, E.J. Mittemeijer, Non-monotonic lattice parameter variation with crystallite size in nanocrystalline solids, Acta Mater. 61 (2013), 4524-4533. http://dx.doi.org/10.1016/j.actamat.2013.04.021

A26 W. Klement, Solid solutions in copper-iron alloys quenched rapidly from the melt, Trans. Met. Soc. AIME 233 (1965), 1080-1082.

A27 E. Gaffet, M. Harmelin, F. Faudot, Far-from equilibrium phase transition induced by mechanical alloying in the Cu-Fe system, J. Alloy. Compd. 194 (1993), 23-30. http://dx.doi.org/10.1016/0925 8388(93)90640 9

Publication B

Ultrahigh-Strength Low Carbon Steel Obtained from the Martensitic State via High Pressure Torsion

Timo Müller, Marlene W. Kapp, Andrea Bachmaier and Reinhard Pippan

Erich Schmid Institute of Materials Science, Austrian Academy of Sciences, Leoben, Austria

Abstract

A new ultrahigh-strength structure is created by plastic deformation of a martensitic 0.1 wt.-% C steel using high pressure torsion (HPT) at room temperature. Tensile tests reveal an ultimate tensile strength of 2.4 ± 0.1 GPa – to our knowledge the highest tensile strength ever reported for a carbon steel with such low carbon content. During HPT, a lamellar microstructure is formed with decreasing lamellar spacing for increasing plastic strain. Micropillar compression gives crucial insights into the mechanical properties which are correlated to the deformation behavior of this material. Strong similarities as compared to HPT-treated pearlitic steel are found in spite of the large differences concerning both carbon content and phase composition. The possibilities and limits of strength maximization in carbon steels are evaluated and discussed.

B.1. Introduction

The improvement of mechanical properties is a key topic of steel research since centuries. Today's strongest steels are cold-drawn pearlitic wires which can reach a tensile strength up to almost 7 GPa [B1] while still sustaining a reasonable fracture toughness in certain loading directions [B2]. The structure of this heavily deformed pearlite consists of nanocrystalline ferrite supersaturated in carbon. The carbon is mainly segregated at dislocations and interfaces and originates from the cementite phase that is dissolved during the deformation process [B3-B6]. A very similar structure is found in the so-called white-etching layer at the surface of rail tracks [B7]. This layer is formed by the severe wear during usage and can reach a hardness up to 14 GPa [B8]. To obtain these ultra-strong steels in a larger bulk volume, alternative techniques of severe plastic deformation (SPD) have to be applied. Indeed, the dissolution of cementite and the supersaturation of carbon in the ferritic phase have been observed after deformation with various methods such as rolling [B9], ball milling [B10, B11] or high pressure torsion (HPT) [B12-B15].

However, the kinetics of the dissolution process depend on the strain path, and, thus, the SPD technique. Whereas the complete dissolution of cementite is reported for cold-drawn wires for equivalent strains of less than ten [B1, B16, B17], accessibility of a single-phase solid solution via HPT requires plastic strains that are more than an order of magnitude larger [B12, B18].

On the other hand, martensitic carbon steel, i.e. single-phase solid solutions of carbon in ferrite via quenching, are known since more than a century. Many similarities of the ultra-strong supersaturated solutions by SPD and conventional martensite have been found, which even lead to the term "deformation-induced martensite" [B17]. However, significant differences exist in the amount and structure of dislocation arrangements and interfaces. In the quenched martensite, orientation relationships are an immediate result of the martensitic transformation and laths, the smallest microstructural units of a martensitic low carbon steel, have a typical width of 100-200 nm [B19]. On the other hand, the grains of the supersaturated structures after SPD have a size of about 10 nm and are separated by heavily distorted, random high-angle grain boundaries [B1, B20].

Whereas the formation of single-phase solid solutions via HPT calls for very large plastic strains, a strong increase in dislocation density as well as grain refinement are commonly observed already at moderate plastic strains [B21]. Thus, HPT of quenched martensitic steel might be an efficient way to create bulk ultra-strong steels since the difficult task of cementite dissolution is already solved a priori. On the other hand, the plastic deformation of martensitic carbon steel is technologically challenging due to its high strength and brittleness. Tsuji et al. have shown that conventional cold rolling of martensitic steel and subsequent annealing can be used to produce a high-strength material with considerable thermal stability [B22]. An enormous strengthening capability by rolling to larger thickness reductions was demonstrated by Zhao et al. [B23], but is rarely used due to the difficult processing of as-quenched martensite. Previous ageing at moderate temperatures can be used to facilitate larger thickness reductions, i.e. larger strains, during cold rolling [B24]. Ball milling of martensitic steel powder has also been investigated [B10]. However, all investigations concerning bulk SPD methods were performed either after tempering or at elevated temperature during the deformation process, which improves the deformability of the martensite (see [B25, B26] and references therein). However, precipitation of carbides might take place during annealing, depending on the composition of the material and the temperature treatments. Furthermore, the accessible grain size by SPD usually increases with increasing deformation temperature [B21]. Thus, structures similar to the SPD pearlite cannot be obtained under those conditions.

In this study, the possibilities and limits of SPD of martensitic steel at room temperature are investigated. HPT is chosen as the most suitable SPD technique in this case since large strains can easily be applied and the hydrostatic pressure during deformation is supposed to suppress crack formation. The structure and mechanical properties of a HPT-treated low carbon martensite are investigated and compared to that of pearlitic steels after SPD.

B.2. Experimental

The martensitic structure of a Ck10 plain carbon steel was obtained by isothermal annealing for 15 minutes at 1000 °C in air and subsequent quenching in salt water. After grinding the top and bottom surface, the disk-shaped samples of 8 mm diameter and about 0.8 mm height were deformed via HPT at room temperature. The HPT device was operated with a hydrostatic pressure of 7.3 GPa and a rotational speed of 0.2 rpm.

A Zeiss LEO 1525 scanning electron microscope (SEM) and a Philips CM 12 transmission electron microscope (TEM) were used for microstructural analysis. High-energy X-ray diffraction (XRD) experiments in transmission were performed using synchrotron radiation with a photon energy of 100 keV at the P07 HEMS beamline at PETRA III (Hamburg, Germany) [B27]. The primary beam had a size of 0.32x0.32 mm² and was oriented in axial direction of the HPT samples. The 2D diffraction patterns were integrated using Fit2D software [B28].

Vickers microhardness was measured with a load of 500 g (HV0.5) using a Buehler Micromet 5104 machine. Tensile samples with a circular cross-section of 0.2 mm diameter were prepared with the tensile axis in tangential direction of the HPT samples. The detailed tensile sample preparation and testing procedure is described in [B29]. Micropillars of 4x4x8 mm³ size were prepared by ion slicing and subsequent FIB milling as described in [B30]. Micropillars were tested with the loading direction in axial direction (normal to the lamellae), in radial direction (parallel to the lamellae) and with an inclined orientation of about 45° to both the axial and radial axis. Sample preparation was done using a Zeiss LEO 1540XB machine with a current of 200 pA for the final polishing step. Deviation from a cuboidal shape due to taper formation was minimized by an overtilt of 1.3° during FIB milling. ASMEC UNAT-SEM microindenter mounted in a Zeiss LEO 982 SEM was used for in-situ compression of the pillars with a strain rate of 10-3 s. The measured displacements were corrected for the compliance of the setup as proposed in [B31].

B.3. Results

B.3.1 Microhardness and Structural Analysis

During HPT, the hardness of the martensite increases from 420 ± 10 HV in the as-quenched state up to a maximum of about 750 HV (Figure B1a). Until an equivalent strain of about $\varepsilon_{vM} = 5$, the hardness increase is approximately proportional to the equivalent strain (Figure B1b). However, for larger strains the hardness also seems to depend on the number of rotations. Cracks along the shear plane, starting at the edge of the HPT disks, occur in the outer region of most samples after one turn. For higher numbers of turns, cracks extend towards the center and are present in all samples. On the other hand, samples with less than one turn only occasionally contain cracks near the edge. For this reason, the following analysis is restricted to samples with one turn and up to a radius of $r = 3$ mm ($\varepsilon_{vM} = 15$), where only few cracks are found.

The as-quenched steel is a typical lath martensite with an approximate average lath width of 200 nm and without any preferred orientation on the macroscopic scale. After one turn HPT, the elongated grains are strongly oriented along the shear direction. TEM micrographs reveal a relatively wide grain size distribution ranging from about 30 to 100 nm in axial direction at $\varepsilon_{vM} = 5$ (Figure B2a+b). Whereas most grains are already aligned in the shear direction, few regions with larger misorientation to the shear plane are also found using the SEM (not shown here). At $\varepsilon_{vM} = 15$, the grain size in axial direction is further reduced to 30 nm (Figure B2c) and both TEM and SEM show a lamellar structure perfectly aligned in the shear plane.
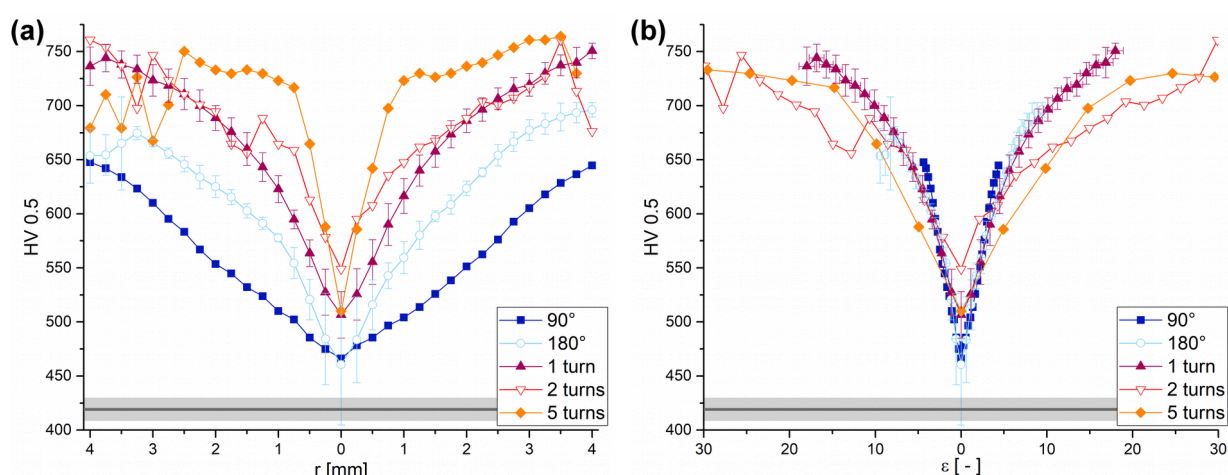

Figure B1: Microhardness profiles after different amounts of plastic deformation as a function of (a) the radius of the HPT disk and (b) the equivalent strain. For certain conditions, several samples are prepared and the vertical error bars indicate the standard deviations from the measurements on different samples. The horizontal error bars in (b) indicate the strain inaccuracy obtained via error propagation from the standard deviations of sample heights. The gray horizontal lines show the average hardness of the as-quenched state ± standard deviation.
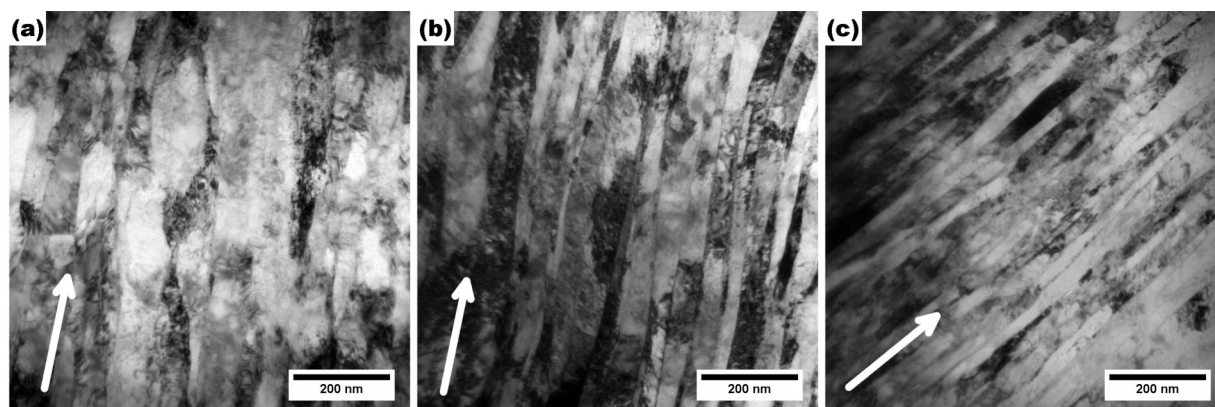
Figure B2: TEM micrographs of a sample after one turn HPT. (a) and (b) are taken at a radius of $r = 1$ mm ($\varepsilon_{vM} = 5$) whereas (c) is from the same sample at $r = 3$ mm ($\varepsilon_{vM} = 15$). The white arrows indicate the shear direction.

XRD shows that retained austenite is present in the as-quenched state, whereas for a sample hydrostatically compressed for 60 seconds at 7.3 GPa in the HPT device as well as for all HPT-deformed samples no indications of retained austenite are found (Figure B3). According to the results of Rietveld refinement, the amount of retained austenite in the as-quenched state equals 1.5 wt.-%. No additional phases can be found in the XRD data of both the as-quenched and the HPT-treated martensite, whereas the cementite in the as-received state can clearly be resolved (Figure B3).

B.3.2 Tensile Tests

The tensile tests reveal a strong increase of strength after HPT processing (Figure B4). Both the yield stress, $\sigma_{0.2}$, and the ultimate tensile strength, σ_{UTS}, are more than doubled by the HPT treatment (1 turn, $r = 1.5$ mm, $\varepsilon_{vM} = 7.5$), whereas the elongation at fracture is significantly reduced (Table B1). The post-mortem SEM investigations on the as-quenched samples show
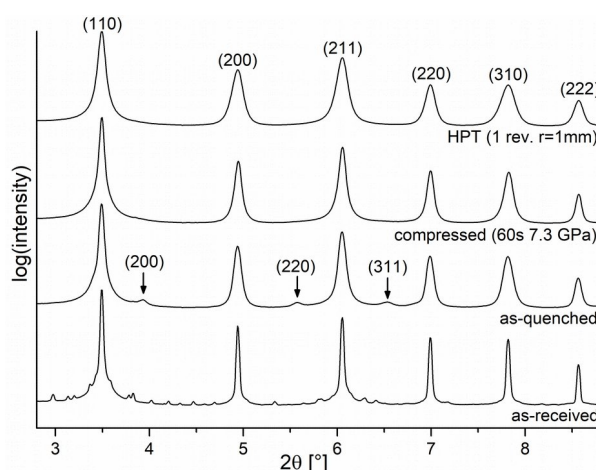

Figure B3: Integrated XRD patterns of as-received, as-quenched, compressed and HPT-treated material. The arrows at the profile of the as-quenched martensite indicate the Bragg peaks of retained austenite (additional austenite peaks are not visible due to overlap with the ferrite peaks).
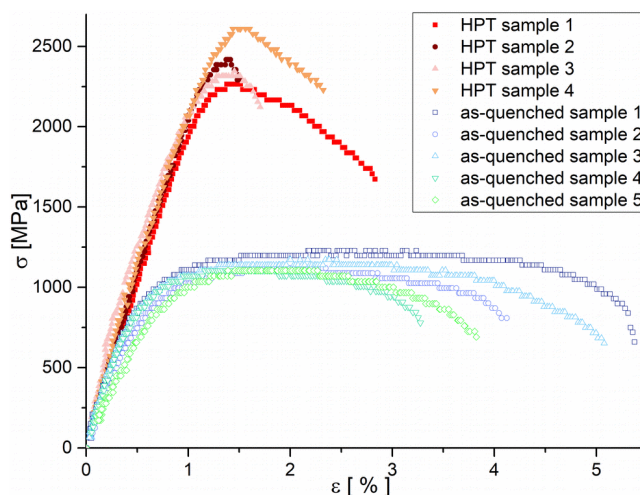
Figure B4: Engineering stress-strain curves of as-quenched and HPT-treated martensite tested in tension along tangential direction (1 turn, $r = 1.5$ mm, $\varepsilon_{vM} = 7.5$).

Table B1: Yield stresses at 0.2 % plastic strain, $\sigma_{0.2}$, ultimate tensile stresses, σ_{UTS}, and fracture strains, ε_f, of the tensile tests. The values are obtained as the average and standard deviations of the five as-quenched and four HPT-deformed samples shown in Figure B4.

	as-quenched	HPT-treated
		(1 turn, $r = 1.5$ mm, $\varepsilon_{vM} = 7.5$)
$\sigma_{0.2}$ [MPa]	935 ± 17	2161 ± 249
σ_{UTS} [MPa]	1146 ± 54	2409 ± 148
ε_f [%]	4.0 ± 0.9	1.2 ± 0.7

strong necking and a dimpled fracture surface which indicates microductile fracture behavior (Figure B5a). Whereas small dimples can also be found for the HPT-treated samples, the main characteristic feature of the fracture surface in this case are cracks and large height steps along the direction of tension (Figure B5b). Cracks ranging more than 100 µm from the fracture surface are observed.
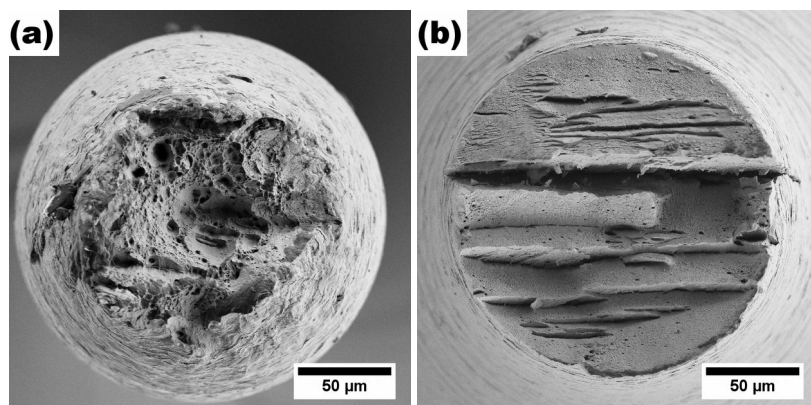

Figure B5: Exemplary fracture surfaces of (a) as-quenched and (b) HPT-treated martensite after tensile tests (1 turn, $r = 1.5$ mm, $\varepsilon_{vM} = 7.5$).

B.3.3 Micropillar Compression

The micropillar compression tests (ε_{vM} = 15) reveal the anisotropic mechanical behavior of the martensitic structure after HPT processing. Figure B6 shows the stress-strain curves which have been truncated after the first strong strain burst for better clarity (the full stress-strain curves are shown in the supplementary). The yield stress, $\sigma_{0.2}$, as well as the flow stress at 1% plastic strain, σ_1, are the largest in the orientation with the lamellae parallel to the loading axis (Figure B6a). Whereas the stresses in normal direction are only slightly smaller (Figure B6b), they are reduced by about one third for the inclined loading direction (Figure B6c). The SEM images of the micropillars after testing show that in parallel orientation a kink band is formed (Figure B6d). The stress-strain curves and the in-situ SEM image sequences reveal that the kink band formation, which takes place after a short range of homogeneous plastic deformation, results in a first load drop. Subsequently, plastic deformation is localized in the kink band. On the contrary, catastrophic failure via the formation of a single sharp shear band is observed for loading perpendicular to the lamellae (Figure B6e). The only exception is one sample, for which only a sharp load drop was measured during the formation of the first shear band, followed by catastrophic failure via the formation of a second shear band. However, in this case, the first shear band is not completely within the micropillar, but runs into the base material which explains the different behavior. For the inclined orientation, multiple shear bands are formed resulting in load drops in approximately equidistant strain intervals (Figure B6c+f). Exemplary in-situ videos for all testing directions can be found in the supplementary.

B.4. Discussion

B.4.1 Deformability and Structure Evolution of Martensitic Steel

The results clearly show that martensitic carbon steel can be deformed via HPT with equivalent strains going far beyond the range of conventional cold deformation such as rolling. HPT results in a uniform orientation of the elongated grains in the shear plane accompanied by a significant reduction of grain size (Figure B2). Furthermore, the dislocation density increases and grain boundaries become distorted with random misorientation, i.e. the orientation relationships of the interfaces in lath martensite are destroyed. These structural changes result in a hardness increase up to about 80% starting from the martensitic low carbon steel, which is already more than three times harder than the corresponding ferritic-pearlitic near-equilibrium structure.

Concerning the phase composition, the only change during HPT is the elimination of the retained austenite which already takes place in the initial compression step of the HPT process. This deformation-induced transformation of retained austenite is well-known [B32]. Although retained
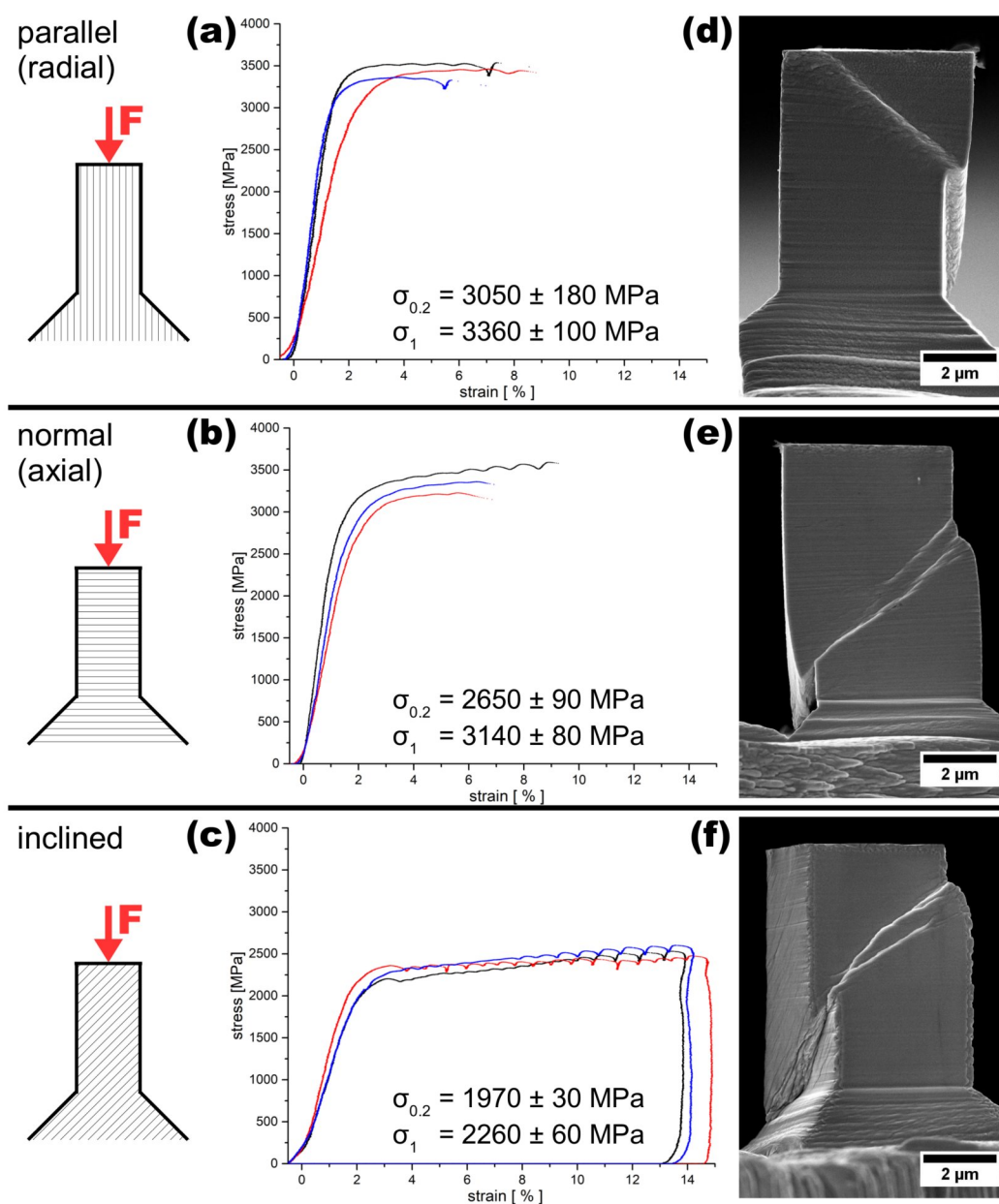
Figure B6: Engineering stress-strain curves from micropillar compression of HPT-deformed martensite (1 turn, $r = 3$mm, $\varepsilon_{vM} = 15$) tested in (a) parallel, (b) normal and (c) inclined loading direction. The three curves in each graph correspond to three different micropillars tested in each direction and the yield stresses at 0.2 % and 1 % plastic strain, $\sigma_{0.2}$ and σ_1, are given as the average value with the standard deviation from the three samples each. Corresponding exemplary post-mortem SEM images for the three orientations are shown in (d-f).

austenite can cause a reduced strength and enhanced ductility [B32], no significant effect of this transformation on the mechanical behavior of the material in this study is expected due to the low fraction of retained austenite in the as-quenched state.

In short, the HPT-deformed structure is a single-phase supersaturated solid solution of carbon in ferrite with strongly oriented, elongated grains reach a short axis of about 30 nm at $\varepsilon_{vM} = 15$. Thus, the structure is very similar to the structures that are formed via cold-drawing of pearlitic

steels. Major differences are the higher carbon content and the even smaller grain size of about 10 nm in the cold-drawn wires [B1, B17].

Further grain refinement of the martensitic low carbon steel is impeded by the formation of cracks at the most severely deformed regions of the HPT samples and the subsequent crack growth towards the center with ongoing deformation. Furthermore, the strength at the edge of the samples after one turn already approaches the strength of the HPT anvils in this study, which were made of a high-speed steel. For these reasons, a saturation state in terms of a dynamic equilibrium between grain refinement and dynamic recovery, which might result in even higher strength, cannot be reached. The use of stronger materials for the HPT tool and the optimization of the cavity geometry of the anvils to protract crack formation may pave the way to even stronger, more heavily deformed structures and is the subject of ongoing work.

B.4.2. Discussion of the Tensile Strength

The comparison of the tensile test results (Table B1) and the hardness at the corresponding position of the HPT samples (1 turn, $r = 1.5$ mm, $\varepsilon_{vM} = 7.5$, 660 HV) shows that the hardness is only increased by about 60 % whereas the ultimate tensile strength is approximately doubled after HPT. The relative increase of the yield stress, $\sigma_{0.2}$, is even higher. Thus, the regularly reported proportional change of hardness and yield (or ultimate tensile) stress [B33, B34] does not hold in the present case. An estimation of the tensile properties from the hardness measurements using the most common conversion factor of three would overestimate of the tensile strength (and even more significantly the yield stress) of the as-quenched state, whereas the strength of the HPT-treated samples would be underestimated. A probable explanation of the non-proportional evolution of hardness and tensile strength upon HPT processing is the conversion of a macroscopically isotropic into an anisotropic structure, since the tensile strength is measured in the strongest direction whereas the complex stress state under the Vickers indenter implies a complex averaging of all orientations. The anisotropy becomes also visible in the fracture surfaces of the tensile samples. The as-quenched martensite shows pronounced necking and subsequent microductile fracture without any signs of anisotropy (Figure B5a). On the contrary, the shear plane can be clearly identified in the fracture surfaces of the HPT-treated samples (Figure B5b). In the necking regime, strong cracks and surface height steps disclose the shear plane as the direction of facilitated crack growth. During its way through the cross-section, the propagating crack is deflected multiple times into the HPT shear plane, i.e. the loading axis, although the driving force for crack propagation in this direction is significantly reduced. The crack growth along the shear plane might be facilitated by the large amounts of straight interfaces in this direction. These findings are in full agreement with the investigations on the anisotropic

fracture toughness of other lamellar structures obtained via HPT, such as pearlitic or duplex steels [B35, B36].

To the authors' best knowledge, the tensile strength measured for the HPT-treated martensite is the highest tensile strength ever measured for a carbon steel with only 0.1 wt.% carbon. Also for low carbon steels with higher carbon contents, only Zhao et al. reported a slightly higher tensile strength of up to 2.5 GPa for a martensitic 0.17 wt.-% carbon steel after severe cold rolling ($\varepsilon_{vM} = 3.1$) and subsequent annealing at 100 °C, i.e. using a similar approach as in this study [B23]. Whereas measurements of $\sigma_{0.2}$ were inhibited by brittle fracture of the samples in [B23], some ductility was still preserved in the present case, even though there is a large scatter in the fracture strain (Figure B4, Table B1).

Other studies using lower plastic strains could not reach such high strength as reported in this study. By cold-rolling to 50 % thickness reduction ($\varepsilon_{vM} = 0.8$), Tsuji et al. obtained an ultimate tensile strength of about 1.5 GPa for a martensitic 0.13 wt.-% C steel, that had a similar strength than the steel of the present study in the as-quenched state [B22]. Also HPT at elevated temperatures with larger equivalent strains than in the present study results in significantly smaller tensile strength [B37]. On the other hand, the tensile strength in the present study is still far from the 7 GPa obtained for a cold-drawn pearlitic steel [B1]. This difference is mainly attributed to the differences in carbon content and grain size and will be further discussed later.

B.4.3. Deformation Mechanisms under Compression – a Comparison to Pearlitic Steels and Multilayers

The behavior of the micropillars during compression has striking similarity to the observations by Kapp et al. on an HPT-deformed pearlitic steel [B38]. The formation of a single shear band for a loading direction normal to the lamellae, the kink band formation for the parallel orientation and the formation of multiple shear bands in the inclined orientation are observed in both cases. Also the high strength in normal and parallel orientation as compared to the inclined arrangement is inherent to both HPT-deformed, lamellar structures. The main differences are the strain hardening capacity and the strains up to both strain localization and catastrophic failure which are all much higher in the case of the pearlite. Although the pearlitic structure in [B38] had a slightly higher hardness of 740 HV and a smaller lamellar spacing of 15 to 20 nm as compared to the HPT-deformed martensitic structure in the present study, plastic deformation starts at lower stresses, manifested in lower yield strengths $\sigma_{0.2}$. However, the flow stresses at a plastic strain of 5 %, that are reported in [B38] for the pearlite, exceed the maximum stresses measured in the martensitic structure for all three orientations (except a single value measured for the strongest sample in

normal direction). Thus, the strain hardening capacity of the HPT-deformed low carbon martensite is much lower than for the nanolamellar pearlite. This can be contributed to the structural differences. The strain hardening capability of the pearlite in [B38] originates from its two-phase composite structure of ferrite and cementite. The elastic resistance of the cementite prohibits strain localization and, thus, enables strain hardening of the ferritic phase up to larger stresses. On the contrary, the elastically responding second phase is absent in the martensitic samples in the present study and the ferritic phase must contain a higher concentration of crystallographic defects in order to reach the same hardness as the pearlitic composite. Thus, plastic deformation starts at higher stresses, but less additional hardening can take place during the compression of the HPT-deformed martensite. For this reason, no strain localization is observed for less than 5 % plastic strain in all three testing orientations for the HPT-deformed pearlite [B38], but strain localization sets in earlier with a large scatter ranging from about 1 to 8 % plastic strain for the HPT-deformed martensite (Figure B6).

Although the lamellar structure consists of a single phase with segregation-stabilized grain boundaries as compared to the two-phase lamellar pearlite in [B38], the orientation-dependent strain localization phenomena, which determine the maximum stresses, are the same in both cases. The onset of strain localization in pearlitic steel is usually attributed to the plastic deformation or the fracture of the cementite lamellae as discussed in [B38]. However, in the present study, there is no cementite but only aligned interfaces, which are decorated with enhanced concentrations of carbon. The similar behavior in all three testing directions indicates that the specific occurrence of the three strain localization phenomena in the three loading directions does not require a lamellar structure of alternating soft and hard phases, but only a lamella-like spatial modulation of strength. These modulations enable local bending and kink band formation for the parallel loading direction, formation of a sharp kink band by breaking or deformation-induced softening of the harder component in the direction of maximum shear stress for normal loading and concentrated dislocation motion within individual lamellae of the softer component for inclined orientations.

The formation of a kink band for compression parallel to the lamella plane is a very general mechanism. It has been reported for a large variety of lamellar structures at different length scales, ranging from stacks of paper [B39] to layered rock formations [B40]. It was also observed for the compression of nanostructured Cu-Nb laminates prepared by accumulative roll-bonding [B41] as well as for sputtered Al-SiC nanolaminates [B42].

Also the failure by strain localization and softening in a shear band for the normal loading direction has been reported for a number of multilayer systems, which include metal-metal [B43-B50], metal-ceramic [B42, B51-B53] and metal-metallic glass [B54] composites. In many

systems it competes with the lateral flow and extrusion of the softer phase, particularly for increasing lamellae thickness and at elevated testing temperatures [B46-B49, B53]. For this orientation, brittle fracture via the formation of vertical cracks in the harder phase has been found as another failure mechanism [B42]. However, in contrast to all these studies, the lamellar structure of the HPT-deformed martensite consists only of one phase. Thus, the absence of the second phase excludes the two alternative deformation or failure mechanisms and results in the formation of a shear band.

As for the pearlite, catastrophic shear banding in two-phase multilayers is usually attributed to the failure or localized deformation of the harder phase resulting in the loss of the lamella interface as an obstacle for dislocation movement of the softer phase [B51]. Transferring this mechanism to the single-phase material in this study, the carbon-stabilized, aligned interfaces inhibit the dislocation movement in the individual lamellae. Once such an obstacle is locally destroyed, softening in this region results in the strain localization and failure along a sharp shear band. For the inclined orientation, the highest shear stress is applied parallel to the layers inducing localized intralamellar shear deformation. This is independent of the nature of the two-dimensional dislocation obstacles, i.e. if lamellae of a second (harder) phase or carbon-stabilized interfaces are present. For this reason, shear banding under inclined loading can be observed for the martensite in this study as well as for sputtered Cu-Nb [B44] or Cu-PdSi [B54] multilayers. The relative reduction of strength in the inclined orientation as compared to normal loading is similar for the martensite and the sputtered two-phase multilayers in [B44] and [B54] indicating that the carbon-stabilized interfaces of the HPT-deformed martensite are comparatively effective as dislocation obstacles as compared to the phase boundaries in the multilayers. However, more work is necessary to investigate the actual deformation mechanisms in the HPT-deformed martensite in order to understand the analogies and differences to the well-investigated two-phase multilayer systems in detail.

B.4.4. How much carbon is necessary to stabilize an ultrahigh-strength steel?

Due to the strong similarities concerning both structure and mechanical behavior of the SPD martensite in this study and SPD pearlitic structures in literature, the question arises if further development of the current approach might compete with the strength of the "deformation-induced martensite" [B17]. So far, most studies on maximizing the strength of carbon steels have been concentrated on near-eutectoid compositions with pearlitic starting materials [B1, B17, B20]. Since the strength after SPD is not obtained from a two-phase structure, but rather from a dissolution of the cementite into interface-stabilizing carbon clusters, the only advantage of near-

eutectoid compositions is the fine and homogeneous distribution of the two phases – and thus also of the carbon – as compared to ferritic-pearlitic structure or the mixture of pearlite and cementite in the hypo- or hypereutectoid rang, respectively. This is also supported by the accelerating effect of a homogeneous, fine-lamellar distribution of cementite on its dissolution during SPD as reported by Shabashov et al. [B55]. As shown in this study, a homogeneous carbon distribution can be easily obtained using martensitic starting materials, which is principally not limited to any specific carbon contents.

Thus, this approach allows to choose the carbon content in order to optimize structure and properties. Whereas the plastic strain in rolling is limited due to the decreasing sample thickness, the deformation via HPT can be arbitrarily extended in principle. However, crack formation must be prevented which might be achieved by enhanced hydrostatic pressure, optimized cavity design of the anvils and optimization of the alignment of the HPT tool. Furthermore, the increasing strength for higher carbon contents requires even stronger materials for the anvils. Additional problems with high carbon steels might originate from the larger amounts of retained austenite which may result in inhomogeneous deformation. Thus, SPD of martensite is a promising technique to obtain new ultrahigh-strength carbon steels, but it is – at least until now – limited to low carbon contents and needs more scientific research and technological progress to exploit all its capabilities.

B.5. Conclusion

SPD of a martensitic low carbon steel is shown as a new promising technique to produce ultrahigh-strength carbon steels. In particular, this is confirmed by the following results:

1. The tensile strength of 2.4 ± 0.1 GPa after an equivalent strain of $\varepsilon_{vM} = 7.5$ is the highest tensile strength reported for a low carbon steel with 0.1 wt.-% C. Since no saturation state is reached during SPD, principally even higher strengths could be achievable by further optimization of the HPT process. This possibility is illustrated by the compressive strength of up to 3.4 GPa for $\varepsilon_{vM} = 15$.

2. The single-phase solid solution with strongly aligned, elongated grains after HPT deformation is very similar to that of SPD pearlitic steels, which are the strongest steels known today. In contrast to the pearlitic steels, where a homogeneous phase distribution is only obtained for the eutectoid composition, the homogeneous carbon distribution in the HPT-treated martensite can be obtained in a large compositional range.

3. The very similar behavior of the HPT martensite as compared to two-phase nanolaminates in micropillar compression along any loading direction indicates that the deformation mechanisms for multilayers and for the pearlitic structure, that have been discussed in literature in detail, also hold for the deformed martensitic structure, i.e. they do not require a lamellar two-phase composite, but rather a lamellar modulation of strength.

Acknowledgements

References

B1 Y. Li, D. Raabe, M. Herbig, P.-P. Choi, S. Goto, A. Kostka, H. Yarita, C. Borchers, R. Kicherheim, Segregation stabilizes nanocrystalline bulk steel with near theoretical strength, Phys. Rev. Lett. 113 (2014) 106104. http://dx.doi.org/10.1103/PhysRevLett.113.106104

B2 A. Hohenwarter, B. Völker, M.W. Kapp, Y. Li, S. Goto, D. Raabe, R. Pippan, Ultra-strong and damage tolerant metallic bulk materials: A lesson from nanostructured pearlitic steel wires, Sci. Rep. 6 (2016) 33228. http://dx.doi.org/10.1038/srep33228

B3 A.R. Waugh, S. Paetke, D.V. Edmonds, A study of segregation to the dislocation substructure in patented steel wire using atom-probe techniques, Metallography 14 (1981) 237-251. http://dx.doi.org/10.1016/0026-0800(81)90029-X

B4 J. Languillaume, G. Kapelski, B. Baudelet, Cementite dissolution in heavily cold drawn pearlitic steel wires, Acta Mater. 45 (1997) 1201-1212. http://dx.doi.org/10.1016/S1359-6454(96)00216-9

B5 H.G. Read, W.T. Reynolds, K. Hono, T. Tarui, APFIM and TEM studies of drawn pearlitic wire, Scripta Mater. 37 (1997) 1221-1230. http://dx.doi.org/10.1016/S1359-6462(97)00223-6

B6 Y.J. Li, P. Choi, C. Borchers, S. Westerkamp, S. Goto, D. Raabe, R. Kirchheim, Atomic-scale mechanisms of deformation-induced cementite decomposition in pearlite, Acta Mater. 59 (2011) 3965-3977. http://dx.doi.org/10.1016/j.actamat.2011.03.022

B7 S.B. Newcomb, W.M. Stobbs, A transmission electron microscopy study of the white-etching layer on a rail head, Mater. Sci. Eng. 66 (1984) 195-204. http://dx.doi.org/10.1016/0025-5416(84)90180-0

B8 W. Lojkowski, Y. Millman, S.I. Chugunova, I.V. Goncharova, M. Djahanbakhsh, G. Bürkle, H.-J. Fecht, The mechanical properties of the nanocrystalline layer on the surface of railway tracks, Mater. Sci. Eng. A303 (2001) 209-215. http://dx.doi.org/10.1016/S0921-5093(00)01948-1

B9   V.N. Gridnev, V.G. Gavrilyuk, I.Ya. Dekhtyar, Yu. Ya. Meshkov, P.S. Nizin, V.G. Prokopenko, Investigation of carbide phase in stained steel by the method of nuclear gamma resonance, Phys. Stat. Sol. (a) 14 (1972) 689-694. http://dx.doi.org/10.1002/pssa.2210140238

B10   M. Umemoto, Z.G. Liu, K. Masuyama, X.J. Hao, K. Tsuchiya, Nanostructured Fe-C alloys produced by ball milling, Scripta Mater. 44 (2001) 1741-1745. http://dx.doi.org/10.1016/S1359-6462(01)00794-1

B11   S. Ohsaki, K. Hono, H. Hidaka, S. Takaki, Characterization of nanocrystalline ferrite produced by mechanical milling of pearlitic steel, Scripta Mater. 52 (2005) 271-276. http://dx.doi.org/10.1016/j.scriptamat.2004.10.020

B12   Yu. Ivanisenko, W. Lojkowski, R.Z. Valiev, H.-J. Fecht, The mechanism of formation of nanostructure and dissolution of cementite in a pearlitic steel during high pressure torsion, Acta Mater. 51 (2003) 5555-5570. http://dx.doi.org/10.1016/S1359-6454(03)00419-1

B13   Yu. Ivanisenko, I. MacLaren, X. Sauvage, R.Z. Valiev, H.-J. Fecht, Shear-induced $\alpha \rightarrow \gamma$ transformation in nanoscale Fe-C composite, Acta Mater. 54 (2006) 1659-1669. http://dx.doi.org/10.1016/j.actamat.2005.11.034

B14   F. Wetscher, R. Pippan, S. Sturm, F. Kauffmann, C. Schau, G. Dehm, TEM investigations of the structural evolution in a pearlitic steel deformed by high-pressure torsion, Metall. Mater. Trans. A 37A (2006) 1963-1968. http://dx.doi.org/10.1007/s11661-006-0138-3

B15   X. Sauvage, Y. Ivanisenko, The role of carbon segregation on nanocrystallisation of pearlitic steels processed by severe plastic deformation, J. Mater. Sci. 42 (2007) 1615-1621. http://dx.doi.org/10.1007/s10853-006-0750-z

B16   K. Hono, M. Ohnuma, M. Murayama, S. Nishida, A. Yoshie, T. Takahashi, Cementite decomposition in heavily drawn pearlitic steel wire, Scripta Mater. 44 (2001) 977-983. http://dx.doi.org/10.1016/S1359-6462(00)00690-4

B17   S. Djaziri, Y. Li, G.A. Nematollahi, B. Grabowski, S. Goto, C. Kirchlechner, A. Kostka, S. Doyle, J. Neugebauer, D. Raabe, G. Dehm, Deformation-induced martensite: A new paradigm for exceptional steels, Adv. Mater. 28 (2016) 7753-7757. http://dx.doi.org/10.1002/adma.201601526

B18   A.V. Korznikov, Yu. V. Ivanisenko, D.V. Laptionok, I.M. Safarov, V.P. Pilyugin, R.Z. Valiev, Influence of severe plastic deformation on structure and phase composition of carbon steel, Nanostruct. Mater. 4 (1994) 159-167. http://dx.doi.org/10.1016/0965-9773(94)90075-2

B19   G. Krauss, A.R. Marder, The morphology of martensite in iron alloys, Metall. Trans. 2 (1971) 2343-2357. http://dx.doi.org/10.1007/BF02814873

B20   Y.J. Li, P. Choi, S. Goto, C. Borchers, D. Raabe, R. Kirchheim, Evolution of strength and microstructure during annealing of heavily cold-drawn 6.3 GPa hypereutectoid pearlitic steel wire, Acta Mater. 60 (2012) 4005-4016. http://dx.doi.org/10.1016/j.actamat.2012.03.006

B21   R. Pippan, F. Wetscher, M. Hafok, A. Vorhauer, I. Sabirov, The limits of refinement by severe plastic deformation, Adv. Eng. Mater. 8 (2006) 1046-1056. http://dx.doi.org/10.1002/adem.200600133

B22   N. Tsuji, R. Ueji, Y. Minamino, Y. Saito, A new and simple process to obtain nano-structured bulk low-carbon steel with superior mechanical property, Scripta Mater. 46 (2002) 305-310. http://dx.doi.org/10.1016/S1359-6462(01)01243-X

B23   X. Zhao, T.F. Jing, Y.W. Gao, G.Y. Qiao, J.F. Zhou, W. Wang, Annealing behavior of nano-layered steel produced by heavy cold-rolling of lath martensite, Mater. Sci. Eng. A 397 (2005) 117-121. http://dx.doi.org/10.1016/j.msea.2005.02.007

B24 E. Ghassemali, A. Kermanpur, A. Najafizadeh, Microstructural evolution in a low carbon steel during cold rolling and subsequent annealing, J. Nanosci. Nanotechnol. 10 (2010) 6177-6181. http://dx.doi.org/10.1166/jnn.2010.2578

B25 M.V. Karavaeva, S.K. Nurieva, N.G. Zaripov, A.V. Ganeev, R.Z. Valiev, Microstructure and mechanical properties of medium-carbon steel subjected to severe plastic deformation, Met. Sci. Heat Treat. 54 (2012) 155-159. http://dx.doi.org/10.1007/s11041-012-9473-8

B26 M.V. Karavaeva, M.A. Nikitina, A.V. Ganeev, R.K. Islamgaliev, High-strength state of ultrafine-grained martensitic steel produced by high pressure torsion, IOP Conf. Ser.: Mater. Sci. Eng. 179 (2017) 012037. http://dx.doi.org/10.1088/1757-899X/179/1/012037

B27 N. Schell, A. King, F. Beckmann, T. Fischer, M. Müller, A. Schreyer, The high energy materials science beamline (HEMS) at PETRA III, Mater. Sci. Forum 772 (2014) 57-61. http://dx.doi.org/10.4028/www.scientific.net/MSF.772.57

B28 A.P. Hammersley, S.O. Svensson, M. Hanfland, A.N. Fitch, and D. Häusermann, Two-dimensional detector software: From real detector to idealised image or two-theta scan, High Pressure Res. 14 (1996) 235-248. http://dx.doi.org/10.1080/08957959608201408

B29 G.B. Rathmayr, A. Bachmaier, R. Pippan, Development of a new testing procedure for performing tensile tests on specimens with sub-millimetre dimensions, J. Test. Eval. 41(4) (2013) 635-646. http://dx.doi.org/10.1520/JTE20120175

B30 S. Wurster, C. Motz, M. Jenko, R. Pippan, Micrometer-sized specimen preparation based on ion slicing technique, Adv. Eng. Mater. 12 (2010) 61-64. http://dx.doi.org/10.1002/adem.200900263

B31 S. Wurster, C. Motz, R. Pippan, Characterization of the fracture toughness of micro-sized tungsten single crystal notched specimens, Philos. Mag. 92 (2012) 1803-1825. http://dx.doi.org/10.1080/14786435.2012.658449

B32 G. Krauss, Martensite in steel: strength and structure, Mater. Sci. Eng. A273-275 (1999) 40-57. http://dx.doi.org/10.1016/S0921-5093(99)00288-9

B33 D. Tabor, The hardness and strength of metals, J. I. Met. 79 (1951) 1-18.

B34 E.J. Pavlina, C.J. Van Tyne, Correlation of yield strength and tensile strength with hardness for steels, J. Mater. Eng. Perform. 17 (2008) 888-893. http://dx.doi.org/10.1007/s11665-008-9225-5

B35 A. Hohenwarter, A. Taylor, R. Stock, R. Pippan, Effect of large shear deformations on the fracture behavior of a fully pearlitic steel, Metall. Mater. Trans. 42A (2011) 1609-1618. http://dx.doi.org/10.1007/s11661-010-0541-7

B36 K.T. Schwarz, K.S. Kormout, R. Pippan, A. Hohenwarter, Impact of severe plastic deformation on microstructure and fracture toughness evolution of a duplex-steel, Mater. Sci. Eng. A 703 (2017) 173-179. http://dx.doi.org/10.1016/j.msea.2017.07.062

B37 A.V. Ganeev, M.V. Karavaeva, X. Sauvage, E. Courtois-Manara, Y. Ivanisenko, R.Z. Valiev, On the nature of high-strength state of carbon steel produced by severe plastic deformation, IOP Conf. Ser.: Mater. Sci. Eng. 63 (2014) 012128. http://dx.doi.org/10.1088/1757-899X/63/1/012128

B38 M.W. Kapp, A. Hohenwarter, S. Wurster, B. Yang, R. Pippan, Anisotropic deformation characteristics of an ultrafine- and nanolamellar pearlitic steel, Acta Mater. 106 (2016) 239-248. http://dx.doi.org/10.1016/j.actamat.2015.12.037

B39 G.W. Hunt, T.J. Dodwell, J. Hammond, On the nucleation and growth of kink and shear bands, Philos. Trans. Royal Soc. A 371 (2013) 20120431. http://dx.doi.org/10.1098/rsta.2012.0431

B40 S. Misra, S. Ellis, N. Mandal, Fault damage zones in mechanically layered rocks: The effects of planar anisotropy, J. Geophys. Res. Solid Earth 120 (2015) 5432-5452. http://dx.doi.org/10.1002/2014JB011780

B41 T. Nizolek, N.A. Mara, I.J. Beyerlein, J.T. Avallone, T.M. Pollock, Enhanced plasticity via kinking in cubic metallic nanolaminates, Adv. Eng. Mater. 17 (2015) 781-785. http://dx.doi.org/10.1002/adem.201400324

B42 C.R. Mayer, L.W. Yang, S.S. Singh, J. Llorca, J.M. Molina-Aldareguia, Y.L. Shen, N. Chawla, Anisotropy, size, and aspect ratio effects on micropillar compression of Al-SiC nanolaminate composites, Acta Mater. 114 (2016) 25-32. http://dx.doi.org/10.1016/j.actamat.2016.05.018

B43 N.A. Mara, D. Bhattacharyya, P. Dickerson, R.G. Hoagland, A. Misra, Deformability of ultrahigh strength 5 nm Cu/Nb nanolayered composites, Appl. Phys. Lett. 92 (2008) 231901. http://dx.doi.org/10.1063/1.2938921

B44 N.A. Mara, D. Bhattacharyya, J.P. Hirth, P. Dickerson, A. Misra, Mechanism for shear banding in nanolayered composites, Appl. Phys. Lett. 97 (2010) 021909. http://dx.doi.org/10.1063/1.3458000

B45 I.J. Beyerlein, N.A. Mara, J.S. Carpenter, T. Nizolek, W.M. Mook, T.A. Wynn, R.J. McCabe, J.R. Mayeur, K. Kang, S. Zheng, J. Wang, T.M. Pollock, Interface-driven microstructure development and ultra high strength of bulk nanostructured Cu-Nb multilayers fabricated by severe plastic deformation, J. Mater. Res. 28 (2013) 1799-1812. http://dx.doi.org/10.1557/jmr.2013.21

B46 P. Dayal, M.Z. Quadir, C. Kong, N. Savvides, M. Hoffman, Transition from dislocation controlled plasticity to grain boundary mediated shear in nanolayered aluminum/palladium thin films, Thin Solid Films 519 (2011) 3213-3220. http://dx.doi.org/10.1016/j.tsf.2010.12.112

B47 J.M. Wheeler, R. Raghavan, V. Chawla, J. Zechner, I. Utke, J. Michler, Failure mechanisms in metal-metal nanolaminates at elevated temperatures: Microcompression of Cu-W multilayers, Scripta Mater. 98 (2015) 28-31. http://dx.doi.org/10.1016/j.scriptamat.2014.11.007

B48 R. Raghavan, J.M. Wheeler, T.P. Harzer, V. Chawla, S. Djaziri, K. Thomas, B. Philippi, C. Kirchlechner, B.N. Jaya, J. Wehrs, J. Michler, G. Dehm, Transition from shear to stress-assisted diffusion of copper-chromium nanolayered thin films at elevated temperatures, Acta Mater. 100 (2015) 73-80. http://dx.doi.org/10.1016/j.actamat.2015.08.016

B49 J. Snel, M.A. Monclús, A. Castillo-Rodríguez, N. Mara, I.J. Beyerlein, J. Llorca, J.M. Molina-Aldareguía, Deformation mechanism map of Cu/Nb nanoscale metallic multilayers as a function of temperature and layer thickness, JOM 69 (2017) 2214-2226. http://dx.doi.org/10.1007/s11837-017-2533-1

B50 Y. Cui, B. Derby, N. Li, N.A. Mara, A. Misra, Suppression of shear banding in high-strength Cu/Mo nanocomposites with hierarchical bicontinuous intertwined structures, Mater. Res. Lett. 6 (2018) 184-190. http://dx.doi.org/10.1080/21663831.2018.1431315

B51 S.M. Han, M.A. Phillips, W.D. Nix, Study of strain softening behavior of Al-Al3Sc multilayers using microcompression testing, Acta Mater. 57 (2009) 4473-4490. http://dx.doi.org/10.1016/j.actamat.2009.06.007

B52 D. Bhattacharyya, N.A. Mara, P. Dickerson, R.G. Hoagland, A. Misra, Compressive flow behavior of Al-TiN multilayers at nanometer scale layer thickness, Acta Mater. 59 (2011) 3804-3816. http://dx.doi.org/10.1016/j.actamat.2011.02.036

B53 S. Lotfian, M. Rodríguez, K.E. Yazzie, N. Chawla, J. Llorca, J.M. Molina-Aldareguía, High temperature micropillar compression of Al/SiC nanolaminates, Acta Mater. 61 (2013) 4439-4451. http://dx.doi.org/10.1016/j.actamat.2013.04.013

B54 I. Knorr, N.M. Cordero, E.T. Lilleodden, C.A. Volkert, Mechanical behavior of nanoscale Cu/PdSi multilayers, Acta Mater. 61 (2013) 4984-4995. http://dx.doi.org/10.1016/j.actamat.2013.04.047

B55 V.A. Shabashov, L.G. Korshunov, A.G. Mukoseev, V.V. Sagaradze, A.V. Makarov, V.P. Pilyugin, S.I. Novikov, N.F. Vildanova, Deformation-induced phase transitions in a high-carbon steel, Mater. Sci. Eng. A 346 (2003) 196-207. http://dx.doi.org/10.1016/S0921-5093(02)00549-X

Publication C

Nanostructured Low Carbon Steels Obtained from the Martensitic State via Severe Plastic Deformation, Precipitation, Recovery and Recrystallization

Timo Müller[1], Andrea Bachmaier[1], Andreas Stark[2], Norbert Schell[2] and Reinhard Pippan[1]

[1] Erich Schmid Institute of Materials Science, Austrian Academy of Sciences, Leoben, Austria

[2] Institute of Materials Research, Helmholtz-Zentrum Geesthacht Centre for Materials and Costal Research, Geesthacht, Germany

Abstract

The range of accessible microstructures from the combination of severe plastic deformation (SPD) and heat treatments of a low carbon steel martensite under various processing conditions is evaluated. SPD results in a temperature decrease for recrystallization and austenitization upon subsequent annealing. On the contrary, the precipitation of cementite takes place at higher temperatures after SPD. Whereas a certain thermal stability is observed for subsequent processing, even low annealing temperatures have a strong impact on the results of simultaneous SPD and heat treatments which results from the differences of dynamic and static recovery. It is shown that with each processing sequence unique microstructures can be produced that have to be taken into account in order to produce a material with optimized tailored properties.

C.1. Introduction

Severe plastic deformation (SPD) and phase transformations can both be used to prepare nanostructured high-strength materials. A combination of both can significantly reduce the strain, which is necessary to obtain ultrafine-grained or even nanocrystalline structures during plastic deformation [C1, C2]. On the other hand, the combination of the processes maintaining the high strains of SPD may open up new possibilities to create microstructures that are not accessible by other methods. The two processes can be combined in any temporal sequence, i.e. with the phase transformation before, during or after plastic deformation. The alternating repetition of the two processes is an additional possibility, but will not be further considered in the following [C1].

In this work, the combination of heat treatments, i.e. carbide precipitation accompanied by recovery and recrystallization, and SPD of martensitic steel is investigated. Tsuji et al. have shown that ultrafine-grained structures can be obtained from martensite by conventional cold-rolling (equivalent strain ε_{vM} = 0.8) followed by annealing [C3]. However, studies on SPD at room temperature of tempered martensite or on SPD of martensitic steel followed by annealing do not exist to the authors' knowledge. The only exception is a study on high pressure torsion (HPT) of a tempered martensitic steel by Karavaeva et al., but the high tempering temperature of 800°C in this study is much higher than the temperatures used in the present work and results in the almost complete loss of the enhanced strength from the previous martensitic transformation [C4]. On the other hand, simultaneous heat treatment and SPD of martensitic steels has already been reported in a number of studies. This is probably due to the brittleness and resulting experimental challenges for SPD of these materials at room temperature.

Dobatkin et al. deformed martensitic 0.14 wt.-% C and 0.1 wt.-% C-B steels via equal-channel angular pressing at 300 °C and proved the enhanced strength and more uniform microstructure after additional subsequent annealing as compared to the ferritic-pearlitic counterparts as starting materials [C5]. Ganeev, Karavaeva et al. investigated the deformation of martensitic 0.1 wt.-% C and 0.45 wt.-% C steels using HPT [C6-C8]. A hardness increase as compared to the as-quenched state and an ultimate tensile strength of 2.65 GPa was reported for 0.45 wt.-% C martensitic carbon steel after HPT deformation at 350 °C [C6-C8]. The effect of various deformation temperatures was only investigated in one of the studies and resulted in a maximum hardness of a 0.45 wt.-% C martensitic steel for a deformation temperature of 350 °C in the investigated temperature range from 300 °C to 450 °C [C5]. In the other studies mentioned above, only one operating temperature was applied without sufficient justification.

In the present study, heat treatments and HPT were combined for a martensitic low carbon steel in all three sequences as described above. The obtained microstructures and mechanical properties are discussed with respect to the influence of previous HPT processing on the annealing behavior, the different effects of static and dynamic recovery and recrystallization and the similarities and differences of the structures obtained from the three processing sequences.

C.2. Experimental Details

Ck10 plain carbon steel (DIN 17210) was annealed for 15 minutes at 1000 °C and subsequently quenched to room temperature in salt water. The oxide layer of the disk-shaped samples was removed from the top and bottom surface, resulting in a final thickness of about 0.8 mm. The diameter of the disks was 8 mm. The specimens were deformed in a HPT device by one revolution either at room temperature or at elevated temperatures using inductive heating of the

anvils. Both the hydrostatic pressure and the rotational speed were kept constant at 7.3 GPa and 0.2 rpm, respectively. The samples for subsequent processing were heat-treated isothermally either before grinding or after the HPT treatment for 10 or 60 minutes in air. Heat treatments at eight different temperatures between 100 °C and 450 °C were investigated.

The microstructures were imaged using a field emission scanning electron microscope (SEM) Zeiss LEO 1525 with a back-scattered electron detector. The micrographs shown in this paper were recorded in tangential direction at a radius of r = 3mm (ε_{vM} = 15). Hardness testing was performed on the cross-sections of the HPT disks using a Buehler Micromet 5104 microhardness tester with a load of 0.5 kg (HV 0.5).

Additional characterization using differential scanning calorimetry (DSC) and in-situ x-ray diffraction (XRD) was performed during heating of an as-quenched sample and a sample after HPT deformation at room temperature. DSC measurements were performed in two cycles between 100 °C and 1000 °C with a heating and cooling rate of 20 K min^{-1} in argon atmosphere using a Netzsch DSC 404 F1 Pegasus device. In-situ XRD was performed in transmission with a photon energy of 100 keV and a beam size of 0.32 x 0.32 mm² at the P07 HEMS beamline at the synchrotron PETRA III (Hamburg, Germany) [C9]. A DIL 805A/D dilatometer by TA Instruments, specially modified for such transmission measurements, was used for these experiments heating from room temperature up into the two-phase region of ferrite and austenite with a heating rate of 10 K min^{-1} in argon atmosphere [C10]. The 2D diffraction patterns were integrated using the software package Fit2D [C11].

C.3. Results

C.3.1. Effect of Deformation Temperature
on Microstructure and Hardness

The microstructures obtained after one revolution HPT at different temperatures are shown in Figure C1. At room temperature, a nanocrystalline structure with strongly elongated grains is obtained (Figure 1a). The grain size decreases with increasing equivalent strain, and equals about 30 m in the axial direction at a radius of r = 3 mm (ε_{vM} = 15). The microhardness increases correspondingly from the center towards the edge of the HPT disk (Figure C2a). The decreasing slope with increasing distance from the disk center implies a decrease of the hardening rate with increasing stain.

At a deformation temperature of 200 °C, a moderate increase in grain size, but the same principal structure as at room temperature is observed (Figure C1b). Analysis of several SEM micrographs
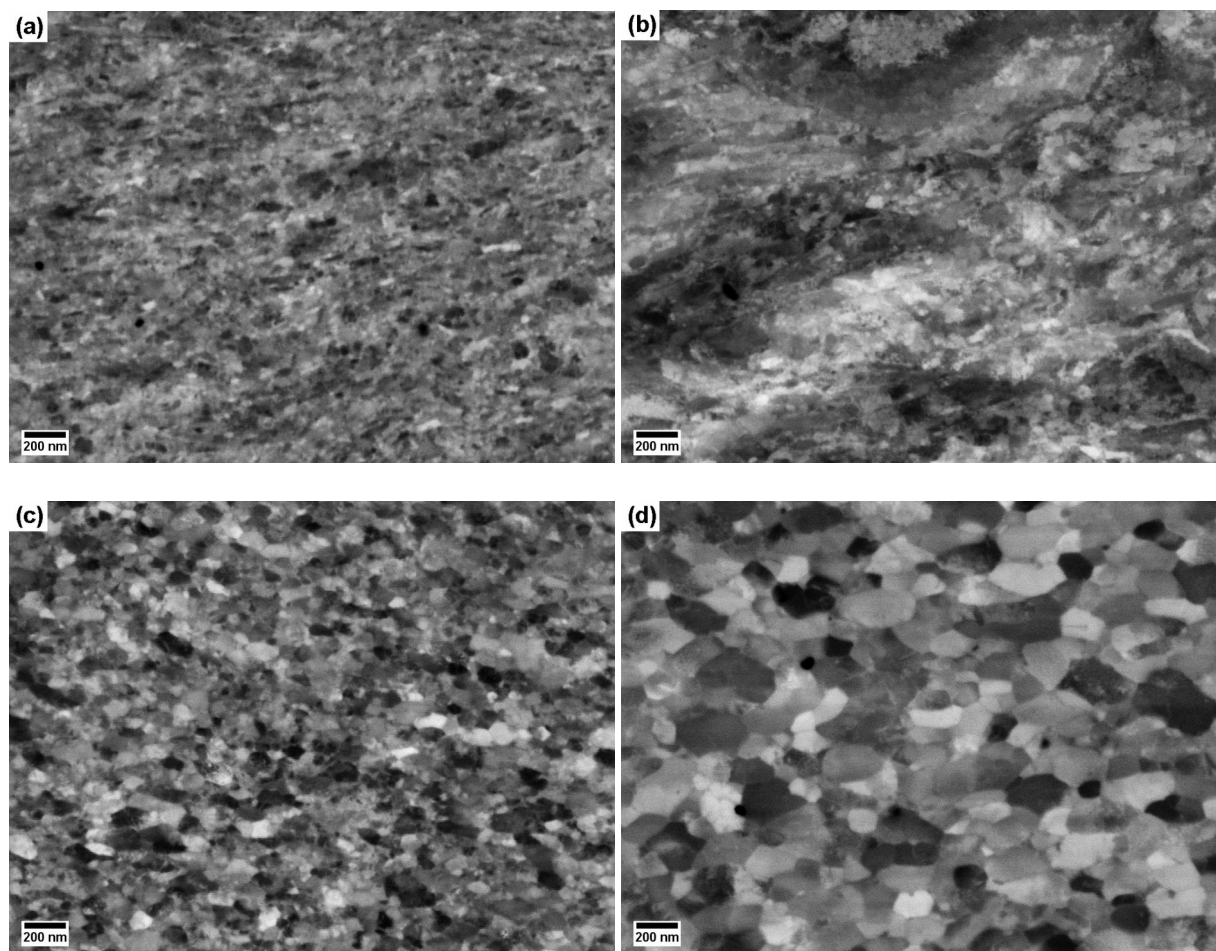
Figure C1: SEM micrographs after HPT at (a) room temperature, (b) 200 °C, (c) 350 °C and (d) 450 °C at radius r = 3 mm (1 revolution, ε_{vM} = 15).

indicates a slight increase of regions, where the elongated grains are not aligned perfectly in the shear plane. The hardness decreases and the hardening rate becomes approximately independent of the radius in this temperature regime up to 200 °C (Figure C2a).
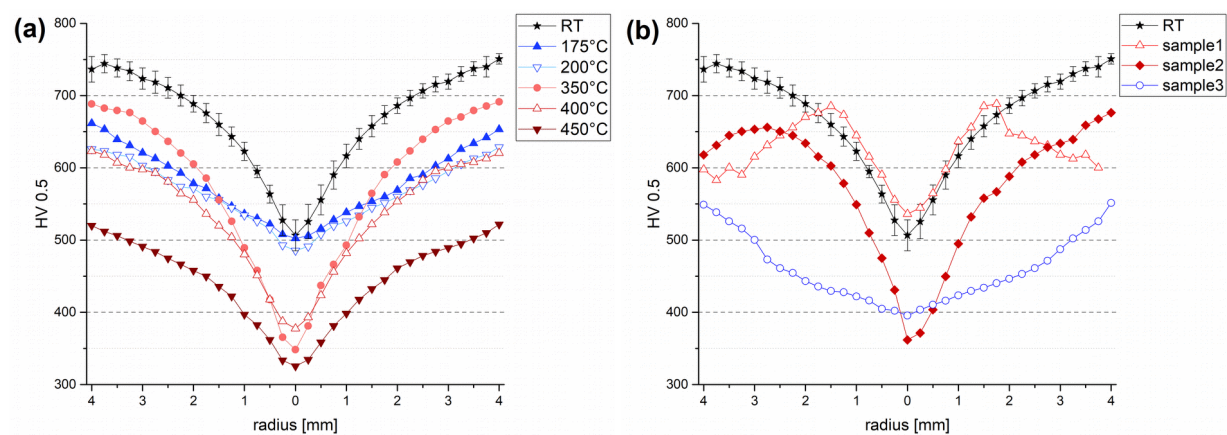

Figure C2: Microhardness profiles after HPT processing (1 revolution) at room temperature or at elevated temperatures (a) in the stable temperature range and (b) at 300 °C (unstable temperature range).

A completely different microstructure with more equi-axed grains is obtained at 350 °C (Figure C1c). The grain size decreases from about 80 nm at $r = 1$ mm ($\varepsilon_{vM} = 5$) to about 60 nm at $r = 3$ mm ($\varepsilon_{vM} = 15$). The hardness in the center of the HPT disk ($\varepsilon_{v,M} = 0$) is significantly lower than for the lower deformation temperatures. However, it is higher than for the lower-annealed samples and only about 50 HV below the room temperature sample near the edge (Figure C2a). Further increase of the deformation temperature results in an increase of the equi-axed grain size up to about 150 nm at radius $r = 3$ mm for a deformation temperature of 450 °C (Figure C1d). This grain size increase is accompanied by a drop of the hardness as compared to the 350 °C sample (Figure C2a).

Strongly inhomogeneous and not well reproducible behavior occurs for HPT at 250 °C or 300 °C. Various microstructures are found in different samples after processing under identical conditions as well as within one sample. Some regions resemble the as-quenched structure, whereas others are more similar to the structures described for 200 °C or 350 °C. This also results in strong variations in the hardness profiles, ranging from the profiles measured for 200 °C and 350 °C to non-monotonous hardness evolutions (Figure C2b).

C.3.2. Microstructure and Hardness
after Tempering and Subsequent SPD

Tempering of the as-quenched martensite results in an approximately constant hardness up to 200 °C followed by a hardness decrease at higher temperatures which is more pronounced for 60 minutes than for 10 minutes tempering (Figure C3a). This evolution of hardness is directly transferred to the hardness profiles after subsequent HPT processing (Figure C3b). For the 200 °C sample even a slight hardness increase as compared to the as-quenched samples can be seen, but only within the magnitude of scatter between different samples. The microstructure for all
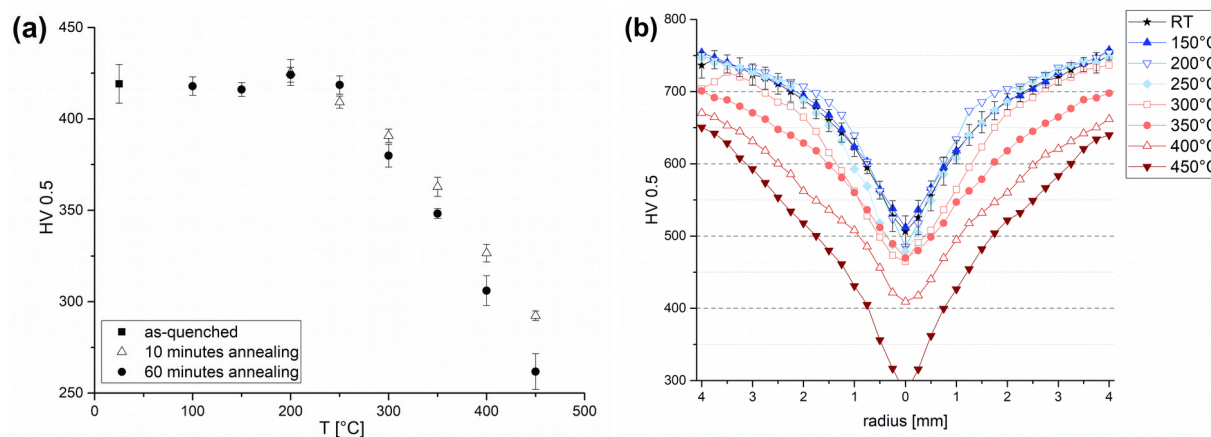

Figure C3: (a) Microhardness of as-quenched martensite after isothermal tempering.
(b) Microhardness profiles after isothermal tempering for 60 minutes and
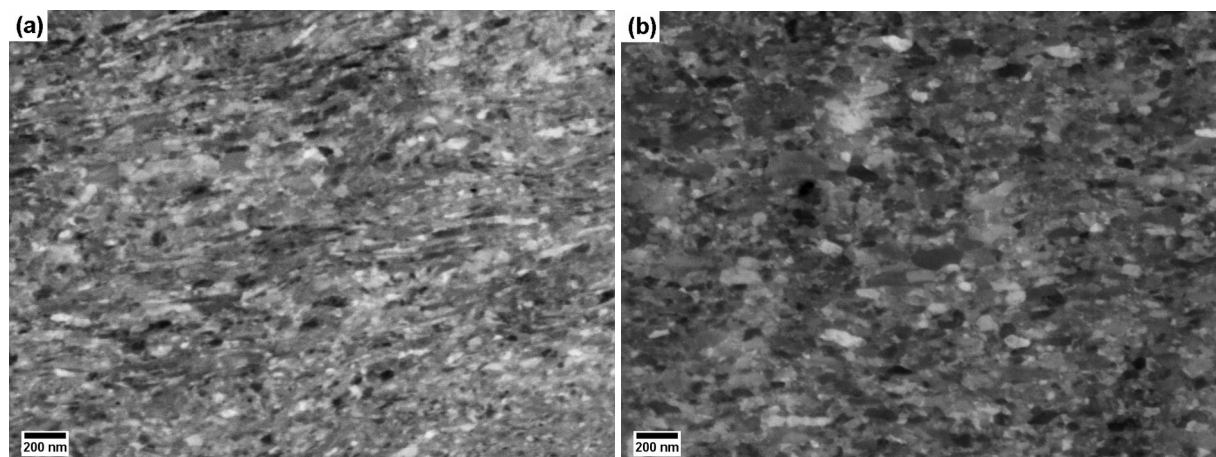**subsequent HPT at room temperature (1 revolution).**

Figure C4: Microstructures after 60 minutes tempering at (a) 200 °C and (b) 450 °C and subsequent HPT deformation (r = 3 mm, 1 revolution, ε_{vM} = 15).

tempered samples consists of elongated grains with an increase of grain size with increasing tempering temperature. Examples for 200 °C and 450 °C are shown in Figure C4. Even for the sample tempered at 450 °C for 60 minutes, the grain size is below 100 nm after an equivalent strain of ε_{vM} = 5 (r = 1 mm) or more.

C.3.3. Annealing after SPD at Room Temperature

C.3.3.1. Microstructures and Microhardness after Isothermal Annealing

Figure C5 shows the microhardness of the HPT-processed martensite after subsequent isothermal annealing for 10 or 60 minutes, respectively. A slight hardness increase for the 200 °C sample, similar to that described in the previous section for the previously tempered sample, is observed. The hardness drop with increasing temperature is shifted towards higher temperatures as compared to the previously tempered samples: For the 350 °C the decrease is restricted to a small part of the sample after 60 minutes annealing (Figure C5b), whereas a significant decrease in hardness is only observed for 400 °C and above. For these high temperatures, the hardness reduction upon annealing is more pronounced in the higher strained regions of the samples, resulting in an almost constant hardness distribution over the whole cross-section of the disk after 60 minutes at 450 °C. This homogeneous hardness value is significantly higher than for the as-quenched sample tempered under the same conditions (Figure C3a). The corresponding microstructural investigations reveal that the small hardness reduction up to 350 °C is based on a moderate increase in grain size retaining the elongated grain shape of the as-deformed structure (Figures C6a+b). On the contrary, the lower hardness of the samples annealed at higher temperatures is caused by a recrystallized structure with approximately equi-axed grains (Figures C6c+d).
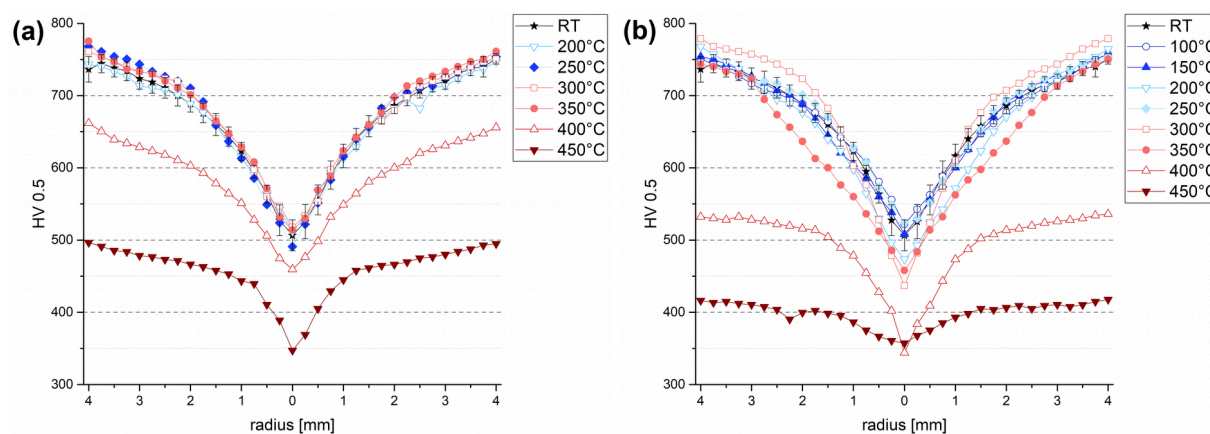
Figure C5: Microhardness profiles after annealing of HPT-treated martensite (1 revolution) for (a) 10 and (b) 60 minutes.
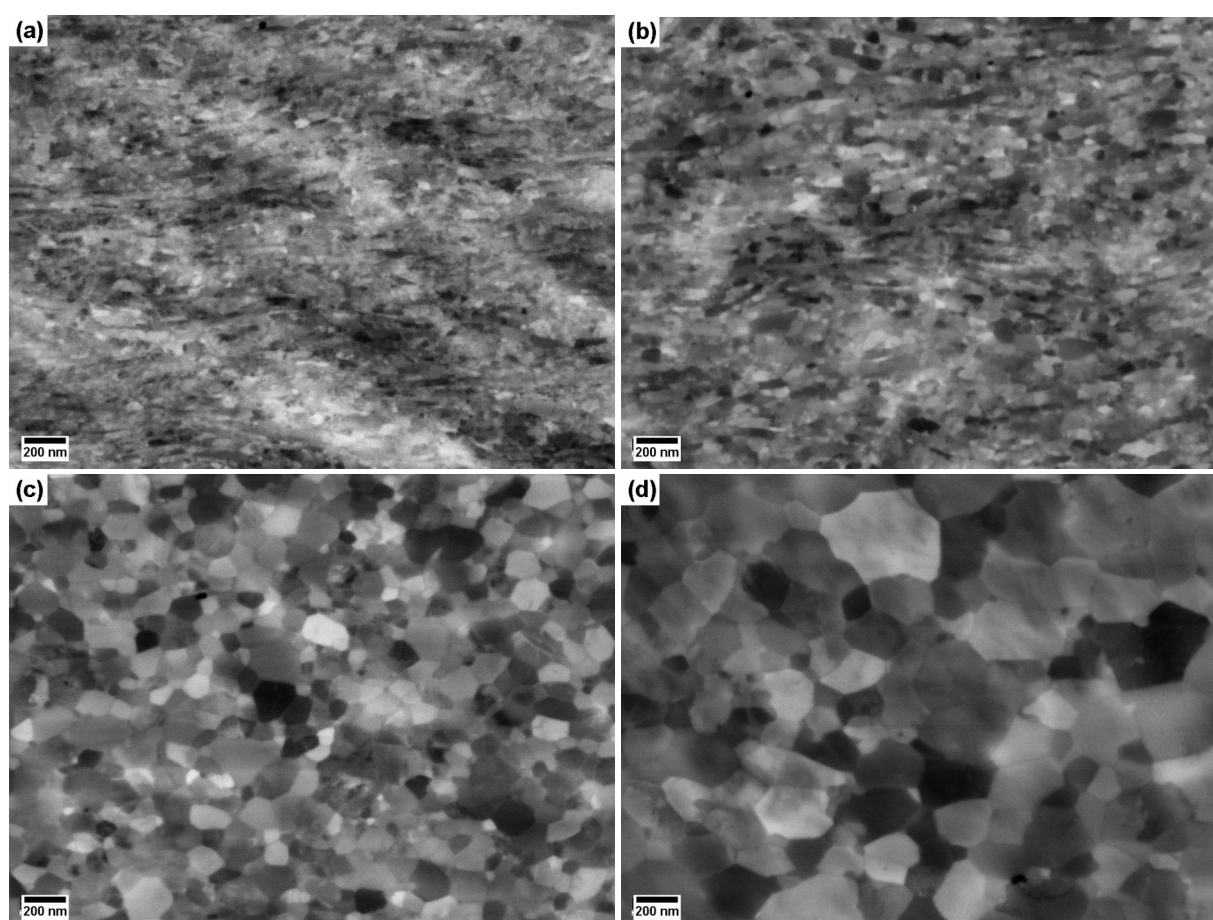

Figure C6: Microstructures after annealing of HPT-treated martensite for 60 minutes at (a) 200 °C, (b) 350 °C, (c) 400 °C and (d) 450 °C ($r = 3$ mm, 1 revolution, $\varepsilon_{vM} = 15$).

C.3.3.2. DSC

The DSC curves of both the as-quenched and the HPT-treated sample show three exothermic peaks accompanied by the magnetic transition at about 870 °C (Figure C7). The first peak only arises in the first heating cycle for both samples. The HPT processing results in a significant broadening, a shift towards lower temperatures and an intensity increase from 1.6 J/g to 3.6 J/g for this peak. The strong peak with an onset temperature of about 740 °C refers to the A_1

transformation. Its area is also increased after HPT as compared to the as-quenched state and is even lower for the second heating cycle of both samples (Table C1). Both the onset and the peak temperature have exactly the opposite order, i.e. the lowest values are obtained after HPT followed by the as-quenched sample and the second cycles. The final peak at 919 °C is a result of the A_3 transformation and does not show any significant temperature shifts among the different measurements. However, its intensity is substantially lower after HPT processing and much higher in the second cycle for both samples (Figure C7).
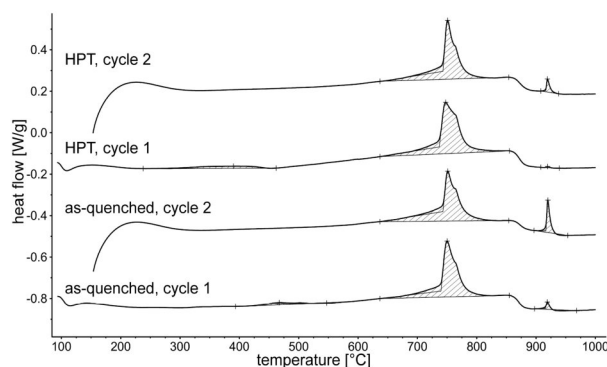

Figure C7: DSC curves of as-quenched and HPT-treated martensite (1 revolution at room temperature).

Table C1: Integrated intensities, I, onset temperatures, T_{on}, and peak temperatures, T_p, of the A_1 peak in the DSC measurements.

sample	cycle	I [J/g]	T_{on} [°C]	T_p [°C]
as-quenched	1	27.37	739.7	750.1
	2	26.63	743.1	751.3
after HPT	1	30.78	736.9	747.8
	2	26.12	743.0	750.9

C.3.3.3. In-Situ XRD during Annealing

The in-situ diffraction experiments show the formation of cementite starting at about 400 °C and austenite at 725 °C for both the as-quenched and the HPT-processed material (Figure C8a+b). Furthermore, a decrease of peak width with increasing temperature occurs in both cases and is more pronounced in the deformed sample. Closer examination shows that the Bragg peaks of the cementite can be found starting from about 320 °C in the as-quenched state, whereas HPT shifts their first appearance to about 420 °C (Figure C8c+d). The formation of intermediate carbides prior to the cementite formation is not observed in this study, as expected for the low carbon steel under investigation [C12].
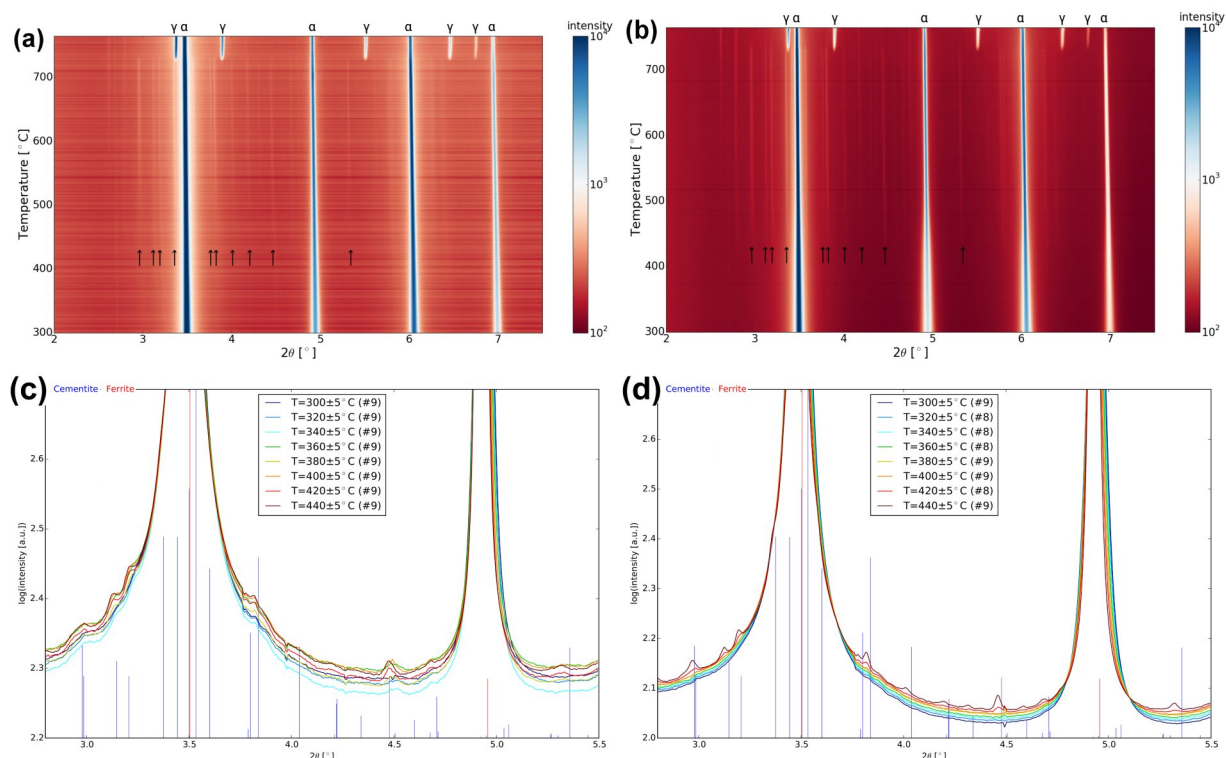
Figure C8: (a-b) Color maps showing the evolution of the diffraction patterns as a function of temperature during heating at the in-situ XRD experiments with (a) an as-quenched and (b) a HPT-treated sample (1 revolution at room temperature). The Bragg peaks of ferrite and austenite are indicated as α and γ, respectively. The arrows indicate some characteristic peaks of the cementite phase. (c-d) Parts of the integrated XRD patterns of (c) as-quenched martensite and (d) HPT-deformed martensite. In the legend, the number in brackets indicates the number of XRD measurements in the given temperature ranges, which were averaged to obtain better counting statistics for the plotted patterns. The blue and red lines show the theoretical peak positions of cementite (Space group Pnma, a = 5.0849 Å, b = 6.7363 Å, c = 4.514 Å) and ferrite (Space group Im-3m, a = 2.8665 Å), respectively. The shifts of the measured peak positions are due to the thermal expansion at the elevated measuring temperatures.

C.4. Discussion

The results show that a wide range of different structures can be obtained from the three processing routes and that the temperature, at which a significant change of microstructure and hardness sets in, depends on the processing sequence. In the following, the formation of the different structures is discussed with respect to the corresponding atomistic processes.

C.4.1. Influence of Severe Plastic Deformation on Annealing Behavior of Martensite

The DSC and in-situ XRD results as well as the microstructures after isothermal heat treatments clearly show that SPD has impact on the thermal stability of the low carbon steel martensite. The first processes upon heating, which are influenced by previous SPD, are recovery and

recrystallization. The heat release from massive structural coarsening or recrystallization results in the first exothermic peak of the DSC measurements. Although located in the same temperature range, this peak is not caused by the precipitation of cementite since the in-situ XRD data shows an opposite temperature shift for this process after SPD and it is well-known that the formation of cementite implies only a very small heat release even for steels with higher carbon contents [C13]. The decreased recrystallization temperature, as indicated by the DSC peak, is confirmed by the microstructural investigations, which show that 400 °C annealing is sufficient to obtain a recrystallized structure after HPT processing (Figure C6). On the contrary, significant growth of the laths takes place at around 450 °C for the undeformed martensite, although a moderate increase of the lath size causes a drop in microhardness already at lower temperatures (Figure C3a). The HPT processing results in an enhanced dislocation density and a reduction of grain size. This additional energy of the deformed structure results in a larger energy release during recrystallization, i.e. a larger peak area in DSC. Furthermore, the heavily deformed structure both facilitates nucleation processes and promotes a higher driving force for recrystallization, which results in the shift of this process towards lower temperatures. This observation is in agreement with the analogous shift of recrystallization temperature reported for a 0.05 wt.-% C (non-martensitic) steel after SPD and a 0.2 wt.-% C martensite after rolling [C14, C15]. The large variation of plastic strain from the center to the edge of a HPT disk is a possible explanation for the large broadening of the DSC peak.

SPD not only affects the recrystallization temperature, but also the grain shape of the recrystallized structures. The formation of equi-axed recrystallized grains is facilitated after SPD, whereas the grain shape of the undeformed martensite is elongated even after annealing at 600 °C, i.e. a complete reconstruction of the microstructure or recrystallization according to a common understanding does not take place (Figure C9). This was already reported for conventional cold-rolling and was attributed to the stabilization of lath boundaries by carbide precipitates for the as-quenched structure [C15].
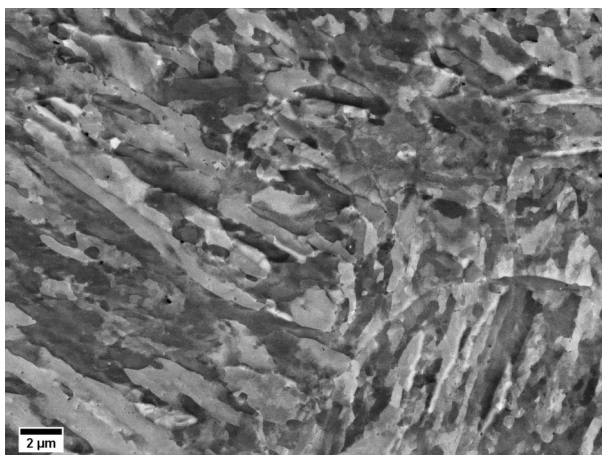
Figure C9: Microstructure of the as-quenched martensite after tempering for 60 minutes at 600°C.

Indeed, the formation of cementite falls within the same temperature range as the recrystallization and is shifted towards higher temperatures by SPD according to the in-situ XRD experiments. To explain this phenomenon, the distribution of carbon in the martensitic structures has to be considered. Due to the high martensite start temperature of low carbon steels, autotempering results in carbide precipitation and carbon segregation already during quenching [C16, C17]. Furthermore, carbon can easily diffuse in these structures even at room temperature [C12, C16]. Thus, only small amounts of carbon occupy interstitial sites in the crystals of the as-quenched martensite, whereas the majority of carbon atoms is located at defects sites and particularly at interfaces such as lath boundaries [C12, C16, C17]. When subjected to SPD, the number of defects increases dramatically [C18]. Furthermore, (partial) dissolution of the carbide precipitates might take place, which is subject of ongoing research. The increase of the number of segregation sites during deformation and the high diffusivity implies a reduced carbon concentration (per unit area) at the grain boundaries. On the one hand, this facilitates grain boundary motion promoting the reduction of the recrystallization temperature as discussed previously. On the other hand, the precipitation of cementite is affected. Whereas the larger number of potential nucleation sites generally facilitates precipitation, the reduced carbon concentration at the interfaces has the opposite effect. More material transport via diffusion and the formation of larger concentration gradients along energetically similar boundary sites are necessary in order to reach a sufficient local carbon concentration for the formation of cementite. This seems to outbalance the effect of the larger number of nucleation sites, resulting in the observed increase of the precipitation temperature. The argument even holds if recrystallization takes place simultaneously due to the reduced grain size in the recrystallized structure after previous SPD. However, part of the apparent temperature shift by 100 K according to the in-situ XRD data may be caused by the restrictions of the measurement technique itself. Due to the wider shoulders of adjacent peaks for the more distorted structure after SPD, Bragg peaks originating from small cementite precipitates may become visible only after reaching a larger volume fraction of the cementite phase as

compared to the case of the coarser-grained as-quenched counterpart. Still, the whole temperature shift is unlikely to be caused by this measurement artifact since the differences in peak width are not that pronounced (Figure C8c+d). The formation of cementite prior to recrystallization stabilizes the elongated grain shape in the as-quenched martensite, whereas the obstructed precipitation after SPD enables the formation of an equi-axed structure.

Finally, DSC shows the impact of the HPT treatment on the austenitization process. For the A_1 transformation, the long-known temperature decrease for the martensitic starting material as compared to the near-equilibrium structure (i.e. the structure in the second heating cycle) is obtained and is accompanied by a slight increase in heat release [C19]. The additional decrease of the transformation temperature and increase of the heat release for the HPT-treated material is caused by the even finer structure in this case. The smaller size of both recrystallized ferrite and cementite precipitates due to the larger number of nucleation sites gives rise to the enhanced heat release because of the larger interface area that is absorbed by the moving phase boundaries during the growth of austenitic grains. The shift of the A_1 transformation temperature in the DSC as compared to the almost constant temperature in in-situ XRD can be attributed to the higher heating rate in the DSC experiments [C19]. The last peak of the DSC measurements corresponds to the A_3 transformation, i.e. the formation of austenite out of ferrite that has not transformed already in the two-phase region due to kinetical reasons at the high heating rate. The finer the structure, the easier the transformation from ferrite to austenite during heating in the two-phase region. Thus, the A_3 transformation peak is almost invisible in the HPT-treated sample, clearly measurable for the as-quenched state and significantly increased in the second cycles (Figure C7).

Overall, it is shown that SPD affects not only recrystallization and cementite precipitation, but even austenitization of the already recrystallized microstructures. The large temperature shifts in opposite directions shift the cementite formation above the recrystallization temperature which makes it possible to produce ultrafine-grained recrystallized microstructures with carbon-enriched grain boundaries.

C.4.2. Dynamic vs. Static Recovery and Recrystallization

Whereas the materials exposed to elevated temperatures before or after SPD are thermally stable up to a certain temperature, which is reflected in the hardness plots (Figures C3 and C5), any temperature rise during HPT has strong impact on the hardness of the material after processing (Figure C2). This difference is well-founded on the different atomistic processes of these processing routes, which are static recovery and recrystallization in the former cases and dynamic recovery and recrystallization in the latter.

Generally, the strength of martensitic steels is mainly based on dislocation and grain boundary strengthening [C16, C20]. Due to autotempering and the fast diffusion of carbon already at room temperature, the strong impact of the carbon content on the strength is not due to solid solution strengthening, but mainly due to the stabilization of dislocations and interfaces [C16]. When the as-quenched martensitic steel is heated, first the diffusion of carbon is further accelerated, then recovery results in the annihilation of point defects as well as the rearrangement and partial annihilation of dislocations and finally interfaces are mobilized triggering massive coarsening and carbide precipitation [C12]. However, dislocation movement and the mobilization of interfaces are strongly inhibited due to the carbon segregation [C15]. Therefore, no significant change in hardness is obtained in the lower temperature regime (Figure C3a). Although recovery and recrystallization are facilitated after SPD, this argumentation holds until a certain temperature. Only when the interfaces become mobile and recrystallization takes place, a drop in hardness is obtained as can be seen in Figure C5 for 400 and 450 °C.

On the very contrary, the dynamic recovery during SPD influences the resulting structures and its hardness already at much lower temperatures (Figure C2a). During SPD at room temperature, the activation of dislocation sources results in a strong increase of dislocation density, the arrangement of dislocations in small-angular grain boundaries and the subsequent increase of the misorientation, leading to the transfer to high-angle grain boundaries [C18]. Dynamic recovery, even at moderate deformation temperatures, results in larger grains after deformation because the absorption of mobile dislocations in interfaces is facilitated and the nucleation rate of new dislocations is reduced due to the enhanced mobility of already existing dislocations. Thus, the whole process of grain refinement during SPD is inhibited already at moderately elevated temperatures. This leads to a larger grain size and reduced hardness with increasing temperature even in the low-temperature regime, where the movement of existing, segregation-stabilized dislocations and interfaces is not significant. Briefly, static recovery has only limited influence on the hardness evolution upon heat treatments in contrast to the strong impact of dynamic recovery.

At higher temperature, grain coarsening and softening occur in both cases due to static or dynamic recrystallization. However, a significant difference concerning the homogeneity of the microstructure is evident in this temperature regime. Static recrystallization always results in a homogeneous coarsening leading to a monotonous distribution of hardness as a function of strain. On the contrary, dynamic recrystallization causes inhomogeneity and non-reproducibility for HPT at 250 °C and 300 °C. The local softening due to the onset of dynamic recrystallization under the simultaneous application of torsional forces initiates the localization of deformation resulting in inhomogeneous samples after HPT. The stochastic components of both the onset of recrystallization and the distribution of energetically favored, highly distorted regions make this

localization unreproducible, which leads to the large variety of different microstructures obtained for these deformation temperatures. Only if the recrystallization spreads over large areas before the shear localization sets in, homogeneous structures are obtained, as is the case at 350 °C and above.

C.4.3. Structural Variety Obtainable by Different Sequences of Heat Treatments and HPT

The three processing routes result in a large range of structures that were shown in Section 3. Each processing route is the origin of certain structures that cannot be obtained by any of the other routes. SPD at room temperature after previous tempering is the only method to obtain a two-phase microstructure of ferrite and cementite with elongated grains and thus anisotropic properties. A similar microstructure may be obtainable by room temperature SPD of bainitic steel [C21]. However, the tempered martensite after SPD is expected to have the higher strength due to the more homogeneous microstructure in the beginning.

The annealing after SPD at room temperature is the best way to produce structures with maximum strength and a certain thermal stability up to temperatures of 300 °C. According to our findings, no significant structural changes take place in these materials from 10 to 60 minutes annealing. Thus, we expect them to be stabilized in this temperature range.

Finally, the HPT processing at elevated temperature is the method of choice to obtain equi-axed grains with minimum grain size resulting in the maximum hardness of an isotropic microstructure.

In summary, all processing routes are of interest to produce steels with certain microstructures. Knowledge of each of the processing sequences is necessary in order to find the optimum route for processing materials with tailored properties and structure. The results show the diversity of structures that can be obtained by the combination of SPD with phase transformations, but also the vast number of processing parameters implied by this combination.

C.5. Conclusions

It was shown that a huge variety of microstructures can be obtained by different combinations of SPD and heat treatments of a martensitic low carbon steel. This is based on the differences of dynamic and static recovery and recrystallization (or grain growth) as well as the impact of SPD on the thermal stability of martensite. SPD lowers the recrystallization and the austenitization temperatures whereas the formation of cementite is retarded upon heating. These

interdependencies of SPD and atomistic processes at elevated temperatures open up an enormous space to tailor microstructures and properties of nanostructured high-strength steels.

Acknowledgments

References

C1   N. Tsuji, T. Maki, Enhanced structural refinement by combining phase transformation and plastic deformation in steels, Scr. Mater. 60 (2009), 1044-1049. http://dx.doi.org/10.1016/j.scriptamat.2009.02.028

C2   N. Tsuji, New Routes for Fabricating Ultrafine-grained microstructures in bulky steels without very high strains, Adv. Eng. Mater. 12 (2010), 701-707. http://dx.doi.org/10.1002/adem.201000018

C3   N. Tsuji, R. Ueji, Y. Minamino, Y. Saito, A new and simple process to obtain nano-structured bulk low-carbon steel with superior mechanical property, Scr. Mater. 46 (2002), 305-310. http://dx.doi.org/10.1016/S1359-6462(01)01243-X

C4   M.V. Karavaeva, M.A. Nikitina, A.V. Ganeev, R.K. Islamgaliev, High-strength state of ultrafine-grained martensitic steel produced by high pressure torsion, IOP Conf. Ser.: Mater. Sci. Eng. 179 (2017), 012037. http://dx.doi.org/10.1088/1757-899X/179/1/012037

C5   S. Dobatkin, J. Zrnik, I. Mamuzic, Utrafine-grained low carbon steels by severe plastic deformation, Metalurgija (Zagreb, Croatia) 47 (2008), 181-186.

C6   A.V. Ganeev, M.V. Karavaeva, X. Sauvage, E. Courtios-Manara,   Y. Ivanisenko, R.Z. Valiev, On the nature of high-strength state of carbon steel produced by severe plastic deformation, IOP Conf. Ser.: Mater. Sci. Eng. 63 (2014), 012128. http://dx.doi.org/10.1088/1757-899X/63/1/012128

C7   M.V. Karavaeva, S.K. Kiseleva, A.V. Ganeev, E.O. Protasova, M.M. Ganiev, L.A. Simonova, R.Z. Valiev, Superior strength of carbon steel with an ultrafine-grained microstructure and its enhanced thermal stability, J. Mater. Sci. 50 (2015), 6730-6738. http://dx.doi.org/10.1007/s10853-015-9227-2

C8   M.V. Karavaeva, S.K. Nurieva, N.G. Zaripov, A.V. Ganeev, R.Z. Valiev, Microstructure and mechanical properties of medium-carbon steel subjected to severe plastic deformation, Met. Sci. Heat Treat. 54 (2012), 155-159. http://dx.doi.org/10.1007/s11041-012-9473-8

C9   N. Schell, A. King, F. Beckmann, T. Fischer, M. Müller, A. Schreyer, The High Energy Materials Science Beamline (HEMS) at PETRA III, Mater. Sci. Forum 772 (2014), 57-61. http://dx.doi.org/10.4028/www.scientific.net/MSF.772.57

C10 P. Staron, T. Fischer, T. Lippmann, A. Stark, S. Daneshpour, D. Schnubel, E. Uhlmann, R. Gerstenberger, B. Camin, W. Reimers, E. Eidenberger, H. Clemens, N. Huber, A. Schreyer, In situ experiments with synchrotron high-energy X-rays and neutrons, Adv. Eng. Mater. 13 (2011), 658-663. http://dx.doi.org/10.1002/adem.201000297

C11 A.P. Hammersley, S.O. Svensson, M. Hanfland, A.N. Fitch, D. Häusermann, Two-dimensional detector software: From real detector to idealised image or two-theta scan, High Pressure Res. 14 (1996), 235-248. http://dx.doi.org/10.1080/08957959608201408

C12 D. Kalish, E.M. Roberts, On the Distribution of Carbon in Martensite, Metall. Trans. 2 (1971), 2783-2790. http://dx.doi.org/10.1007/BF02813252

C13 P.V. Morra, A.J. Böttger, E.J. Mittemeijer, Decomposition of iron-based martensite: A kinetic analysis by means of differential scanning calorimetry and dilatometry, J. Therm. Anal. Calorim. 64 (2001), 905-914. http://dx.doi.org/10.1023/A:1011514727891

C14 F. Khodabakhshi, M. Kazeminezhad, Differential scanning calorimetry study of constrained groove pressed low carbon steel: recovery, recrystallisation and ferrite to austenite phase transformation Mater. Sci. Technol. 30 (2014), 765-773. http://dx.doi.org/10.1179/1743284713Y.0000000388

C15 S. Takaki, S. Iizuka, K. Tomimura, Y. Tokunaga, Influence of cold working on recovery and recrystallization of lath martensite in 0.2%C steel, Mater. Trans., JIM 33 (1992), 577-584. http://dx.doi.org/10.2320/matertrans1989.33.577

C16 G. Krauss, Martensite in steel: strength and structure, Mater. Sci. Eng. A 273-275 (1999), 40-57. http://dx.doi.org/10.1016/S0921-5093(99)00288-9

C17 B. Hutchinson, J. Hagström, O. Karlsson, D. Lindell, M. Tornberg, F. Lindberg, M. Thuvander, Microstructures and hardness of as-quenched martensites (0.1–0.5%C), Acta Mater. 59 (2011), 5845-5858. http://dx.doi.org/10.1016/j.actamat.2011.05.061

C18 R. Pippan, F. Wetscher, M. Hafok, A. Vorhauer, I. Sabirov, The limits of refinement by severe plastic deformation, Adv. Eng. Mater. 8 (2006), 1046-1056. http://dx.doi.org/10.1002/adem.200600133

C19 N.C. Law, D.V. Edmonds, The Formation of Austenite in a Low-Alloy Steel, Metall. Trans. A 11 (1980), 33-46. http://dx.doi.org/10.1007/BF02700436

C20 T. Ohmura, K. Tsuzaki, S. Matsuoka, Nanohardness measurements of high-purity Fe-C martensite, Scr. Mater. 45 (2001), 889-894. http://dx.doi.org/10.1016/S1359-6462(01)01121-6

C21 F. Wetscher, B. Tian, R. Stock, R. Pippan, High pressure torsion of rail steels, Mater. Sci. Forum 503-504 (2006), 455-460. http://dx.doi.org/10.4028/www.scientific.net/MSF.503-504.455

Publication D

Electrodeposition of Fe-C Alloys from Citrate Baths: Structure, Mechanical Properties and Thermal Stability

Timo Müller, Joseph Grimwood, Andrea Bachmaier and Reinhard Pippan

Erich Schmid Institute of Materials Science, Austrian Academy of Sciences, Leoben, Austria

Abstract

A new citrate-based electrolyte is suggested for the electrodeposition of thick Fe-C films. The structure and properties of the deposits are compared to those from another electrolyte previously reported in literature. Both consist of a nanocrystalline single-phase structure with a grain size of 20 nm, which results in a hardness of up to 660 HV. Due to its higher growth rate, the new electrolyte is a promising candidate for the deposition of thick film. However, the codeposition of oxygen causes embrittlement, limiting the application of the deposits from both the new and the known electrolyte. On the other hand, the codeposited carbon and oxygen provide considerable thermal stability and even a hardening capacity upon annealing. The results are compared and discussed with respect to the previous investigations of electrodeposited Fe-C alloys.

D.1. Introduction

The binary Fe-C system and carbon steels in general are among the most investigated materials since they are widely used for engineering applications and account for the lion's share of the global steel production. On the other hand, research on electrochemical deposition has grown rapidly during the last decades due to its industrial applications. Whereas electroplating of carbon steel parts with films made of other materials has been investigated in depth and is widely used in industrial applications, the use of Fe-C alloys as a coating material is rarely considered. The electrodeposition of Fe-C alloys has been studied only in a very limited number of investigations and will be reviewed in the following.

The codeposition of carbon with iron was already reported in the 1950s by Petrov [D1]. He observed 0.4-0.7 wt.-% C in Fe deposits from a chloride bath containing glycerol and sugar,

resulting in a high hardness of the deposits [D1]. However, this phenomenon was not further investigated, until it was rediscovered by Izaki et al. in 1989 [D2]. They found that the addition of citric acid and ascorbic acid to an iron sulfate bath enables the deposition of thick fine-grained layers incorporating about 1 wt.-% C which results in a hardness of 800 HV [D2]. The deposits were shown to consist of a single-phase supersaturated solid solution with a body-centered tetragonal (bct) crystal structure and elongated grains of about 20 nm in width [D3, D4]. The carbon content – and, thus, hardness and tetragonal distortion – can be varied via the applied current density during deposition [D4, D5]. Upon annealing, decomposition of the supersaturated solid solution takes place via the formation of an intermediate carbide and cementite [D5]. This decomposition is accompanied by a hardening effect up to 350 °C for deposits with high carbon contents [D5]. These findings were confirmed by the work by Haseeb et al. [D6] who investigated the decomposition upon annealing in more detail [D7, D8].

Oh et al. showed that pulse plating has only little effect on the structure and hardness of electrodeposited Fe-C alloys [D9]. Nevertheless, ductility of the pulsed deposits is improved according to their findings investigating the surroundings of Vickers microindents [D9].

Almost all studies on electrodeposition of Fe-C alloys use citric acid and / or ascorbic acid in the electrolyte in order to codeposit carbon. However, Fujiwara et al. showed that other hydroxycarboxylic and polycarboxylic acids are also suitable for the electrodeposition of Fe-C alloys [D10, D11]. Furthermore, they investigated the effect of other bath components [D12].

Finally, the electrodeposition of ternary alloys including Fe-C has been studied. However, these investigations are restricted to the addition of another element of the iron group (nickel [D7] or cobalt [D13]) and the elements phosphorous and boron [D14, D15]. The codeposition of hydrogen is inherent to the electrodeposition of iron and its alloys in general [D16], but was shown to be significantly enhanced in the case of Fe-C alloy deposition [D17].

In spite of these previous studies, many questions on the formation and properties of electrodeposited Fe-C alloys are still unsolved or even uninvestigated. For example, the exact mechanism of carbon co-deposition is still unclear, the distribution of carbon in the strongly supersaturated, nanostructured deposits has not been investigated and – despite the enormous hardness of the deposits – further investigations on the mechanical properties have been restricted to wear tests by Miyamoto et al. on Fe-C-P deposits [D15]. In this work, a new citrate bath for the deposition of thick Fe-C layers is proposed and the structure of the deposits is investigated both in the as-quenched and annealed state. Besides indentation, compression and bending tests are used to get further insights into the mechanical properties of these materials.

D.2. Materials and Methods

Electrodeposition was performed under constant current density using a computer-controlled IPS PGU10V-2A-OEM-MI potentiostat. A double-walled glass cell connected to a circulation thermostat was used to control the temperature during the experiments. The pH of the bath was measured before and after the experiment. Most samples were deposited under one of the following three conditions: from the new citrate bath at 65 °C with -50 mA/cm², from the same electrolyte at 50 °C with -30 mA/cm² or from the electrolyte described by Haseeb et al. [D8] at 50 °C and -30 mA/cm². In the following, these deposition conditions will be designated as A65, A50 and B50, respectively. The corresponding bath compositions and deposition parameters are shown in Table D1. Additional experiments under different conditions were performed in order to investigate the effect of certain deposition parameters and will be mentioned in the text. All experiments were performed without bath agitation. Polycrystalline copper plates were used as substrates. The substrates were aligned vertically in the bath and had a size of about 2 mm in thickness and 12 mm in diameter. A rod of ARMCO iron was used as soluble counter electrode.

The structure of the deposits was characterized using a Zeiss LEO1525 scanning electron microscope (SEM) and a Philips CM 12 transmission electron microscope (TEM). X-ray diffraction (XRD) measurements of the as-deposited samples were performed in transmission with high-energy synchrotron radiation at the P07 HEMS beamline of PETRA III [D18]. The photon energy for these experiments was 111 keV and the beam size was 0.1x0.5 mm². Diffractograms of the annealed samples were recorded using a Rigaku SmartLab diffractometer with a Cu-Kα source and a monochromator on the secondary side.

Vickers microhardness was measured on cross-sections of the deposits with a Buehler Micromet5104 machine at a load of 500g (HV0.5). For the nanoindentation experiments, which were also performed on cross-sections of the films, a Hysitron Triboscope with a diamond cube corner indenter was used. Compression and bending experiments were performed with a tension/compression module and a bending module of Kammerath&Weiss, respectively. The compression samples were about 0.5 mm in the growth direction of the films and about 1.0 to 1.5 mm in the other two dimensions; the bending beams were 3 mm in width, 0.3 mm in height and were tested in 3-point bending with a support span of 3.2 mm. The samples for these experiments were prepared by mechanical grinding and polishing. The copper substrates were removed via grinding during the preparation of the compression and bending samples as well as before annealing to avoid crack formation due to the different thermal expansion coefficients of Fe-C deposits and Cu substrates. Annealing was performed under a pressure of about 10^{-5} mbar in a vacuum tube furnace.

Table D1: Standard electrolytes and deposition parameters used in this study. Parameter sets A65 and A50 are new deposition conditions investigated in this work, whereas B50 is taken from [D8].

Sample designation	A65	A50	B50
Bath composition [g/l]			
Ferrous Sulfate Heptahydrate	120		120
Citric Acid	-		1.2
Tri-Sodium Citrate Dihydrate	20		-
L-Ascorbic Acid	3		3
Sodium Sulfate	80		-
Deposition parameters:			
Temperature [°C]	65	50	50
Current Density [mA/cm²]	-50	-30	-30
pH (before deposition)	4.2	4.2	2.5

D.3. Results

D.3.1. Deposition Process

Thick films with a smooth, black surface are obtained in a large range of bath compositions and deposition conditions. From a number of baths containing citric acid, tri-sodium citrate or mixtures of both, the two electrolytes shown in Table D1 provide the best results concerning the availability of thick, smooth deposits over a large current density range as well as concerning a high current efficiency. With these electrolytes, smooth films are obtained for current densities ranging from -20 mA/cm² up to about -50 mA/cm². For lower current densities, coarse grained deposits with a rough surface are formed with a very low current efficiency. The upper current density limit is caused by the formation of powdery deposits and can be shifted towards higher current densities by increasing the deposition temperature.

A cross-section of a typical deposit from this study is shown in Figure D1a. A homogeneous layer with smooth surface is obtained in the center of the substrate. Near the edge of the substrate, the layer thickness increases due to the edge effect, which also results in the growth of dendritic-like features directly at the edge of the samples. This structure can be maintained up to a thickness of
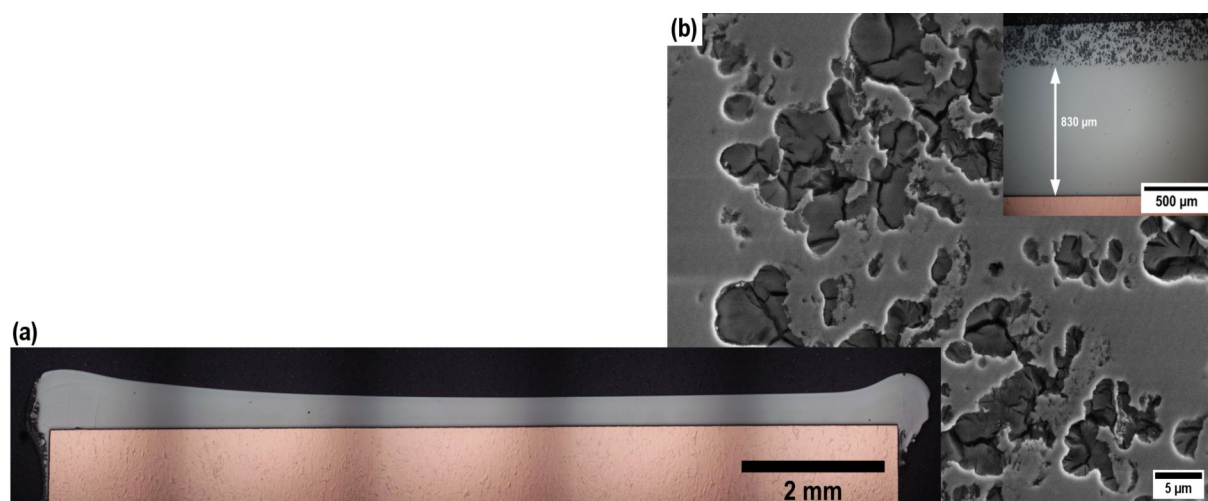
Figure D1: (a) Optical micrograph of a complete sample cross-section after deposition for 22 hours under conditions B50. (b) SEM image of the sponge-like structure with ceramic inclusions formed at the top surface layer after prolonged deposition under conditions A65. The inlay shows a cross-section over the whole thickness of the sample.

more than 800 μm. However, if the deposition process is continued even longer, ceramic particles are included into the deposit resulting in a metallic matrix with ceramic second-phase particles (Figure D1b).

The electrochemical potential directly after starting the deposition with respect to an Ag/AgCl reference electrode is about $E = -1100$ mV to $E = -1150$ mV for conditions A50 and A65, whereas about $E = -1200$ mV are obtained for B50. During deposition, the potential increases up to $E = -1000$ mV to $E = -1050$ mV for A50 and A65 and about $E = -1100$ mV for B50 after 22 hours of deposition. In the same time, the pH increases slightly to 4.3, 4.4 and 3.0 for A50, A65 and B50, respectively. For even longer deposition, the color of bath B50 changes from green to yellow after more than one day of deposition, indicating strong oxidation of the bath, i.e. formation of ferric ions.

The current efficiency calculated via Faraday's law from the mass of the deposits after 22 hours deposition time scatters in the range of 70-90 % for all three deposition conditions. Due to the pronounced edge effect, the current efficiency calculated from the film thickness near the center of the substrate is considerably lower, in the range of 40-50%.

D.3.2. As-Deposited State

D.3.2.1. Microstructure and Composition

SEM shows the nanocrystalline nature of the Fe-C electrodeposits (Figure D2a). Needle-like grains elongated along the growth direction are observed throughout the deposits without any considerable changes over the film thickness. Even for the very thick films, in which the ceramic
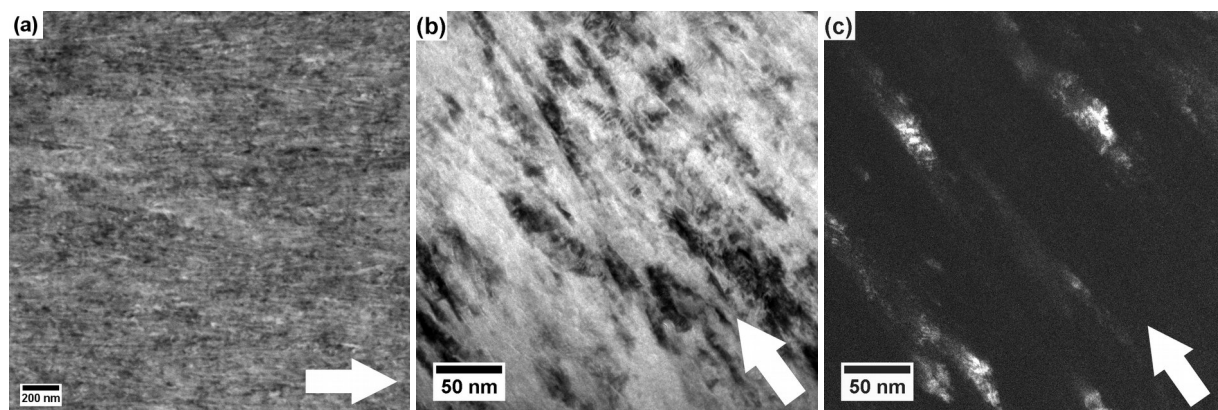
Figure D2: (a) Microstructure of an as-deposited A50 sample imaged with the backscatter-electron detector in the SEM. (b) Bright-field and (c) dark-field TEM images of an A65 sample in a film cross-section. The white arrows indicate the growth direction.

inclusions are observed (Figure D1b), the nanocrystalline structure of elongated grains is preserved, but their orientation becomes random. Only films, for which the deposition was stopped prior to the occurrence of ceramic inclusions, will be discussed in the following. The grains are about 20 nm in the short axis and have an aspect ratio of approximately two to three (Figure D2b-c).

Both TEM selected area diffraction patterns (not shown) and high-energy transmission XRD (Figure D3) show that the deposits consist of a single phase of body-centered cubic structure. Only a tiny peak next to bcc (110) indicates the presence of another phase (Figure D3b). However, the phase could not be determined since only this single peak is visible. Due to the low intensity of the peak and the absence of further Bragg peaks, the amount of the phase is assumed to be very low (<1%) and the films can be considered to be practically single-phase. A tetragonal distortion, as described for electrodeposited Fe-C alloys in literature [D3, D4, D10, D14, D15] could not be found, but a tetragonal distortion with a small c/a ratio cannot be excluded due to the limited angular resolution of the diffraction data. The 2D diffraction patterns clearly reveal the preferred orientation of (211) planes perpendicular to the growth direction (Figure D3a). The presence of a (211) fiber texture without any preferred orientation within the plane parallel to the substrate was proven via a full texture measurement for a deposit from another citrate-based bath (not shown).

Analysis with a Leco CS-125 carbon analyzer revealed carbon contents of 1.0 ± 0.1 wt.-% independent of the deposition conditions within the range of stable deposition of smooth deposits. Indications of significant amounts of oxygen were found using x-ray photoelectron spectroscopy, but no reliable quantitative amounts could be determined.
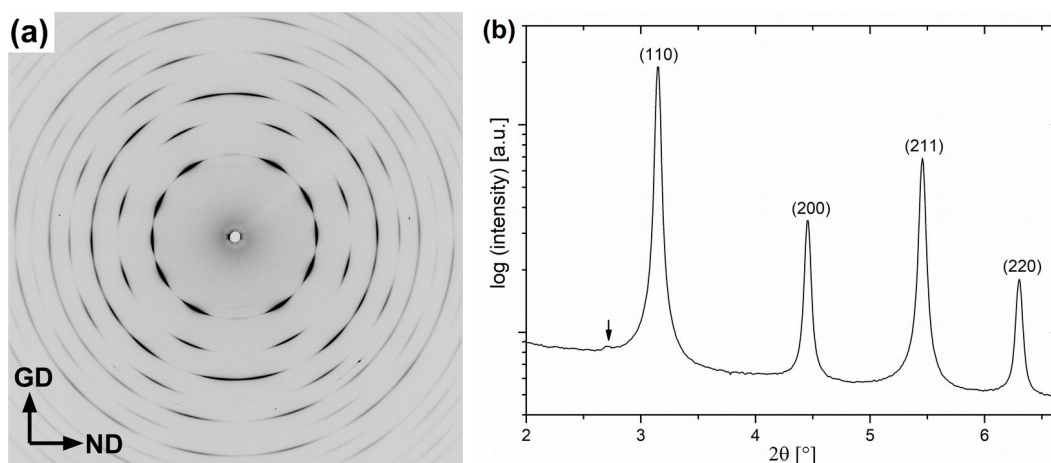
Figure D3: (a) High-energy XRD pattern of a B50 sample recorded with the primary beam in-plane. GD and ND indicate the growth direction and the in-plane direction, respectively. (b) Diffractogram obtained from (a) via integration over all azimuthal angles. The only indication of a small peak besides the ferritic phase is marked with an arrow.

D.3.2.2. Mechanical Properties

The microhardness equals 556 ± 10 HV for A50, 662 ± 28 HV for A65 and 660 ± 17 HV for B50. The hardness of deposits from other citrate and / or citric acid baths lies in between these values. The hardness slightly increases with increasing distance from the substrate. Vickers indents on film cross-sections, which are oriented with one diagonal parallel to the growth direction, show crack formation along this direction, whereas no cracks originating from the Vickers indents occur parallel to the substrate surface (Figure D4a). Using the equation by Niihara [D19] for median cracks obtained from Vickers indentation, estimated fracture toughnesses of 3.8 MPa m$^{0.5}$ are obtained from the measured crack lengths of both A50 and B50 samples, whereas for A65 3.2 MPa m$^{0.5}$ is determined.

Both compression and bending tests reveal a completely brittle fracture behavior. Compression testing, which was performed on samples with the loading axis parallel to the growth direction as well as in normal orientation, results in catastrophic failure by a sudden mechanical collapse of the structure. The cuboidal bulk samples are transferred into many small powder-like particles of elongated shape indicating intercrystalline fracture. The maximum stress before failure scatters in a large range between 400 and 1800 MPa. Large scatter of the maximum stress is also observed in the bending experiments, but at a much lower level, between 100 and 190 MPa. In contrast to the compression samples, the bending beams break along one sharp interface, making the investigation of fracture surfaces feasible. Irregular morphologies varying from one sample to another are observed next to the surface of the bending beams which is under tension upon bending. Near the center, the fracture surface has the lowest roughness, but elongated features of
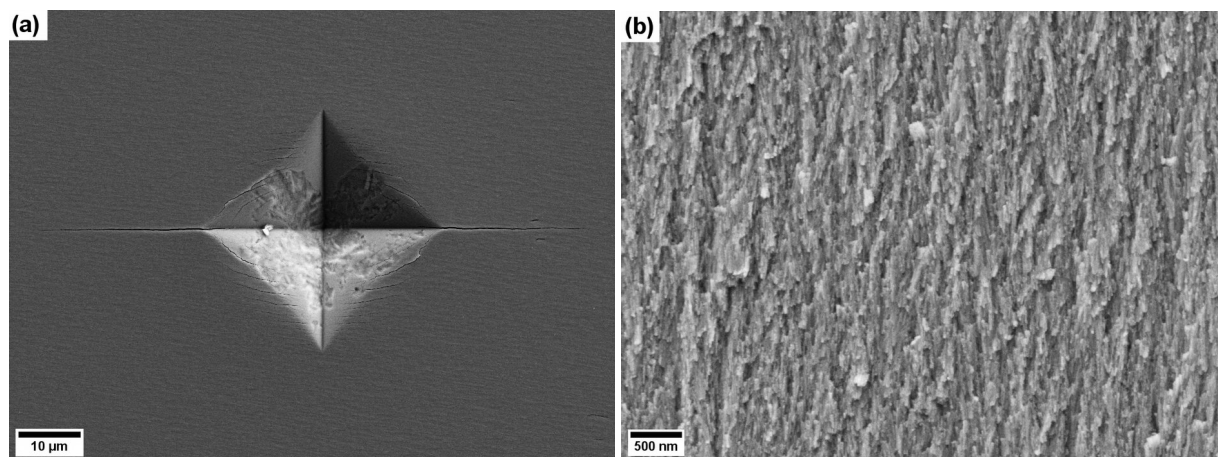
Figure D4: (a) SEM micrograph of a Vickers microindent on the cross-section of a B50 sample. (b) Exemplary fracture surface of an A65 sample after bending.

similar size as the crystallographic grains can be found at higher magnifications in the SEM (Figure D4b). This structure becomes rougher, making an elongated structure even visible in the light microscope, when approaching the edge on the other side of the fracture surface which is mainly loaded with compressive stresses upon bending.

D.3.3. Thermal Stability and Structure Evolution Upon Annealing

During isothermal annealing, the deposits from all three deposition conditions behave similar. For this reason, the evolution upon annealing will be discussed in the following in a general way and conditions A50, A65 and B50 are only differentiated where necessary.

After annealing at 200 or 300 °C, no significant changes in the structure except a slight increase in contrast between the elongated grains can be observed in the SEM (Figure D5a+b). Neither any changes in phase composition are shown by XRD (Figure 6a). This corresponds well with a constant microhardness until 200 °C and only a slight increase at 300 °C (Figure D6b). On the contrary, isothermal annealing at 400 °C results in the formation of equi-axed precipitates with diameters ranging from a few nanometers up to about 70 nm (Figure D5c). Closer investigation of the regions between these precipitates proves the conservation of the elongated grain shape, although some grain growth occurrs. The precipitation results in additional peaks in the XRD patterns, which are identified as cementite and magnetite (Figure D6a). The hardness is considerably increased to more than 800 HV (Figure D6b). Increasing the annealing temperature to 500 °C, the aligned orientation of the microstructure along the growth direction is lost and an isotropic structure exists throughout the film (Figure D5d). The structure is considerably coarsened as compared to the 400 °C annealed material. This coarsening results in a drop of the microhardness below that of the as-deposited state (Figure D6b). XRD indicates no significant changes as compared to 400 °C (Figure D6a).
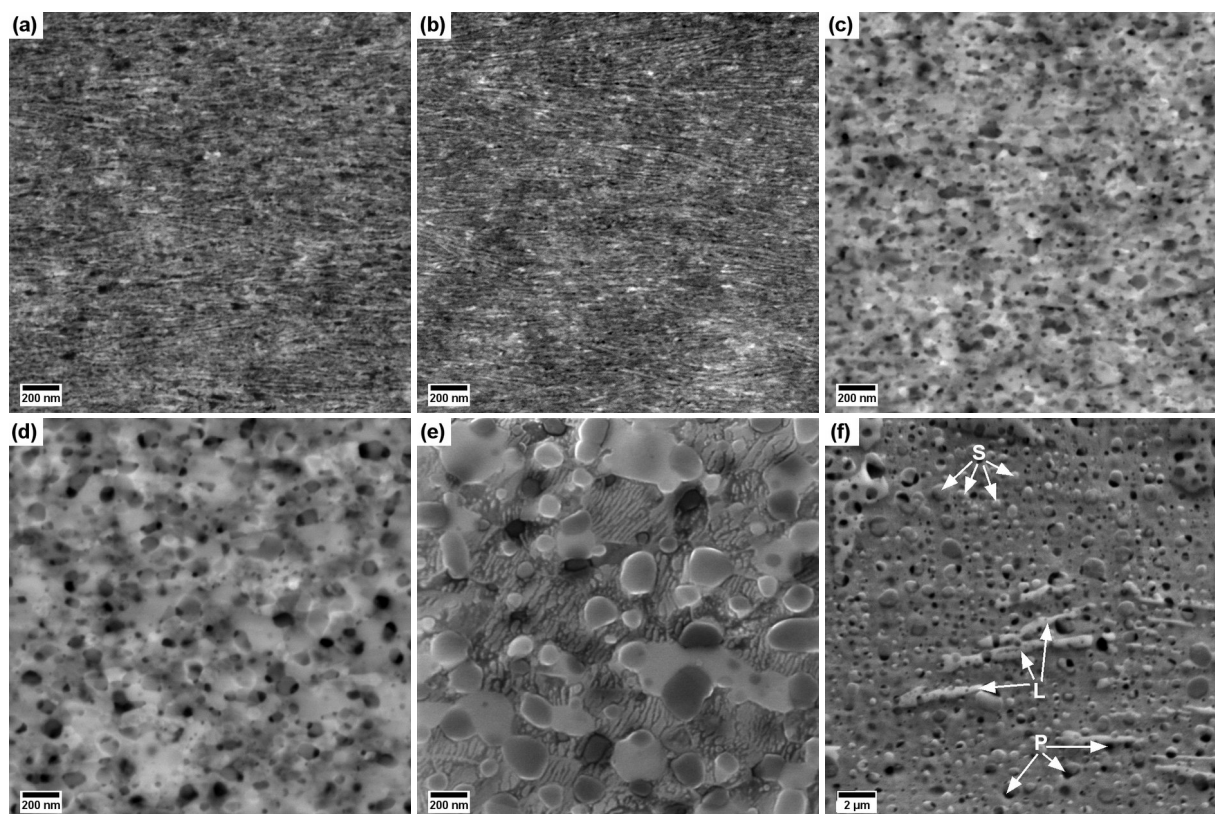
Figure D5: SEM micrographs after isothermal annealing for one hour. (a-d) are recorded with a backscatter-electron detector and show the structural evolution of A50 samples at (a) 200 °C, (b) 300 °C, (c) 400 °C and (d) 500 °C. The lamellar structure observed in B50 samples at 600 °C is shown in (e). The structure after annealing at 800 °C is shown in (f) and selected elongated precipitates (L), spherical precipitates (S) and pores (P) are indicated. The growth direction is from left to right for all images.

For even higher annealing temperatures, further coarsening takes place accompanied by a decreasing microhardness. A lamellar substructure appears in the matrix after annealing at 600 °C; this effect is particularly pronounced in the B50 samples (Figure D5e). However, no new phases are observed in the XRD patterns even for annealing treatments at 800 °C, i.e. above the eutectoid temperature of the Fe-C system [D20]. Using SEM and nanoindentation at specific positions, identified by atomic force microscopy with the nanoindenter tip, three features could be identified in the ferritic matrix after annealing at 800 °C (Figure D5f). First, elongated particles of about 500 nm in width and several microns in length with a nanoindentation hardness of 16.6 ± 1.0 GPa. Next, approximately spherical precipitates are distributed in both the matrix and the larger elongated particles. They have a large size distribution from tens of nanometers up to about one micron and a nanoindentation hardness of 8.4 ± 1.4 GPa. Finally, pores are identified with similar size and shape as the second type of precipitates. XRD patterns after annealing at 800 °C still show ferrite, cementite and magnetite, but the peak width is significantly reduced and the intensity distribution is changed as compared to the lower-annealed samples (Figure D6a).
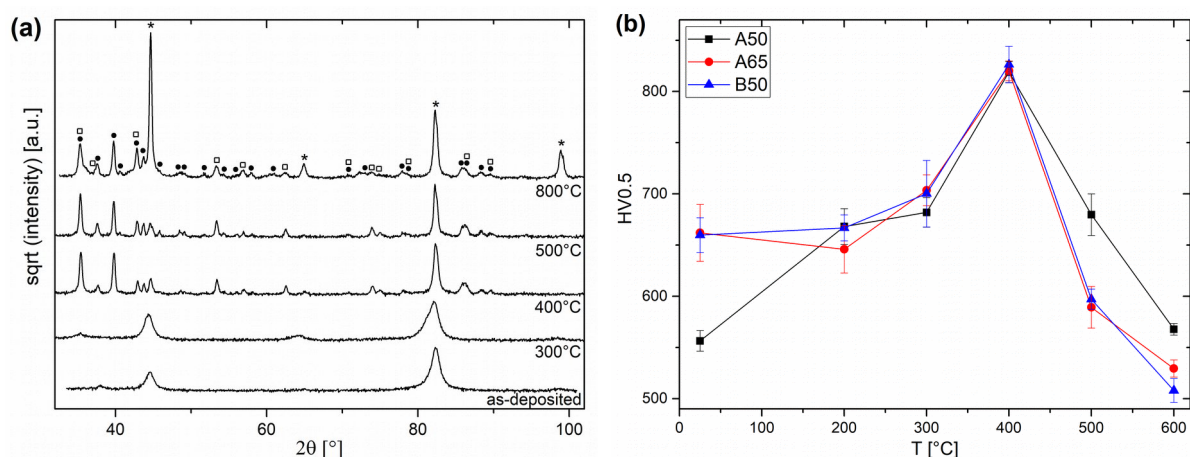
Figure D6: (a) XRD patterns and (b) hardness evolution of isothermally annealed A65 deposits. Bragg peaks of ferrite, cementite and magnetite are indicated with *, ● and □, respectively.

D.4. Discussion

The results show that Fe-C alloys can be deposited from various citrate-based electrolytes with the newly proposed bath leading to very similar deposits as compared to the bath taken from literature. In the following, three aspects of the results, namely the carbon and oxygen codeposition, the thermal stability of the deposits as well as the range of suitable electrolytes for electrodeposition of Fe-C alloys are discussed in more detail.

D.4.1. Codeposition of Carbon and Oxygen

The codeposition of 1.0 ± 0.1 wt.-% C for B50 samples corresponds well with the 0.96 wt.-% C that have been reported by Haseeb et al. for the same deposition conditions [C8]. The chemical analysis shows that with the new citrate bath (A50 and A65) similar carbon contents are obtained. Also with other baths based on iron citrate complexes, the incorporation of about 1 wt.-% C has been regularly reported in literature over a large range of current densities [D3-D6, D10, D12]. Only if the current density falls below a threshold value of about -10 mA/cm², the carbon content decreases significantly [D4, D12]. The mechanism of the codeposition process is still unclear, but it is likely that organic species (based on citrate or ascorbic acid in the bath) are adsorbed at the growth front and incorporated into the metallic matrix [D4, D12]. The adsorption of organic species impedes the growth of existing crystals during deposition, resulting in an enhanced nucleation rate and a refinement of the microstructure. This explains the nanocrystalline structure of the deposits under investigation in contrast to the coarser deposits observed at low current densities.

Whereas the codeposition of carbon is intended due to its beneficial effect on the mechanical properties, the codeposition of oxygen is expected to result in embrittlement and is generally

undesired for this reason. These alloying effects are well-known from steels, in which carbon is regularly used as an alloying element resulting in the industrially important group of carbon steels. On the other hand, the oxygen content is reduced to 50 ppm and less during production in order to improve the quality of the steels [D21]. However, the codeposition of oxygen in the electrodeposition of iron, and particularly Fe-C, has regularly been observed [D4, D15, D22] and is also present in the present study. Due to the lack of reasonable results via chemical analysis, the oxygen content was estimated from the amount of magnetite in 800°C annealed samples that was determined via Rietveld refinement of the XRD data and then converted to oxygen contents assuming a near-equilibrium state with all dissolved oxygen transformed into magnetite. With this method, the oxygen contents of A50, A65 and B50 samples are estimated to be 5, 4 and 3 wt.-%. Although these results should be considered with care due to the general inaccuracy, the effect of texture and instabilities of the Rietveld refinement process, the carbon contents obtained via this method equal 1.2-1.3 wt.-% for all three conditions, which is in good agreement with the 1.1 ± 0.1 wt.-% obtained from chemical analysis and shows the plausibility of the results. Whereas the oxygen contents contradict with the negligible oxygen contents up to -30 mA/cm² and 2 wt.-% O for -70 mA/cm² as reported by Izaki et al. [D4], they match very well with the 4.7 wt.-% obtained by Miyamoto et al. for Fe-C deposits from a chloride bath containing citric and ascorbic acid [D15]. The differences can be attributed to the different electrolytes as well as to different experimental conditions such as dissolved oxygen in the electrolytes. Oxygen contents have been reported to be reduced by inert gas bubbling and by adding boric acid to the bath [D22]. However, gas bubbling also causes bath agitation, which is known to reduce the current efficiency for Fe-C deposition [D10]. In this study, the use of citrate buffer solutions as a potential alternative to boric acid were tested. However, no significant reduction of the oxygen content according to the XRD analysis is obtained, but the current efficiency is reduced as compared to the conditions A50, A65 and B50.

As shown in Figure D3, the as-deposited state consists practically of a single-phase solid solution of iron, carbon and oxygen. The measured carbon and estimated oxygen contents are far beyond the negligible equilibrium solubilities of these elements in iron at room temperature [D20, D23]. This strong supersaturation raises the question, how the carbon and oxygen atoms are distributed in the ferritic structure. If the supersaturation was achieved via a homogeneous distribution in the interstitial sites of the ferritic lattice, the lattice parameter would be significantly increased which is in contradiction to the XRD results. For this reason, it is more likely that carbon and oxygen are concentrated at defects sites, in particular at the grain boundaries. The incorporation of carbon and oxygen from adsorbed species at the growth front during deposition might explain such a distribution since the adsorbed species impede the grain growth, give rise to the formation of new

grains and are then incorporated at the newly formed grain boundaries. The formation of clustered carbon distributions rather than a homogeneous distribution of interstitial carbon atoms has also been proposed by Haseeb et al. based on Mössbauer spectroscopy measurements [D8]. The segregations result in a mechanical weakening of the grain boundaries. This explains the intercrystalline fracture in the bending tests and the catastrophic failure and transformation into powder under compressive loading. The large scatter of the load bearing capacity in these tests is caused by the statistical distribution of defects since the size of the largest defect differs from one sample to another and immediately affects the maximum applied load before failure. The elongated, straight grain boundaries in growth direction facilitate crack growth which results in the low maximum stresses in the bending tests as well as the preferred crack formation in this direction during Vickers indentation.

The hardness of the as-deposited samples in the current study is within the range of 600-800 HV that can be found in literature [D4, D6-D8, D12, D15]. The hardness of the B50 samples in this study is lower than the 810 HV reported for the same deposition conditions by Haseeb et al. [D8]. Although the microstructure and the carbon contents look almost identical, this difference as well as the different hardness values in literature might be a result of different experimental conditions leading to structural differences of the deposits, e.g. concerning oxygen contents and residual stresses. However, the different loads used in these studies (e.g. 20 g in [D8] vs. 500 g in the present work) might also contribute to the hardness differences via the indentation size effect [D24]. The lower hardness of the A50 samples as compared to the A65 and B50 structures in the present work is probably caused by the higher oxygen contents in this case which facilitate crack growth and, thus, penetration by the indenter. Strengthening via oxide formation or oxygen redistribution might explain the outbalancing of this hardness difference upon annealing.

D.4.2. Discussion of the Thermal Stability

In contrast to the disastrous effect of the grain boundary segregations on the mechanical properties, they provide the fundament for a strong thermal stability. In the temperature range up to 300 °C, where the carbon and oxygen atoms stay in segregated solid solution, they inhibit any significant grain growth in spite of the very small grain size of about 20 nm.

The precipitation of cementite and magnetite, that is observed for higher temperatures in the present study, is in contradiction to the formation of cementite via intermediate carbides as found by Izaki et al. [D5] and Haseeb et al. [D7, D8]. However, the preservation of the same peak positions in the XRD patterns even after austenitization at 800 °C, clearly shows that the observed phase is the thermodynamically stable magnetite and no intermediate carbide. Furthermore, the qualitative evidence of oxygen codeposition via x-ray photoelectron

spectroscopy and the negligible solubility of oxygen in iron according to the phase diagram require the formation of an oxide phase during annealing. The two precipitate phases can also be differentiated by nanoindentation and according to their shape and size after annealing at 800 °C. On the contrary, only approximately spherical precipitates of nanometer to sub-micron size exist at lower annealing temperatures in spite of very similar XRD patterns, indicating a similar morphology of magnetite and cementite in this temperature range. This difference of the 800 °C samples as compared to the lower annealing temperatures can be attributed to passing the eutectoid temperature of the Fe-C phase diagram (740 °C [D20]). Thus, the ferritic matrix transforms into austenite, in which carbon has a solubility of nearly 1 wt.-% at 800 °C [D20]. The spherical cementite particles dissolve during annealing and precipitate again during cooling, giving rise to a change of particle shape and size with a large size enabled by the low cooling rate in the vacuum furnace. On the contrary, oxygen does not show any considerable solubility in iron up to 1528 °C, where the melting process sets in [D23]. For this reason, the oxide particles may change their size via diffusion and may transform from magnetite to wüstite during heating and transform back during cooling, but no complete dissolution and re-nucleation takes place. Thus, the large elongated precipitates in Figure D5f can be identified as cementite, whereas the smaller spherical precipitates can be ascribed to magnetite.

The precipitation affects the hardness of the deposits in two ways. On the one hand, the formation of second-phase particles with a significantly higher hardness compared to the matrix results in a hardening. On the other hand, the vanishing grain boundary segregations facilitate grain growth in the matrix, causing a hardness decrease. At 400 °C, the nanoprecipitates provide a strengthening effect and the elongated grains in the matrix are preserved, indicating that the precipitation is not yet completed and grain boundary segregations still stabilize the nanocrystalline structure. This explains the hardening effect at this temperature (Figure D6b), which has been observed in a similar temperature range by Izaki et al. [D5]. At higher temperatures, the loss of the grain boundary stabilization due to complete precipitation of carbon and oxygen in the form of cementite and magnetite gives rise to grain growth, causing the observed softening. The growth of the precipitates with increasing temperature supports this coarsening, since the number of obstacles for grain boundary motion decreases. Nevertheless, it is worth mentioning that the grain size after annealing at 600 °C is still below one micron, which can be attributed to the barrier to grain growth promoted by the large fraction of second-phase particles. The higher hardness of the A50 deposits at this high annealing temperatures as compared to the A65 and B50 deposits (Figure D6b) is attributed to a larger amount of oxide precipitates due to the higher oxygen content. The lamellar structure observed at 600 °C supports the thermal stability because of its nanocrystalline structure. However, its formation is currently

not understood. Its random orientation excludes direct formation of a two-phase lamellar structure from the lamellar single-phase structure with grain boundary segregations in the as-deposited state. The structure looks like the result of a eutectoid decomposition, but the annealing temperature is well below the eutectoid temperature of the Fe-C system.

D.4.3. Comparison of Different Electrolytes for Fe-C Electrodeposition

The results show no significant differences between the samples obtained from the deposition conditions A50, A65 and B50. The existence of a range of deposition conditions, particularly current densities, in which deposits with only small deviations in carbon content, microstructure, and, thus, hardness are obtained, can also been concluded from former studies such as [D11]. The new citrate bath tested in this study is within this range.

Citrate buffer solutions were tested in this study in order to impede the pH increase next to the substrate due to the evolution of hydrogen. The layers from these baths also had a similar structure and a hardness between those of A50 and A65 deposits. However, the current efficiency is significantly reduced. Thus, this approach is not suitable for the electrodeposition of thick Fe-C films.

The enhanced hardness of electrodeposits from succinic acid baths has been reported by Fujiwara et al. [D11]. This was reproduced in preliminary experiments of the current work resulting in a hardness of about 750 HV in the as-deposited state. However, reduced current efficiency was observed in contrast to the findings in [D11]. Additionally, low bath stability and enhanced brittleness of the deposits limit the practical use of the succinic acid bath.

The citrate bath from this study is found to be the most suitable electrolyte for the deposition of thick films with high hardness. The deposition under conditions A65 allows the preparation of films with almost identical structure and properties compared to B50, but with higher current density, i.e. faster growth rate. Nevertheless, the practical use of the deposits is limited due to the codeposition of oxygen causing embrittlement of the structure.

D.5. Conclusions

The codeposition of carbon in iron electrodeposits from iron-citrate complexes in the electrolyte has been reviewed and a new bath based on sodium citrate is proposed which is found to be suitable for the deposition of thick films up to more than 800 μm. The nanocrystalline structure with a grain size of about 20 nm results in a hardness of up to 660 HV. This hardness can be further increased to more than 800 HV via annealing. However, the embrittlement due to the

codeposition of oxygen limits the mechanical load-bearing capacity of the deposits from both the new and previously proposed electrolyte. On the other hand, the codeposited carbon and oxygen provide considerable thermal stability of the structure. Even after annealing at 600 °C, the structure is still ultrafine-grained.

Acknowledgments

Author Contributions

T.M., A.B. and R.P. conceived and designed the experiments. T.M. performed the electrodeposition experiments and wrote the manuscript. T.M. and J.G. performed the structural and mechanical analysis of the deposits. All authors contributed to the finalization of the manuscript.

References

D1 Yu. N. Petrov, Porous electrodeposition of iron and its use in repair of machine parts, Doklady Akad. Nauk Tadzhik. S.S.R. 20 (1957), 67-70. Summary: Chem. Abstr. 53 (1959), 8879e.

D2 M. Izaki, H. Enomoto, T. Omi, Hardness and carbon content of Fe electroplate from sulfate bath containing l-ascorbic acid and citric acid, J. Surf. Fin. Soc. Jpn. 40 (1989), 1304-1305. http://dx.doi.org/10.4139/sfj.40.1304

D3 M. Izaki, H. Enomoto, T. Omi, Structure and hardness of Fe-C alloy film electrodeposited from an iron sulfate electrolyte, J. Japan Inst. Metals 56 (1992), 636-640. http://dx.doi.org/10.2320/jinstmet1952.56.6_636

D4 M. Izaki, T. Omi, Structural characterization of martensitic iron-carbon alloy films electrodeposited from an iron(II) sulfate solution, Metall. Mater. Trans. A 27 (1996), 483-486. http://dx.doi.org/10.1007/BF02648429

D5 M. Izaki, H. Enomoto, A. Nakae, S. Terada, E. Yamauchi, T. Omi, Phase transformations and hardness changes in electrodeposited Fe-C alloy films, J. Surf. Fin. Soc. Jpn. 45 (1994), 1302-1307. http://dx.doi.org/10.4139/sfj.45.1302

D6 A.S.M.A. Haseeb, M.Z. Huq, Electrodeposition of martensitic iron-carbon alloy coatings at room temperature, Met. Finish. 95 (1997), 30-34. http://dx.doi.org/10.1016/S0026-0576(97)86770-0

D7 A.S.M.A. Haseeb, M. Arita, Y. Hayashi, Thermal decomposition study of electrodeposited Fe-C and Fe-Ni-C alloys by differential scanning calorimetry, J. Mater. Sci. 36 (2001), 4739-4743. http://dx.doi.org/10.1023/A:1017931106376

D8   A.S.M.A. Haseeb, Y. Hayashi, M. Masuda, M. Arita, On the nature of the electrochemically synthesized hard Fe-0.96 mass pct C alloy film, Metall. Mater. Trans. B 33 (2002), 921-927. http://dx.doi.org/10.1007/s11663-002-0076-4

D9   Y.J. Oh, H.P. Ha, J.S. Byun, Effect of pulse plating on the hardness and ductility of electroplated Fe-C, J. Korean Inst. Surf. Eng. 35 (2002), 141-148.

D10 Y. Fujiwara, M. Izaki, H. Enomoto, A. Nakae, Effects of hydroxycarboxylic acids on the electrodeposition of Fe-C alloys, Denki Kagaku 61 (1993), 840-842.

D11 Y. Fujiwara, T. Nagayama, A. Nakae, M. Izaki, H. Enomoto, E. Yamauchi, Electrodeposition of Fe-C alloys from baths containing dicarboxylic acids with a linear alkyl chain, J. Electrochem. Soc. 143 (1996), 2584-2590. http://dx.doi.org/10.1149/1.1837051

D12 Y. Fujiwara, M. Izaki, H. Enomoto, T. Nagayama, E. Yamauchi, A. Nakae, Optimization of bath composition for hard Fe-C alloy plating, J. Appl. Electrochem. 28 (1998), 855-862. http://dx.doi.org/10.1023/A:1003444610964

D13 N. Miyamoto, S. Sakamoto, H. Tamuro, M. Matsuoka, J. Tamaki, Effect of carbon content on structural and mechanical properties of Fe-Co-C alloy electrodeposited from aqueous solutions, J. Electrochem. Soc. 152 (2005), C488-C492. http://dx.doi.org/10.1149/1.1837051

D14 M. Izaki, N. Miyamoto, A. Nakae, T. Hasegawa, S. Watase, M. Chigane, Y. Fujiwara, M. Ishikawa, H. Enomoto, Martensitic iron-carbon-boron alloy electrodeposit with improved mechanical properties, J. Electrochem. Soc. 149 (2002), C370-C374. http://dx.doi.org/10.1149/1.1484376

D15 N. Miyamoto, K. Yoshida, M. Matsuoka, J. Tamaki, Effect of phosphorus content on mechanical properties of electrodeposited Fe-C-P alloys, J. Electrochem. Soc. 151 (2004), C645-C648. http://dx.doi.org/10.1149/1.1785798

D16 Y.D. Gamburg, G. Zangari, Theory and Practice of Metal Electrodeposition, Springer, New York, 2011, p. 302. http://dx.doi.org/10.1007/978-1-4419-9669-5

D17 N. Fukumuro, S. Kojima, M. Fujino, Y. Mizuta, T. Maruo, S.Yae, Y. Fukai, Hydrogen-induced superabudant vacancies in electrodeposited Fe-C alloy films, J. Alloys Comp. 645 (2015), S404-S407. http://dx.doi.org/10.1016/j.jallcom.2014.12.093

D18 N. Schell, A. King, F. Beckmann, T. Fischer, M. Müller, A. Schreyer, The high energy materials science beamline (HEMS) at PETRA III, Mater. Sci. Forum 772 (2014), 57-61. http://dx.doi.org/10.4028/www.scientific.net/MSF.772.57

D19 K. Niihara, A fracture mechanics analysis of indentation-induced Palmqvist cracks in ceramics, J. Mater. Sci. Lett. 2 (1983), 221-223. http://dx.doi.org/10.1007/BF00725625

D20 H. Okamoto, The C-Fe (carbon-iron) system, J. Phase Equilib. 13 (1992), 543-565. http://dx.doi.org/10.1007/BF02665767

D21 L. Zhang, B.G. Thomas, X. Wang, K. Cai, Evaluation and control of steel cleanliness – review, Steelmaking Conf. Proc. 85 (2002), 431-452.

D22 S. Gadad, T.M. Harris, Oxygen incorporation during the electrodeposition of Ni, Fe and Ni-Fe alloys, J. Electrochem. Soc. 145 (1998), 3699-3703. http://dx.doi.org/10.1149/1.1838861

D23 B. Sundman, An assessment of the Fe-O system, J. Phase Equilib. 12 (1991), 127-140. http://dx.doi.org/10.1007/BF02645709

D24 W.D. Nix, H. Gao, Indentation size effects in crystalline materials: a law for strain gradient plasticity, J. Mech. Phys. Solids 46 (1998), 411–425. http://dx.doi.org/10.1016/S0022-5096(97)00086-0

Publication E

Mechanical Properties of Electrodeposited Amorphous/Crystalline Multilayer Structures in the Fe-P System

Timo Müller[1], Andrea Bachmaier[1], Ruth Konetschnik[2], Thomas Schöberl[1] and Reinhard Pippan[1]

[1]   Erich Schmid Institute of Materials Science, Austrian Academy of Sciences, Leoben, Austria

[2]   Department Materials Physics, Montanuniversität Leoben, Austria

Abstract

Amorphous/crystalline multilayer structures of Fe-P alloys were deposited electrochemically using the single bath technique. Hall-Petch behavior of microhardness with respect to sublayer thickness was observed down to a sublayer thickness of 15 nm. For thinner sublayers, a hardness plateau was obtained. The transition at a sublayer thickness of 15 nm coincides with the loss of the multilayer structure as observed in transmission electron microscopy. The transition is a possible result of a change in the amorphous to crystalline sublayer thickness ratio and the interface roughness development during the deposition process. Additionally, crack deflection at the interfaces was observed for the layered structures with small sublayer thickness in microbending experiments.

E.1. Introduction

Lamellar structures with lamella widths in the submicron to nanometer regime have attracted much attention due to their unique properties, for example concerning magnetism [E1-E3] or mechanical strength [E4]. The mechanical strength is generally observed to increase with decreasing lamella thickness for crystalline structures. This is equivalent to the Hall-Petch behavior in bulk materials [E5, E6]. Indeed, the size dependency for lamellar structures is well described in many cases using the Hall-Petch equation with the sublayer thickness instead of the grain size [E7-E10]. In other studies, a linear behavior of hardness or yield stress as a function of the reciprocal sublayer thickness was observed [E11, E12]. Independent of the exact relationship of strength and sublayer thickness, no further increase or even a decrease of strength is observed

below a certain sublayer thickness, which is typically between 2 and 50 nm [E8-E10, E13]. Various explanations for this phenomenon, which are mainly based on a change of deformation mechanisms on the nanometer scale, are discussed in literature [E9, E10].

On the contrary, no clear dependence of the strength on the layer thickness is reported for amorphous layers [E14]. This can be attributed to the different deformation mechanism of amorphous structures which is based on shear transformation zones as the carriers of plastic deformation [E15]. Multilayer structures of alternating amorphous and crystalline sublayers are promising candidates for high strength materials since the combination of the different deformation mechanisms allows materials with high strength, strain hardening and reduced tendency for strain localization.

Most previous studies on the mechanical properties of amorphous/crystalline multilayer structures have been conducted on sputtered Cu/Cu-Zr multilayer structures [E16-E18]. It was found that the presence of the crystalline layers prevents the formation of catastrophic shear bands in the amorphous phase which was attributed to a minimum size that is necessary to induce shear localization [E16]. Similar results were obtained by Donohue et al. for sputtered Cu/Pd-Si multilayer structures [E19].

Multilayer structures can also be produced using electrochemical deposition. Two different techniques for electrodeposition of such structures exist [E7]. In the dual bath technique, different electrolytes are used for each set of sublayers and the sample is transferred between the baths after deposition of each sublayer. This technique allows a large variety of multilayer systems, but is technologically challenging due to possible contamination during the transfer between the baths [E7, E20]. The other technique, which is used in the present study, is the single bath technique. The complete multilayer structures are deposited from one electrolyte by changing one deposition parameter periodically during the deposition process. Thus, the technique is restricted to systems, in which all sublayer structures can be deposited from the same bath changing only one deposition parameter such as current density [E7]. Both techniques have been applied to many systems, also including amorphous/crystalline multilayers [E21-E24].

Although later and less intensively investigated than the analogous systems Co-P and especially Ni-P [E25], electrodeposition of Fe-P alloys is well known and various properties of such alloys have been examined. The structure of electrodeposited Fe-P alloys depends on their phosphorus content. For more than about 15–22 at.-% P an amorphous material is formed, whereas for smaller phosphorus contents the alloy crystallizes as interstitial solid solution of body-centered cubic structure [E26-E30]. Regularly, a mixture of crystalline and amorphous structures is reported for intermediate phosphorus contents [E27, E28]. Similar results are also known for

electroless Fe-P alloys [E31, E32]. The phosphorus content of the deposits depends on many deposition parameters, such as bath composition, current density and temperature [E27, E30, E33]. The composition range of amorphous structures can be extended towards lower phosphorus contents using pulsed deposition current [E34, E35].

Although the dependency of the structure on the phosphorus content provides the possibility to produce layered structures with periodically changing phosphorus contents using the single bath technique, only a few studies exist on this topic, which are even restricted to the analogical system Ni-P. Elias et al. deposited amorphous/crystalline multilayer samples in the Ni-P system and proved an improved corrosion resistance as compared to homogeneous coatings [E36]. The Ni-P systems was also used as a model system during the improvement of the dual bath technique [E20, E21] and diffusion measurements were performed on amorphous/crystalline multilayers produced with this technique [E22]. Besides, indications of multilayer structures were found in Ni-P deposits prepared under constant potential or current density, respectively [E37, E38]. For the Fe-P system, Kamei and Maehada investigated pulsed electrodeposition, but reported multilayer structures only for the Fe-Cu-P system [E34]. Thus, no study on deposition of amorphous/crystalline multilayers of Fe-P alloys and no investigations on the mechanical properties of amorphous/crystalline electrodeposits in general exist to the authors' knowledge.

In this work, Fe-P multilayer structures are prepared using the single bath technique. The use of electrodeposition allows the production of samples with a significantly larger total thickness as compared to previous work on sputtered films [E18]. The deposition parameters are chosen in such a way that both amorphous and crystalline sublayers can be obtained by changing the current density. The dependence of the mechanical properties of these structures on the sublayer thickness is evaluated using microhardness, nanoindentation, and microbending testing. Additionally, direct current samples are investigated to get more insights into the properties of the two phases combined in the multilayer structures.

E.2. Experimental details

E.2.1. Electrodeposition

The multilayer structures were deposited electrochemically on mechanically polished polycrystalline copper plates of 12 mm diameter. The bath composition was 160 g/l iron(II) sulfate heptahydrate, 12 g/l sodium chloride, 20 g/l ammonium chloride, 15 g/l sodium hypophosphite hydrate, 0.2 g/l sodium dodecyl sulfate. Deposition was carried out at 60 °C and a pH of 2.35 ± 0.05 was adjusted both before and during the experiments using sulfuric acid. An iron rod was used as soluble counter electrode. All deposition experiments were performed under

galvanostatic control using an IPS Jaissle PGU OEM-2A-MI potentiostat. The current density was switched between -10 mA/cm^2 and -80 mA/cm^2 to obtain amorphous and crystalline layers, respectively. For all samples, except where noted otherwise, an identical nominal layer thickness for the amorphous and the crystalline layers was chosen. This nominal layer thickness was varied over a large range from 10 nm to 800 nm for different samples. The deposition times for each layer were chosen accordingly using Faraday's law. The total nominal layer thickness was 50 μm for all samples.

E.2.2. Sample characterization

Cross-sections were investigated using scanning and transmission electron microscopy (SEM and TEM). SEM samples were polished with water-free suspensions. For investigations of the multilayer structures, they were subsequently etched for 10 s in a diluted nital solution consisting of 0.25 vol.-% nitric acid in ethanol. SEM investigations were carried out using a Zeiss LEO1525 instrument, which was also used for energy-dispersive X-ray spectroscopy (EDX). A Philips CM12 machine was used for TEM analysis on cross-sections prepared by mechanical polishing and subsequent thinning in a focused ion beam machine. High-resolution TEM and EDX were performed on a JEOL 2100F machine.

X-ray diffraction (XRD) measurements were performed on the as-deposited film surface using a Rigaku SmartLab instrument with CuKα radiation. Vickers microhardness testing was also carried out on the as-deposited surface with a load of 100 g (HV 0.1). Nanoindentation was performed with a diamond cube corner tip on water-free polished surfaces both parallel and perpendicular to the substrate surface using a Hysitron Triboscope with a maximal load of 6 mN.

E.2.3. Micromechanical testing

Microbending beams were prepared as described in [E39] using a HITACHI E-3500 ion polisher and a Zeiss LEO 1540XB focused ion beam machine. The cuboidal bending beams were approximately 30 μm long, 9 μm broad and 5 μm thick after the final polishing with a Ga$^+$ ion current of 200 pA. The loading axis was perpendicular to the substrate surface. The beams were bent until catastrophic failure under displacement control with a velocity of 1 μm per minute. The bending experiments were carried out using an ASMEC UNAT-SEM microindenter in a Zeiss LEO 982 SEM.

E.3. Results

E.3.1. Comparative samples without multilayer structure

To prove the suitability of the system for amorphous/crystalline multilayer deposition, direct current deposits were prepared with the current densities that were later used for the two sets of sublayers in the multilayer samples. The XRD patterns of these deposits reveal the mainly amorphous and crystalline structure obtained at -10 mA/cm^2 and -80 mA/cm^2, respectively (Figure E1). However, the XRD pattern of the amorphous structure contains some small Bragg peaks. Most of them can be attributed to the copper substrate, but the peak at $2\theta = 82°$ seems to originate from bcc Fe-P crystallites. Nevertheless, these deposition conditions are a suitable candidate for the deposition of amorphous sublayers in a multilayer structure since the prolonged deposition with low current density for the direct current samples makes the formation of crystals more probable due to the depletion of phosphorus in the bath. Table E1 shows the hardness and the phosphorus contents for the direct current deposits. The difference in hardness obtained from microhardness testing and nanoindentation is attributed to the different indenter geometries, i.e. a Vickers indenter and a cube corner tip, respectively, in combination with the well-known indentation size effect [E40]. The phosphorus contents correspond well with the compositions of amorphous and crystalline Fe-P electrodeposits according to literature [E26-E30].
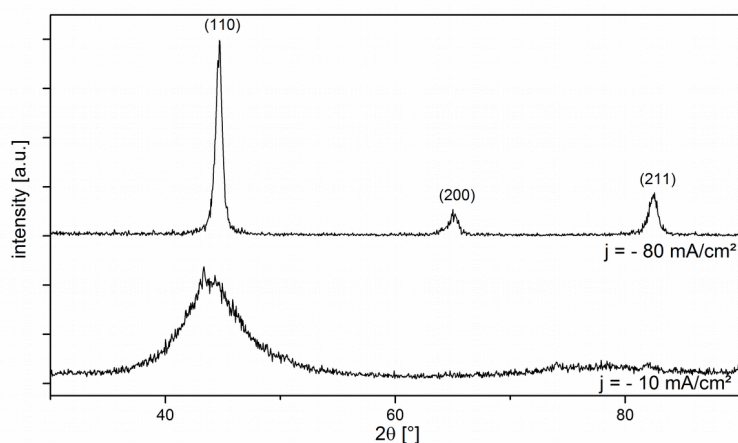

Figure E1: XRD patterns of direct current deposits prepared with current densities of -80 mA/cm^2 and -10 mA/cm^2 resulting in a crystalline and amorphous structure, respectively.

Table E1: Hardness, phosphorus content and structure of direct current deposits. The phosphorus contents were determined using EDX in the SEM. Nanoindentation was performed on cross-sections.

Current density [mA/cm²]	-10	-80
Structure	Amorphous	Crystalline
Microhardness [GPa]	4.65 ± 0.18	4.94 ± 0.18
Nanoindentation hardness [GPa]	6.07 ± 0.04	8.70 ± 0.14
at.-% P	19.3 ± 0.1	6.8 ± 0.2

E.3.2. Structural characterization of multilayer samples

The total thickness of the deposits was measured from SEM micrographs and the cathodic current efficiency was calculated using Faraday's law assuming that only the reduction of ferrous ions to iron atoms takes place at the cathode. The cathodic current efficiency scatters in a range from about 30–60% without any obvious dependency on the sublayer thickness or any other measured deposition parameter. The average sublayer thickness of each sample was calculated as the product of the nominal sublayer thickness and the cathodic current efficiency obtained from the total film thickness measured in the SEM, assuming equivalent thickness of amorphous and crystalline sublayers.

Before etching, no sublayer structure was observed in the SEM. However, after etching the multilayer structure becomes visible over the complete range of sublayer thicknesses of this study (Figure E2). Only for sublayer thicknesses of less than 15 nm the multilayer structure was usually not observed over the whole sample, but only in some regions. Besides, in thin multilayer structures also delamination, i.e. cracking parallel to the layer orientation, was observed (Figure E2d). However, no cracks were observed on the same samples before etching.
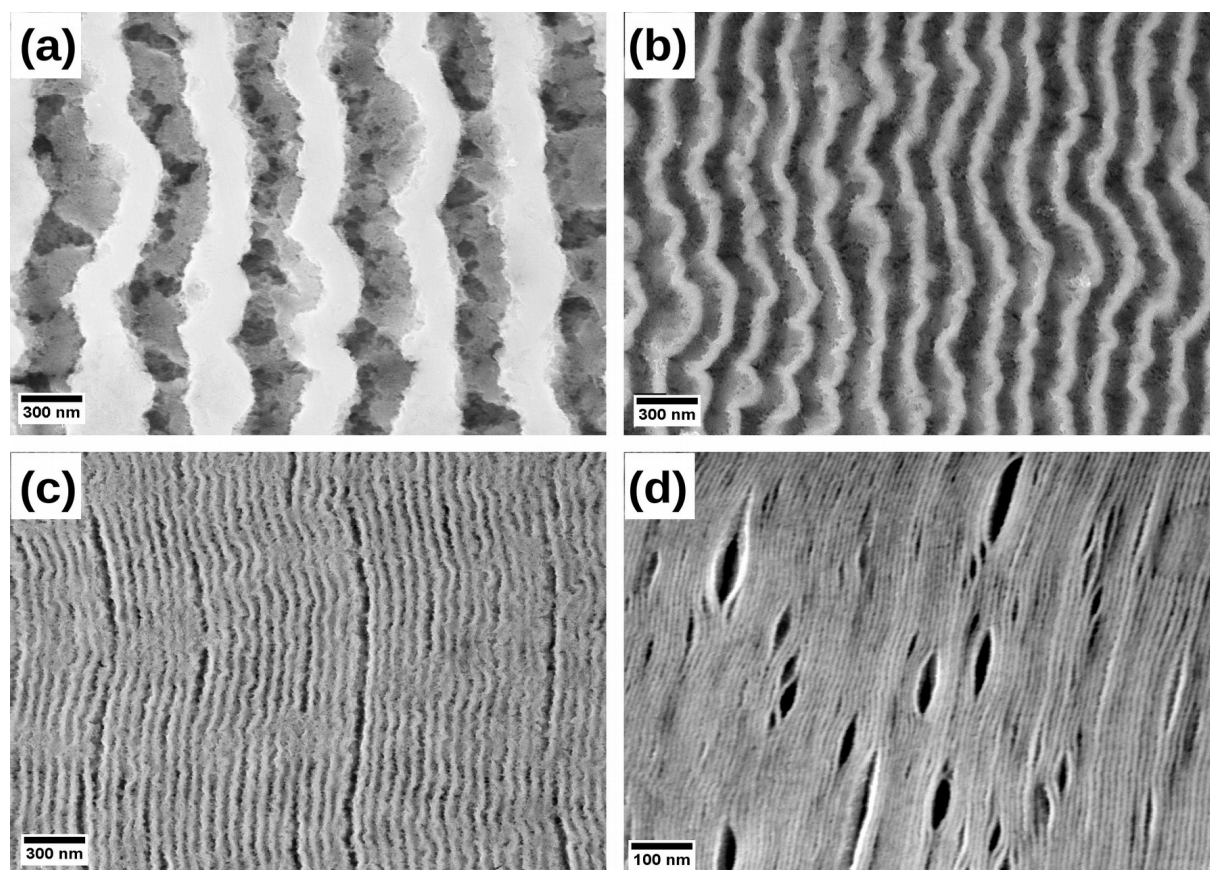
Figure E2: SEM micrographs of etched multilayer samples with (a) 250 nm, (b) 100 nm, (c) 30 nm, and (d) 5 nm average sublayer thickness.

Amorphous and crystalline structures can be differentiated in the SEM since one set of sublayers is almost unaffected by etching, whereas the other one is attacked by the etching solution and shows a substructure indicating the presence of crystalline grains (Figure E2a). The amorphous and crystalline structure of the sublayers was proven by TEM for selected samples (Figure E3). For a sample with 250 nm average sublayer thickness, the area diffraction patterns recorded in the two sets of sublayers show their crystalline or amorphous structure, respectively (Figure E3a). High-resolution TEM performed with samples of 290 nm (Figure E3b) and 30 nm sublayer thickness (not shown) confirm these findings. For smaller sublayer thicknesses, the amorphous/crystalline multilayer structure was observed down to an average sublayer thickness of 15 nm (Figure E3b–c). However, for average sublayer thicknesses of less than 15 nm, no multilayer structure was observed in TEM (Figure E3d). For some samples, the sublayer thicknesses in the TEM micrographs deviate significantly from the average sublayer thickness. This can be attributed to local fluctuations of the sublayer thickness as well as to non-perpendicularity of the TEM cross-sections.

For an average sublayer thickness of 290 nm, 14 at.-% P and 3 at.-% P were measured using EDX in the TEM for the amorphous and crystalline sublayers, respectively. For the sample shown in Figure E3c having a sublayer thickness of 30 nm, measurements in the amorphous layers revealed 11 at.-% P, whereas 4 at.-% P were measured in the crystalline parts of the sample.

The roughness of the interfaces was evaluated from SEM cross-sections. The interface roughness increases during growth and reaches R_{rms} = 50 nm to R_{rms} = 100 nm at a distance of ten micrometers from the substrate. The final roughness at the surface scatters between R_{rms} = 100 nm and R_{rms} = 250 nm without any obvious dependence on the sublayer thickness.

Residual stress measurements on selected samples using XRD regularly resulted in non-linear $\sin^2\psi$ plots, which may occur due to texture or stress gradient effects [E41]. However, more sophisticated measurements are necessary to measure the absolute residual stresses in the crystalline set of sublayers, which is beyond the scope of this work. Nevertheless, all $\sin^2\psi$ plots have a positive slope and $\sin^2\psi$ analysis indicates tensile residual stresses in the order of several hundred megapascals.
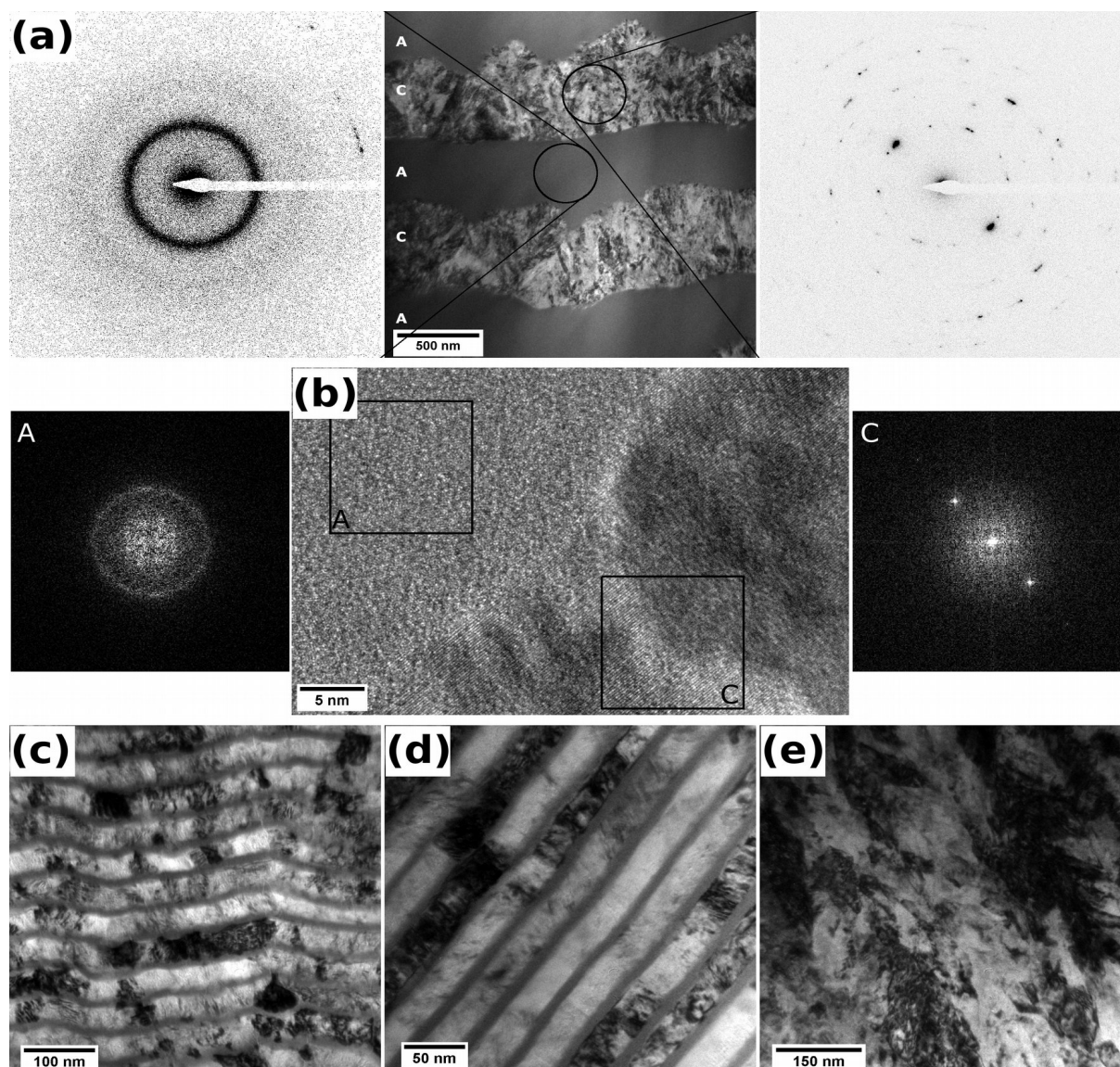
Figure E3: **TEM images of cross-sections: (a) Bright field micrograph and two selected area diffraction patterns of the indicated areas from a sample with 250 nm average sublayer thickness. The amorphous and crystalline sublayers are indicated as A and C, respectively. (b) High-resolution image of an interface in a sample with 290 nm sublayer thickness. The FFT patterns prove the amorphous (left) and crystalline (right) nature of the indicated areas. (c)-(e): Bright field micrographs of samples with (c) 30 nm, (d) 15 nm, and (e) 8 nm average sublayer thickness.**

E.3.3. Microhardness and nanoindentation

Figure E4a–b show the microhardness as a function of the sublayer thickness. The microhardness increases with decreasing sublayer thickness down to an average sublayer thickness of 15 nm, whereas below this value a hardness plateau is obtained. The hardness increase is approximately linear with the inverse square root of the sublayer thickness (Hall-Petch plot, Figure E4a), but also with the inverse sublayer thickness (Figure E4b). The former fit has the higher Pearson correlation coefficient, whereas the latter results in the better coefficient of determination (Table E2). Thus, both models describe the measured data with a similar quality.
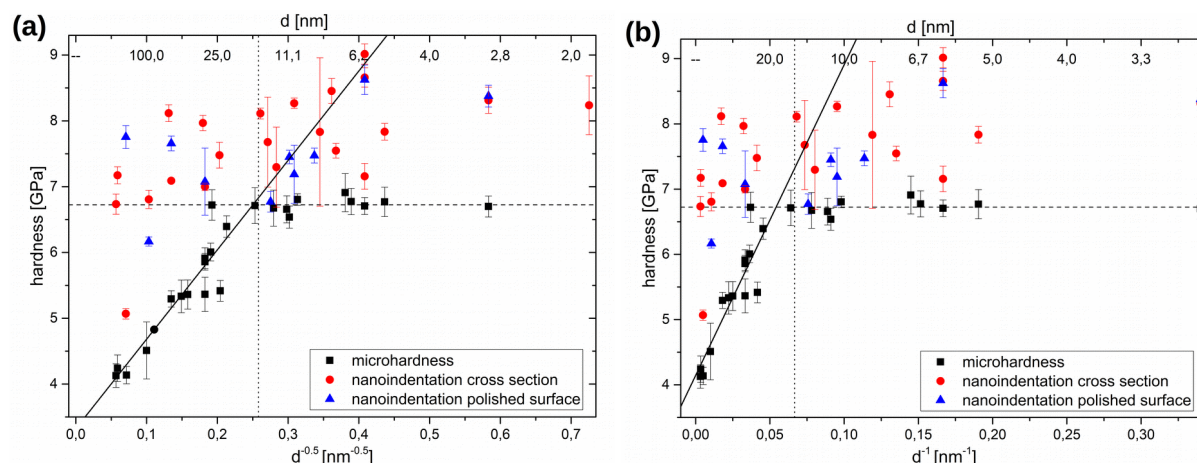
Figure E4: Microhardness and nanoindentation results plotted (a) in a Hall-Petch plot with respect to the average sublayer thickness and (b) as a function of the inverse average sublayer thickness. The dotted lines show the limit of a sublayer thickness of 15 nm, whereas the dashed lines show the hardness plateau beyond this point.

The lowest measured hardness value of 4.13 GPa corresponds to an indention depth of 3.0 μm. This is more than the generally recommended 10 % of the total layer thickness. However, measurements with reduced load resulted in more scatter due to the smaller indent size, but no significant change in hardness. Thus, no effect of the total layer thickness, i.e. the substrate, on the measured hardness values is expected.

The nanoindentation results scatter significantly more as compared to the microhardness (Figure E4a–b). However, a similar trend of a hardness increase up to a plateau with decreasing sublayer thickness is observed. Fitting the data in the range of increasing microhardness also results in a positive slope, i.e. an increase in hardness with decreasing sublayer thickness. However, the error of the slope is too large to extract any further information from it. The plateau, which is visible in the microhardness data, is almost indistinguishable and only indicated by the data points from the very thinnest layers in the nanoindentation results. Interestingly, no significant deviations between the two investigated loading directions (normal and parallel to the surface normal) occur.

Table E2: Results of the linear fits from Figure E4a+b and the corresponding Pearson correlation coefficients and coefficients of determination (R^2).

Fitting model	Hardness vs. $d^{-0.5}$	Hardness vs. d^{-1}
Slope	13.6 ± 1.4 GPa nm$^{0.5}$	47.6 ± 5.8 GPa nm
Intercept	3.3 ± 0.2 GPa	4.1 ± 0.2 GPa
Pearson R	0.937	0.915
R^2	0.878	0.837

All indention curves are smooth without any pop-ins that would be expected if the indentation had initiated delamination along sublayer interfaces (Figure E5a).

Since the Hall-Petch behavior is often observed in crystalline, but not in amorphous materials, additional hardness measurements were carried out on samples with a fixed nominal crystalline sublayer thickness of 100 nm and a nominal amorphous sublayer thickness varying from 25 to 300 nm. The results show no dependence of the microhardness on the thickness of the amorphous sublayer, but depend more on the scatter of the actual crystalline sublayer thickness (Figure E5b).
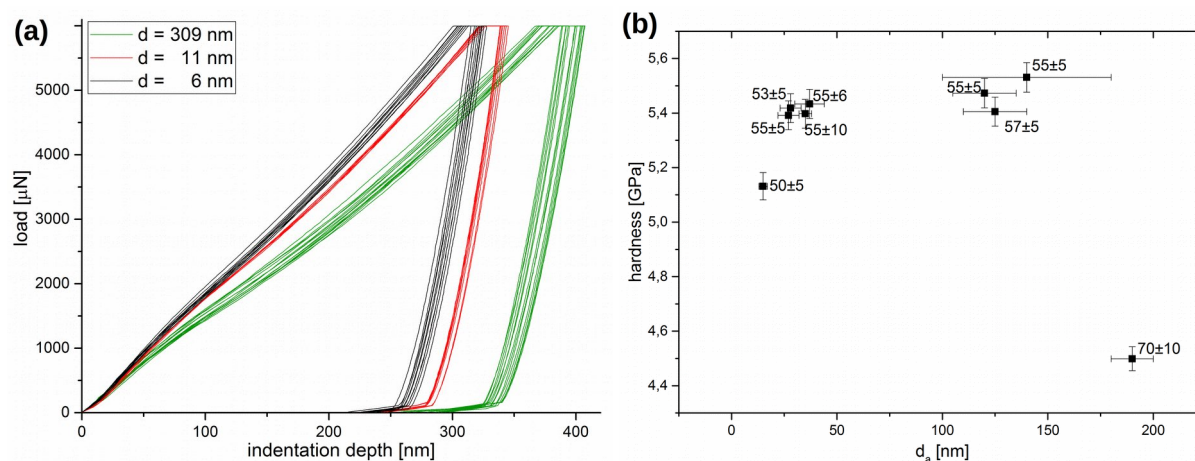

Figure E5: (a) Exemplary nanoindentation curves of samples with 6, 11, and 309 nm sublayer width, *d*, which show no sudden displacement bursts (pop-ins). (b) Microhardness measurements of samples with a constant nominal crystalline sublayer thickness of 100 nm and varying amorphous sublayer thickness, d_a. The numbers indicate the crystalline sublayer thicknesses. All sublayer thicknesses were measured on etched cross-sections in the SEM.

E.3.4. Microbending tests

Figure E6a shows the normalized load-displacement curves from the microbending experiments, which were performed on samples with 5 nm, 40 nm, and 310 nm average sublayer thickness. Despite the larger scatter of the data, the highest normalized load, i.e. the highest stresses, are obtained for the 40 nm sample, followed by the 5 nm and finally the 310 nm sample. Despite the highest stresses, also a deviation from a linear load-displacement relationship exists for some of the bending beams from the 40 nm sample. The in-situ SEM observation during the bending experiments of this sample revealed, that a crack is first initiated at the top surface of the bending beam and subsequently grows through the beam upon further loading (Figure E6b, video S1c). In contrast, the bending beams of the 5 nm and 310 nm samples all break through instantaneously after the crack was observed (videos S1a-b).
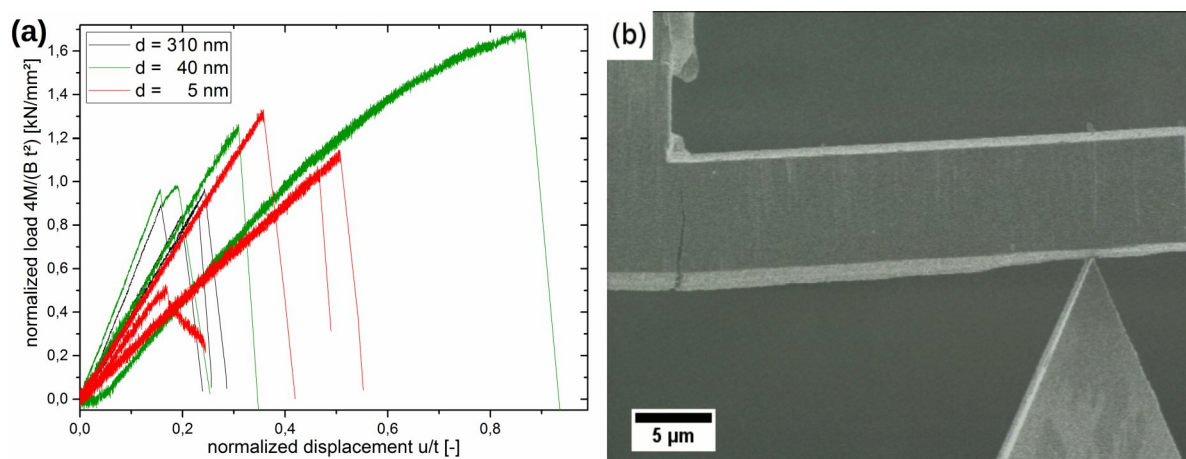
Figure E6: (a) Normalized force displacement diagram of the microbending tests. (b) In-situ SEM micrograph during the microbending experiment of the 40 nm sample with growing crack.

All bending beams failed parallel to the loading direction. The fracture surfaces were investigated with the SEM to gain information about the crack path. For the 310 nm sample, the fracture surface consists of alternating layers of small dimples and relatively flat regions (Figure E7a). The thickness of these alternating layers corresponds well with the sublayer thickness of the multilayer structure. EDX measurements revealed a higher phosphorus content in the flat regions of the fracture surface, indicating that these regions correspond to the amorphous sublayers. However, absolute phosphorus contents could not be obtained due to the large interaction volume for EDX measurements in the SEM. In the fracture surface of the 40 nm sample, a layered structure was also observed, but only in a part of the fracture surface (Figure E7c+d). Again, the layer thickness equals approximately the sublayer thickness of the multilayer structure. However, no amorphous and crystalline layers could be identified due to the smaller layer thickness. The fracture surface indicates that the crack was deflected at many layer interfaces, but finally kept its main growth direction parallel to the loading axis leaving no indications of the multilayer structure on the final part of the fracture surface. On the contrary, no layered structure was observed on the fracture surface of the 5 nm sample, which coincides with the loss of the multilayer structure for this sublayer thickness according to the TEM investigations (Figure E7b).
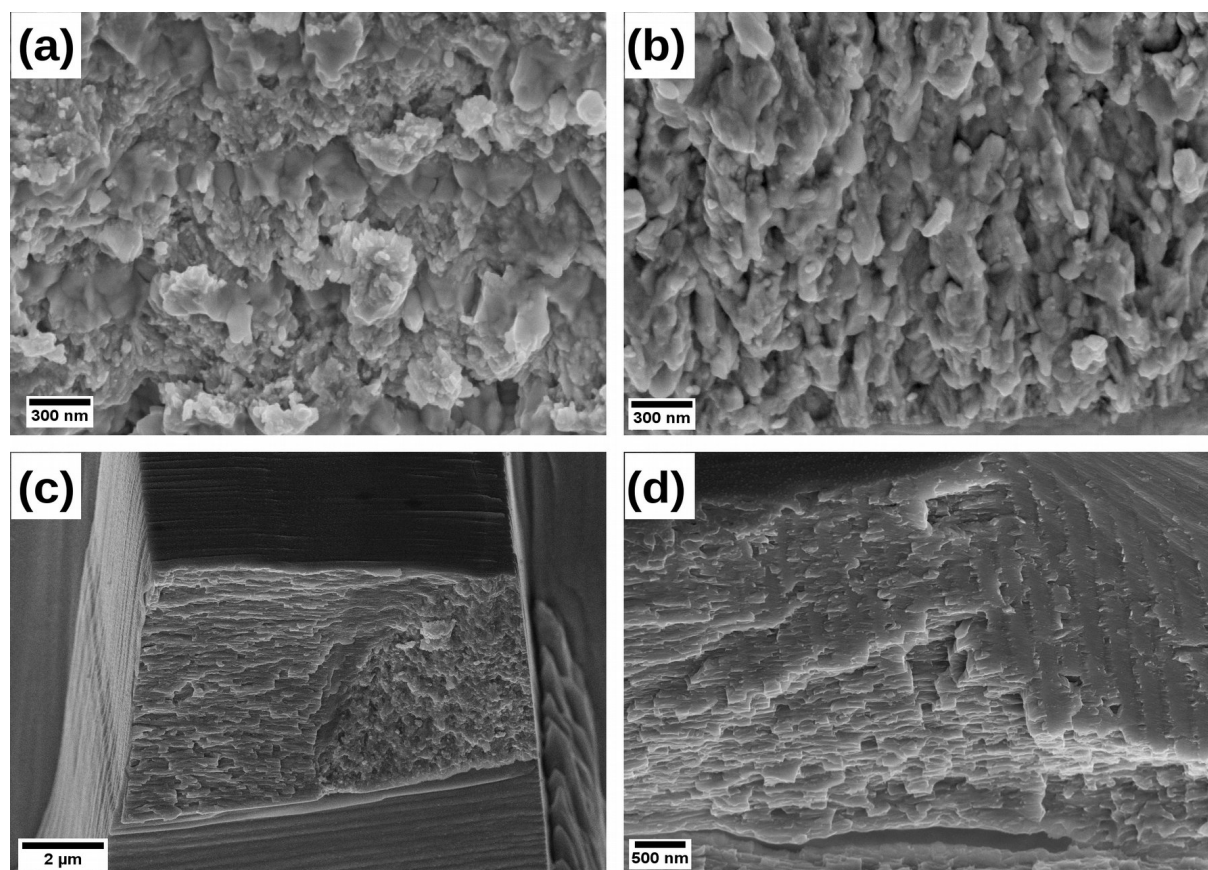
Figure E7: SEM images of the fracture surfaces of the microbending beams with (a) 310 nm, (b) 5 nm, and (c+d) 40 nm sublayer thickness. The images were taken with the primary electron beam approximately 30° (a+b) or 45° (c+d) to the fracture surface.

E.4. Discussion

E.4.1. Hall-Petch behavior for larger layer thicknesses

For the microhardness data of this study, both the Hall-Petch relation and a linear behavior with the inverse sublayer thickness describe the data with similar accuracy. Also in literature, both linear dependence on the inverse square root sublayer thickness (Hall-Petch) or on the inverse sublayer thickness are reported [E7-E12]. In the following, the results of the Hall-Petch fit are analyzed quantitatively and discussed in detail.

The hardness of the multilayer structure is assumed to combine the hardness of the two phases via a linear rule of mixture. The hardness of the amorphous phase is independent of the layer thickness, as it is observed in amorphous/amorphous multilayers [E14]. It may change if its composition changes with varying sublayer thickness. Although the results from the EDX measurements in the TEM indicate such a change, it will not be taken into account in the following analysis. On the one hand, even some signal from the substrate was observed in the EDX measurements indicating that the signal originates not completely from the intended area of

interest. This explains the slightly lower phosphorus contents as compared to literature values for amorphous Fe-P alloys as well as the decreasing phosphorus content with decreasing sublayer thickness since more low-phosphorus crystalline material is in close vicinity of the measurement area. On the other hand, slight variations in compositions are not expected to have such a significant effect as in crystalline matter. For these reasons, the hardness of the amorphous structure is set to a constant value of 4.65 ± 0.18 GPa as measured for the amorphous samples produced with direct current (Table E1). On the other hand, the hardness of the crystalline phase is assumed to depend on the sublayer thickness according to the Hall-Petch relation. With these assumptions, an intercept of 1.99 ± 0.40 GPa and a slope of 859.2 ± 88.8 MPa $\mu m^{0.5}$ are obtained for the Hall-Petch equation of the crystalline phase. Using a conversion factor of three [E42], this equals σ_0 = 660 ± 130 MPa and k_{HP} = 286 ± 30 MPa $\mu m^{0.5}$ for the yield stress. The intercept is significantly lower than the hardness of the crystalline single phase as obtained from the direct current samples (Table E1). However, possible deviations of the structure in a sublayer of a multilayer structure and in a direct current sample, which are prepared with the same deposition parameters, have to be considered. First, during the deposition of a crystalline sublayer on a multilayer structure, that has already a certain total thickness, less phosphorus is expected to be incorporated as compared to the deposition with the same parameters on a direct current sample of the same thickness, since the concentration of hypophosphite in the electrolyte close to the substrate is lower due to the larger previous consumption. This change in phosphorus content directly affects the mechanical properties due to solid solution hardening. Secondly, the high current density and the enrichment in phosphorus in the direct current samples result in a grain size that is significantly too small to take these samples as materials with quasi-infinite grain size as necessary for the intercept of the Hall-Petch plot. In most interstitial-free steels, the yield stress is much lower than the results of this analysis, but they contain only a small amount of phosphorus [E43]. In solution treated Fe-P alloys a similar hardness to the hardness intercept in the present study was obtained with about 1–2 at.-% P [E44], which is close to the compositions measured with EDX in the TEM. These measurements also indicate that there is no significant change of composition with varying sublayer thickness since the difference from 3 at.-% to 4 at.-% going from 290 nm to 30 nm sublayer thickness is close to the measurement inaccuracy of EDX.

The obtained Hall-Petch constant of 286 ± 30 MPa $\mu m^{0.5}$ for the yield stress seems to be too large for Fe-P alloys since the Hall-Petch constant for interstitial-free steels is reported to be between 130 and 180 MPa $\mu m^{0.5}$ [E45] and is slightly lowered by the presence of phosphorus [E46]. The presence of interstitial carbon would increase the Hall-Petch constant significantly, even for very low concentrations [E46]. However, sodium dodecyl sulfate, which is the only component of the

electrolyte that contains carbon, is present just in very low concentrations and is not known to result in co-deposition of carbon. Thus, the presence of carbon in the deposits can be excluded. The uncertainty of the conversion factor between hardness and yield strength might also be another reason for the discrepancy, since the conversion factor of three is just an approximation [E42] and a large range of conversion factors is reported in literature [E47, E48]. However, the main reason for the too large Hall-Petch constant might be the assumption of equal thickness of amorphous and crystalline sublayers for the determination of the sublayer thicknesses. The TEM results indicate that the assumption is approximately correct for large sublayer thicknesses, but the amorphous sublayers are much thinner than the crystalline ones for smaller thicknesses (see Figure E3). Thus, the phase fraction of the crystalline phase increases with decreasing sublayer width, resulting in an additional increase of strength beside the Hall-Petch effect as soon as the crystalline phase is harder than the amorphous phase. This effect was not included in the analysis above, which results in a too large Hall-Petch constant. However, a quantitative analysis of this effect would require the accurate measurement of the crystalline sublayer thicknesses for all samples which is impossible due to local fluctuations, calling for an unmanageable number of TEM samples, and the effect of etching parameters on the thickness of the individual layers for SEM investigations. Furthermore, for the largest sublayer thicknesses, grains smaller than the sublayer thickness are visible in the TEM micrographs (Figure E3a); in this case the hardness could be additionally influenced by the grain size. However, there are at least some grains going through the complete crystalline sublayer for all sublayer thicknesses. Thus, the maximum grain size in growth direction of the films always equals the sublayer thickness. For this reason, we do not expect a significant influence of grain size in our samples. However, a detailed grain size analysis was not performed and is out of the scope of this study. To separate the effects of grain size and sublayer thickness, one had to produce samples with constant sublayer thickness but different grain sizes. This may be achieved by modifying the deposition parameters. However, this might induce a simultaneous change in composition resulting again in two different hardening mechanisms which are difficult to separate.

E.4.2. Breakdown of the Hall-Petch relation and loss of multilayer structure for thinner layers

Transitions from Hall-Petch behavior to a hardness (or yield strength) plateau at a grain size or sublayer thickness in the nanometer regime are frequently reported. They are usually attributed to a change in deformation mechanism due to a threshold size below which no dislocation pile-up at the grain boundaries or multilayer interfaces can form [E9, E10]. This cannot be excluded for the transition observed in this study. However, from the TEM images in Figure E3 another reason for

the restricted range of validity of the Hall-Petch relation in the present case can be suggested: the loss of the amorphous/crystalline multilayer structure. The absence of continuous amorphous sublayers for average sublayer thicknesses smaller than 15 nm allows crystallites to grow to a size much larger than the intended sublayer thickness. The presence of multilayer structures in some regions of the samples in the SEM investigations indicate that there is still a periodic modulation (probably of phosphorus content) which results in a periodic change of the attack by the etching solution. Two main reasons may result in the loss of the amorphous sublayers for short periodicity lengths: the interface roughness and the decreasing amorphous-to-crystalline phase ratio with decreasing sublayer thickness. The roughness causes an inhomogeneous current density distribution during the deposition process. Once this inhomogeneity becomes too large, the current density during the deposition of the amorphous sublayers becomes sufficiently large to deposit not an amorphous, but a crystalline alloy at the regions, where the current density distribution has its maxima. The opposite effect during the deposition of crystalline sublayers at the minima of the current density distribution is less likely, since the minima coincide with the lowest points in the surface profile of the deposit, which are surrounded by an electrolyte depleted in hypophosphite due to geometrically impeded mass transport or diffusion, respectively. The decreased ratio of amorphous-to-crystalline sublayer thickness enhances the proposed mechanism for the breaking of the multilayer structure, since the thinner amorphous layers facilitate the penetration by crystalline phase.

E.4.3. Microbending tests and nanoindentation

The results in both microbending and nanoindentation scatter more than the microhardness measurements. This can be attributed to the smaller volume which is tested in these small-scale techniques. When local defects such as small pores or inclusions (e.g. hydroxides or phosphides) on nanometer scale are present in the tested volume of such tests, they result in measurable reduction in strength or hardness, respectively. On the other hand, a larger volume is probed in microhardness testing and the obtained values are averaged over a larger volume. Additionally, roughness and local deviations in sublayer thickness also attribute to the larger scatter in the testing methods with a smaller testing volume.

Despite the scattering, the microbending tests indicate some ductility for the intermediate nominal sublayer thicknesses, for which the sublayer thickness is already in the nanometer regime, but the amorphous/crystalline multilayer structure is still present. This can be attributed to the multiple crack deflection at the large number of interfaces, as visible on the fracture surfaces.

However, the maximum stresses obtained in microbending are lower than expected from the hardness measurements. Besides local defects, as discussed above, the residual stresses in the

deposits are another reason for this discrepancy. Tensile residual stresses for the crystalline phase, that were obtained from X-ray stress analysis, are a typical feature of iron electrodeposits [E49] and have also been found in purely amorphous Fe-P deposits [E29]. They promote crack initiation and crack growth in the tension part of the bending beam. On the other hand, their influence in the complex stress field during indentation is more complicated, but is expected to be less significant since the stresses are mainly compressive and the strains are quite large in the vicinity of the indent. The tensile residual stresses can also cause the observed delamination in multilayers with small sublayer widths after etching (Figure E2d), since the etched region acts as a notch, which results in crack growth or delamination under the tensile residual stresses if the stress concentration is high, i.e. if the notch is sharp enough. Thus, further improvement of the mechanical properties may be obtained by a reduction of residual stresses, which can be reached by changes in the deposition process (e.g. addition of suitable additives or pulse plating).

E.5. Summary

It was shown that amorphous/crystalline multilayer structures of Fe-P alloys can be prepared using the single bath electrodeposition technique. However, the multilayer structure breaks down below a sublayer thickness of 15 nm which is attributed to the role of roughness and amorphous-to-crystalline layer thickness ratio during the deposition process. A significant increase in strength according to the Hall-Petch relation was observed in the multilayer region, whereas a hardness plateau was observed when the multilayer structure was broken. Microbending tests showed that high strength and crack deflection at the interfaces can be obtained. Further improvement of the mechanical properties may be achievable in future by appropriate changes in the deposition process in order to decrease the minimum sublayer thickness for intact amorphous/crystalline multilayer structures as well as the number of local defects and the amount of residual stresses.

References

E1 I.K. Schuller, S. Kim, C. Leighton, Magnetic superlattices and multilayers, J. Magn. Magn. Mater. 200 (1999), 571-582. http://dx.doi.org/10.1016/S0304-8853(99)00336-4

E2 L. Peter, I. Bakonyi, Electrodeposition and properties of nanoscale magnetic/non-magnetic metallic multilayer films, in: G.T. Staikov (Ed.), Electrocrystallization in Nanotechnology, Wiley-VCHWeinheim, 2007, pp. 242-260. http://dx.doi.org/10.1002/9783527610198.ch12

E3 I. Bakonyi, L. Peter, Electrodeposited multilayer films with giant magnetoresistance (GMR): progress and problems, Prog. Mater. Sci. 55 (2010), 107-245. http://dx.doi.org/10.1016/j.pmatsci.2009.07.001

E4 B.M. Clemens, H. Kung, S.A. Barnett, Structure and strength of multilayers, MRS Bull. 24 (1999), 20-26. http://dx.doi.org/10.1557/S0883769400051502

E5 E.D. Hall, The deformation and ageing of mild steel, Proc. Phys. Soc. Lond. Sect. B 64 (1951), 747-753. http://dx.doi.org/10.1088/0370-1301/64/9/303

E6 N.J. Petch, The cleavage strength of polycrystals, J. Iron Steel Inst. 174 (1953), 25-28.

E7 C.A. Ross, Electrodeposited multilayer thin films, Annu. Rev. Mater. Sci. 24 (1994), 159-188. http://dx.doi.org/10.1146/annurev.ms.24.080194.001111

E8 A. Misra, M. Verdier, Y.C. Lu, H. Kung, T.E. Mitchell, M. Nastasi, J.D. Embury, Structure and mechanical properties of Cu-X (X=Nb,Cr,Ni) nanolayered composites, Scr. Mater. 39 (1998), 555-560. http://dx.doi.org/10.1016/S1359-6462(98)00196-1

E9 R.G. Hoagland, R.J. Kurtz, C.H. Henager, Slip resistance of interfaces and the strength of metallic multilayer composites, Scr. Mater. 50 (2004), 775-779. http://dx.doi.org/10.1016/j.scriptamat.2003.11.059

E10 A. Misra, J.P. Hirth, R.G. Hoagland, Length-scale-dependent deformation mechanisms in incoherent metallic multilayered composites, Acta Mater. 53 (2005), 4817-4824. http://dx.doi.org/10.1016/j.actamat.2005.06.025

E11 S.L. Lehoczky, Strength enhancement in thin-layered Al-Cu laminates, J. Appl. Phys. 49 (1978), 5479-5485. http://dx.doi.org/10.1063/1.324518

E12 S.L. Lehoczky, Retardation of dislocation generation and motion in thin-layered metal laminates, Phys. Rev. Lett. 41 (1978), 1814-1818. http://dx.doi.org/10.1103/PhysRevLett.41.1814

E13 S. Menezes, D.P. Anderson, Wavelength-property correlation in electrodeposited ultrastructured Cu-Ni multilayers, J. Electrochem. Soc. 137 (1990), 440-444. http://dx.doi.org/10.1149/1.2086459

E14 J.B. Vella, A.B. Mann, H. Kung, C.L. Chien, T.P. Weihs, R.C. Cammarata, Mechanical properties of nanostructured amorphous metal multilayer thin films, J. Mater. Res. 19 (2004), 1840-1848. http://dx.doi.org/10.1557/JMR.2004.0248

E15 C. Schuh, T.C. Hufnagel, U. Ramamurty, Mechanical behavior of amorphous alloys, Acta Mater. 55 (2007), 2067-4109. http://dx.doi.org/10.1016/j.actamat.2007.01.052

E16 Y. Wang, J. Li, A.V. Hamza, T.W. Barbee, Ductile crystalline-amorphous nanolaminates, Proc. Natl. Acad. Sci. USA 104 (2007), 11155-11160. http://dx.doi.org/10.1073/pnas.0702344104

E17 Y.Q. Wang, J.Y. Zhang, X.Q. Liang, K. Wu, G. Liu, J. Sun, Size- and constituent-dependent deformation mechanisms and strain rate sensitivity in nanolaminated crystallline Cu/amorphous Cu-Zr films, Acta Mater. 95 (2015), 132-144. http://dx.doi.org/10.1016/j.actamat.2015.05.007

E18 W. Guo, E. Jägle, J. Yao, V. Maier, S. Korte-Kerzel, J.M. Schneider, D. Raabe, Intrinsic and extrinsic size effects in the deformation of amorphous CuZr/nanocrystalline Cu nanolaminates, Acta Mater. 80 (2014), 94-106. http://dx.doi.org/10.1016/j.actamat.2014.07.027

E19 A. Donohue, F. Spaepen, R.G. Hoagland, A. Misra, Suppression of the shear band instability during plastic flow of nanometer-scale confined metallic glasses, Appl. Phys. Lett. 91 (2007), 241905. http://dx.doi.org/10.1063/1.2821227

E20 C.A. Ross, L.M. Goldman, F. Spaepen, An electrodeposition technique for producing multilayers of nickel-phosphorus and other alloys, J. Electrochem. Soc. 140 (1993), 91-98. http://dx.doi.org/10.1149/1.2056116

E21 L.M. Goldman, C.A. Ross, W. Ohashi, D. Wu, F. Spaepen, New dual-bath technique for electrodeposition of short repeat length multilayers, Appl. Phys. Lett. 55 (1989), 2182-2184. http://dx.doi.org/10.1063/1.102351

E22 C.A. Ross, D.T. Wu, L.M. Goldman, F. Spaepen, Measurements of interdiffusion in electrodeposited nickel-phosphorus multilayers, J. Appl. Phys. 72 (1992), 2773-2780. http://dx.doi.org/10.1063/1.351528

E23 M. Onoda, K. Shimizu, T. Tsuchiya, T. Watanabe, Preparation of amorphous/crystalloid soft magnetic multilayer Ni-Co-B alloy films by electrodeposition, J. Magn. Magn. Mater. 126 (1993), 595-598. http://dx.doi.org/10.1016/0304-8853(93)90697-Z

E24 G. Rivero, M. Multigner, E. Fraga, J. Alonso, J.L. Munoz, Control of magnetic anisotropy in electrodeposited CoP/Cu multilayers, IEEE Trans. Magn. 31 (1995), 4097-4099. http://dx.doi.org/10.1109/20.489873

E25 A. Brenner, Electrodeposition of Alloys, Vol. II, Academic Press, New York, 1963, p. 457. http://dx.doi.org/10.1016/B978-1-4831-9807-1.50026-X

E26 E.J. Hiltunen, J.A. Lehto, On the structure of Fe-P amorphous alloys prepared by electrodeposition and melt spinning methods, Phys. Scr. 34 (1986), 239-244. http://dx.doi.org/10.1088/0031-8949/34/3/011

E27 S. Vitkova, M. Kjuchukova, G. Raichevski, Electrochemical preparation of amorphous Fe-P alloys, J. Appl. Electrochem. 18 (1988), 673-678. http://dx.doi.org/10.1007/BF01016891

E28 G. Dietz, K. Richter, F. Stein, H.C. Schäfer, The microstructure of electrodeposited amorphous or microcrystalline Fe-P alloys, Z. Phys. B Condens. Matter 81 (1990), 223-228. http://dx.doi.org/10.1007/BF01309352

E29 S. Armyanov, S. Vitkova, O. Blajiev, Internal stress and magnetic properties of electrodeposited amorphous Fe-P alloys, J. Appl. Electrochem. 27 (1997), 185-191. http://dx.doi.org/10.1023/A:1018404024196

E30 F. Wang, K. Itoh, T. Watanabe, Relationship between the crystallographic structure of electrodeposited Fe-P alloy film and its thermal equilibrium phase diagram, Mater. Trans. 44 (2003), 127-132. http://dx.doi.org/10.2320/matertrans.44.127

E31 C. Ruscior, E. Croiala, Chemical iron-phosphorus films, J. Electrochem. Soc. 118 (1971), 696-698. http://dx.doi.org/10.1149/1.2408146

E32 G.-F. Huang, W.-Q. Huang, L.-L. Wang, B.-S. Zou, Q.-L. Wang, J.-H. Zhang, Studies on the Fe-P film plating from a chemical bath: deposition mechanism and parameter effects, Int. J. Electrochem. Sci. 3 (2008), 145-153.

E33 V.V. Bondar, Yu. M. Polukarov, Composition and magnetic properties of electrodeposited iron-phosphorus alloys, Elektrokhimiya 4 (1968), 1368-1369.

E34 K. Kamei, Y. Machara, Structure and magnetic properties of pulse-plated Fe-P and Fe-Cu-P amorphous alloys, Mater. Sci. Eng. A 181/182 (1994), 906-910. http://dx.doi.org/10.1016/0921-5093(94)90767-6

E35 A. Mikó, E. Kuzmann, M. Lakatos-Varsányi, A. Kákay, F. Nagy, L.K. Varga, Mössbauer and XRD study of pulse plated Fe-P and Fe-Ni thin layers, Hyperfine Interact. 165 (2005), 195-201. http://dx.doi.org/10.1007/s10751-006-9265-x

E36 L. Elias, K.U. Bhat, A.C. Hedge, Development of nanolaminated multilayer Ni-P alloy coatings for better corrosion protection, RSC Adv. 6 (2016), 34005-34013. http://dx.doi.org/10.1039/C6RA01547F

E37 J. Crousier, Z. Hanane, J.-P. Crousier, Electrodeposition of NiP amorphous alloys. A multilayer structure, Thin Solid Films 248 (1994), 51-56. http://dx.doi.org/10.1016/0040-6090(94)90210-0

E38 C.C. Nee, R. Weil, The banded structure of Ni-P electrodeposits, Surf. Technol. 25 (1985), 7-15. http://dx.doi.org/10.1016/0376-4583(85)90043-3

E39 S. Wurster, C. Motz, M. Jenko, R. Pippan, Micrometer-sized specimen preparation based on ion slicing technique, Adv. Eng. Mater. 12 (2010), 61-64. http://dx.doi.org/10.1002/adem.200900263

E40 W.D. Nix, H. Gao, Indentation size effects in crystalline materials: a law for strain gradient plasticity, J. Mech. Phys. Solids 46 (1998), 411-425. http://dx.doi.org/10.1016/S0022-5096(97)00086-0

E41 C. Genzel, Problems related to X-ray stress analysis in thin films in the presence of gradients and texture, in: E.J. Mittemeijer, P. Scardi (Eds.), Diffraction Analysis of the Microstructure of Materials, Springer, Berlin, 2004, pp. 473-503. http://dx.doi.org/10.1007/978-3-662-06723-9

E42 D. Tabor, The hardness and strength of metals, J. Inst. Met. 79 (1951), 1-18.

E43 W. Guo, Z. Wang, Y. Li, N. Xu, J. Shin, Effect of phosphorus content on properties of warm-rolled interstitial-free steel sheets, Metallogr. Microstruct. Anal. 2 (2013), 249-256. http://dx.doi.org/10.1007/s13632-013-0086-4

E44 E. Hornbogen, Precipitation of phosphorus from alpha iron and its effect on plastic deformation, Trans. Am. Soc. Met. 53 (1961), 569-589.

E45 S. Takaki, Review on the Hall-Petch relation in ferritic steels, Mater. Sci. Forum 654–656 (2010), 11-16. http://dx.doi.org/10.4028/www.scientific.net/MSF.654-656.11

E46 N. Nakada, M. Fujihara, T. Tsuchiyama, S. Takaki, Effect of phosphorus on Hall-Petch coefficient in ferritic steel, ISIJ Int. 51 (2011), 1169-1173. http://dx.doi.org/10.2355/isijinternational.51.1169

E47 E.J. Pavlina, C.J. van Tyne, Correlation of yield stress and tensile strength with hardness for steels, J. Mater. Eng. Perform. 17 (2008), 888-893. http://dx.doi.org/10.1007/s11665-008-9225-5

E48 P. Zhang, S.X. Li, Z.F. Zhang, General relationship between strength and hardness, Mater. Sci. Eng. A 529 (2011), 62-73. http://dx.doi.org/10.1016/j.msea.2011.08.061

E49 Y.D. Gamburg, G. Zangari, Theory and Practice of Metal Electrodeposition, Springer, New York (2011), p. 355. http://dx.doi.org/10.1007/978-1-4419-9669-5